Preparation of Porous Materials with Aligned Pores by Unidirectional Freezing and Freeze-Drying

Jin-Woong Kim

Contents

Appendix I

Appendix II

Chapter I

General Introduction

1.1 Introductory Remarks

Porous materials are defined as solids containing pores inside of materials. Porous materials have specific properties such as high surface area, high permeability, lightweight, and low thermal conductivity. Due to these characteristics, a wide range of applications such as catalyst supports,[1] membranes[2], filters,[3] bioscaffolds,[4-7] porous electrodes,[8] lightweight materials,[9] and insulators[10] have been researched and developed. As described below, pore can be classified by pore size and interconnectivity.

Size: The International Union of Pure and Applied Chemistry (IUPAC) categorizes pores by their pore diameter: micropore (pore diameter < 2 nm), mesopore (2 nm < pore diameter < 50 nm), and macropore (50 nm < pore diameter)

Connectivity: open pores are connected to the outside of the material, and closed pores are isolated from the outside

For the application of porous materials, it is necessary to manipulate several important factors such as composition, pore size, connectivity, pore size distribution, specific surface area, permeability, and mechanical strength.[11] For examples, pore size must be controlled for the proper usage as membrane, filter, and bioscaffold. For the applications which require high permeability such as adsorbent and catalyst, porous structures which has open pores and high specific surface area have to be prepared. On the opposite of these applications, closed pore is preferred for thermal insulator. The preparation methods of porous polymeric materials and ceramic materials are discussed

in the next sections.

1.2. Methods for Preparation of Porous Polymeric Materials

Several techniques have been developed to fabricate polymeric porous structures: porogen leaching,[12] microbead patterning,[13] phase separation,[14,15] drying of polymer blend solution,[16] gas foaming,[17] 3D printing,[18] and freeze/freeze-drying.[6,19-21] In this section, the representative methods to prepare porous polymeric materials are introduced.

1.2.1. Foaming

Foaming is the most commonly used method to prepare polymeric porous materials. In the early stage of development, polymer foam was fabricated using vaporization of low boiling organic chemicals such as pentane and hydrochlorofluorocarbons (HCFCs)[22] that could be dissolved in polymer.[23] Then, foaming process using chemical foaming agent (CFA) was developed. The CFA is a thermally unstable component, which is added to the polymer. Upon heating the CFA decomposes into gaseous components, resulting in the desired foam[17]. Polyurethane (PUR) foam is the representative polymeric foam that was fabricated using a gaseous CFA formed by the reaction of two polymeric components.[24] Due to the environmental problem that was caused by HCFCs, environment friendly foaming process which was using gases, mainly carbon dioxide, as physical foaming agent (PFA) was developed. The foaming process using CO_2 as PFA is based on the solubility of CO_2 in polymers and the decrease of glass transition temperature (T_g) of polymer with the increase of

impregnated CO_2 by pressurization. After dissolving CO_2, foaming can be performed by the increase of temperature or the decrease of pressure. Polymeric foams can be classified in terms of pore size: macrocellular foams (typical cell sizes of 50 μm or larger) and microcellular foams (MCFs, a typical cell size of 10-100 μm and cell densities ranging from 10^8 to 10^{15} cells/cm^3). MCFs was firstly developed by Suh et al. [25,26] in the 1980s, to save materials while maintaining mechanical strength. Recently, Foaming of polymer blend was researched to control pore morphology of polymeric foam.[17,27] Nanoassembled block copolymer was also foamed to prepare well aligned porous film using the difference of CO_2 solubility and glass transition temperature of polymers.[28]

1.2.2 Phase Separation

Phase separation of a polymer solution is one of the useful methods to create and control polymer morphology. There are several methods to induce phase separation such as thermally induced phase separation (TIPS),[14,29-32] solvent induced phase separation (SIPS),[16,33,34] and nonsolvent induced phase separation (NIPS).[35-38] These phase separation methods utilize solubility difference as a driving force for morphology development. General phase diagrams of polymer-solvent binary system and polymer-polymer-solvent ternary system are shown in Figure 1.1.

TIPS process utilizes the difference in solubility of polymer in solution by temperature. If polymer is added to a solvent that shows upper critical solution temperature (UCST), homogeneous polymer solution can be prepared at high temperature. Then, phase separation can be induced by decreasing solution temperature. After phase separation, phase separated solvent is removed by drying or rinse with other

solvent to create pore in polymer. As an alternative method to induce phase separation, solvent induced phase separation (SIPS) has been proposed. SIPS process utilizes the solubility change of polymer solution by the addition of poor solvent. Generally, Polymer is dissolved in a good solvent for used polymer. After casting of the solution, it is immersed into a poor solvent. This process causes the change of solvent composition by diffusion and finally the precipitation of polymer rich phase. One of the main differences of SIPS with TIPS is that asymmetric porous structure can be prepared by SIPS due to the penetration of a poor solvent in one direction. This method has been used for preparation of asymmetric membrane since Loeb et al.[35] developed it in early 1960's. Moreover, nonsolvent induced phase separation (NIPS) has been also used to prepare porous structure that is composed of immiscible polymer blend. NIPS process utilizes solubility of good solvent for two immiscible polymers. If homogeneous solution of immiscible polymer blend is dried by the evaporation of solvent, phase separation of polymer that has relatively low solubility for the used solvent occurs. This remains phase separated porous morphology of polymer blend. One polymer, which has selective solubility in that polymer, also can be leached out using solvent. Kim et al.[16] prepared a unique highly ordered microporous film using this method with PS/PEG/Solvent systems.

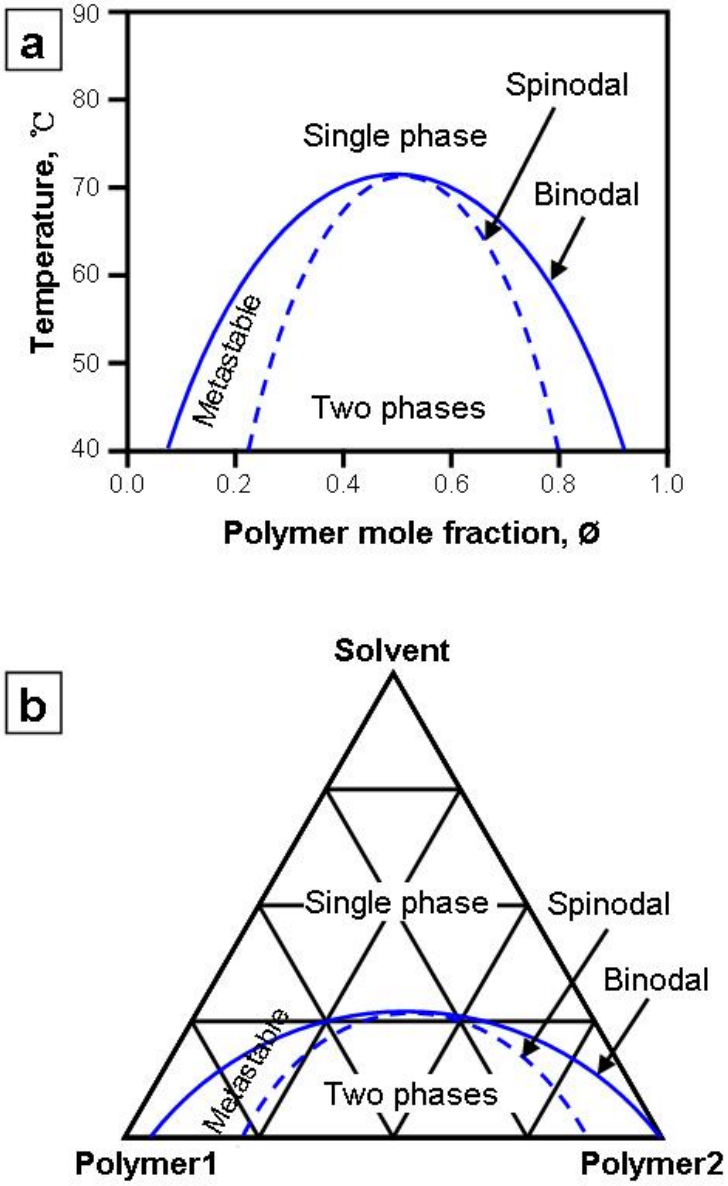

Figure 1.1. A schematic phase diagram of a polymer solution. (a) binary phase and (b) ternary phase.

1.2.3 Leaching

Porous polymeric materials can be also prepared by porogen leaching technology, which was originally developed to prepare porous membrane. In this method, polymer is dissolved in a highly volatile solvent and porogen is added to the solution. Porogens are size controlled insoluble materials (mainly water soluble inorganic salts such as sodium chloride, ammonium carbonate, and sugar) in organic solvent. Then, it can be solidified by solvent casting. After solidification of the polymer-porogen mixture, porous polymeric structure can be prepared by leaching porogen with water or rinse solvent. Recently, template leaching technology, known as solvent casting and particulate leaching (SCPL), was adopted to prepare polymeric bioscaffold by Mikos et al [5,39]. They prepared three-dimensional biodegradable foams by laminating porous poly(L-lactic acid) and copolymers of poly(DL-lactic-co-glycolic acid). One of the main advantages of this method is that the pore size and morphology can be controlled by the size, size distribution, and added amount of porogen.[40]

1.2.4 Other Techniques

Many other methods to prepare polymeric porous materials have been investigated over the past decades. Membranes for ultrafiltration and microfiltration were mainly prepared using stretching of semicrystalline polymers such as PP or PTFE.[41] Pores from 20 nm to 200 nm can be prepared by separation of lamella crystalline of polymer using this method. Nuclear track etching method was also developed to prepare microfiltration membrane. Moreover, vapor breathing technology was developed to prepare polymer films with regular arrays of submicron to micron-sized pores.[42] This method utilized

condensing of water vapor on the casted polymer solution and honeycomb like arrangement of condensed water on polymer solution.

1.3. Methods for Preparation of Porous Ceramic Materials

Techniques of preparing porous ceramic materials have been investigated intensively because of their high potential usage. Typical processing methods including replica technique, sacrificial template technique, and direct foaming are introduced in this section.

1.3.1. Replica Technique

Most of porous ceramic materials are currently fabricated using a replica technique, which produces the so-called reticulated ceramics. Reticulated ceramics are open cellular materials consisting of interconnected voids surrounded by a web of ceramic ligaments [43]. General replication procedure is as follows:

1) An open cellular structure (synthetic porous structure or natural porous structure) is soaked into ceramic suspension or preceramic polymer.
2) Excess ceramic suspension or preceramic polymer is removed by passing through roller.
3) The coated cellular structure is dried.
4) The cellular structure is removed by burning at appropriate temperature.
5) The remained cellular ceramic structure is calcined at high temperature.

Through described procedure, a cellular ceramic which has the same morphology as the original porous material can be fabricated. Only open cellular ceramic structure

can be produced using this technique due to the usage of open cellular template. The replica technique was firstly developed by Schwartzwalder and Somers[44] for the production of macroporous ceramics using polymeric sponges as replication material. Recently Byrne et al.[45] reported the use of wood as a cellular structure to produce porous silicon carbide structure. They prepared carbonized wood monolith by controlled thermal decomposition of wood. Then, the carbonized structure was converted to silicon carbide structure using liquid infiltration/reaction process or sol-gel infiltration/reaction process.

1.3.2. Sacrificial Template Technique

Basic concept of sacrificial template technique is the same as the leaching method for preparing of polymeric porous materials described previously in the section 1.2.3. The difference of this method from the replica technique is that a negative replica of original sacrificial template can be obtained. Many materials have been used for sacrificial template such as polymer beads,[46] polymeric gels,[47] solvent crystals,[48] and salts[49]. Using proper template, pore size can be controlled from several nanometers to millimeters. The biphasic composite of ceramic and template material can be prepared using several methods such as dip coating and drying,[50] freezing,[48] sol-gel synthesis,[51] and infiltration, [49,52] etc. Then, sacrificial template has to be removed using proper method such as pyrolysis, evaporation, sublimation, and chemical leaching. Due to the high thermal resistance of ceramics, removal of template using thermal treatment is possible.

1.3.3. Direct Foaming

Direct foaming method offers an easy, cheap, and fast way of preparing macroporous ceramics. In this method, porous structure is prepared by the dispersion of gas bubbles in the liquid slurry of ceramic powders or inside a ceramic precursor solution. Both close and open porous ceramics can be prepared using this method by controlling coalescence time of bubbles.[43] This method can be classified by gas generation method: 1) addition of external gas and 2) in situ generation of gas.[53] External gas was added using injection method or mechanical frothing.[54] For the in situ gas generation, several methods such as chemical blowing agent[55] (gas can be developed in situ by chemical reactions or thermal decomposition) and physical blowing agent[56,57] (a volatile liquid such as Freon and dichloromethane) were reported. The prepared foam morphology has to be stabilized by addition of surfactant, protein, or solid particles with tailored surface because the porous structure can be easily collapsed due to the inherent instability.[58] After preparation of bubbles, it must be solidified in order to maintain its porous morphology. Up to now several methods such as gelation[56] and thermosetting[57] have been developed to stabilize the prepared morphology.

1.3.4. Other Techniques

Porous ceramic structure can be also fabricated using other techniques such as extrusion, fused deposition or prototyping, random alignment of fiber, and direct sintering of ceramic powder. Various shapes of honeycomb structured ceramics have been prepared using paste extrusion of ceramic powders[59]. Several researchers reported preparation of well designed three-dimensional structure using fused deposition or

robotic rapid prototyping technique.[60] Mat of ceramic fiber can be also prepared using random alignment of ceramic fibers.[61] Direct sintering of ceramic powder[62] is one of the simple methods to prepare porous ceramic structures.

1.4. Preparation of Porous Materials using Unidirectional Freezing

Unidirectional freezing is an easy and cost effective technique for preparing porous materials. Regularly aligned crystals of water or organic solvent can be prepared by unidirectional freezing. Then, crystals can be removed by thawing[63] or direct sublimation[64] at low temperature and *in vacuo* to prepare aligned pores. A porous structure which has aligned pore channels[63-65] or fibers[66] can be prepared using this technique. The pore morphology prepared by unidirectional freezing absolutely depends on the crystal morphology. Up to now, formations of lamellar, rods, cells, and dendrites type crystal were reported. However, terms of prepared porous structures were not yet clearly defined. For example, porous structure prepared by templating dendrite crystal was described as fish bone structure or ladder-like structure. In this dissertation, lamellar, fiber, cellular honeycomb, and dendritic honeycomb were added to describe the pore morphology and to understand easily the origin of pore morphology.

For the unidirectional freezing and freeze-drying, the solvent has to satisfy two conditions: it must be frozen at moderate low temperature and the sublimation of solvent crystal under reasonable temperature and pressure has to be achievable. Up to now, water, camphene,[67] 1,4-dioxane,[6,64] tert-butyl alcohol,[68] benzene[6] and dichloroethane.[20] and liquid CO_2 were used for unidirectional freezing and

freeze-drying.[69] Freezing temperature and boiling temperature of these solvent is summarized in Table 1.1.

Since Mahler and Bechtold[70] reported the preparation of silica fiber and lamellar using unidirectional freezing of silica gel. This method has attracted much attention as a preparation method for porous polymers and ceramics because of its inherently high contact efficiency and the controllability of its morphology. The structure prepared by unidirectional freezing has great potential as a catalyst support,[1] catalyst,[71] substrate for drug delivery,11 [72] bioscaffold,[6,73] and porous electrodes,[8]

Unidirectional freezing can be classified into two; unsteady state freezing method and pseudo steady state freezing method. Fukasawa et al.[48] used a cylindrical container, the bottom of which was made of metal with high thermal conductivity and the side was made of fluororesin with low thermal conductivity. They immersed only the container bottom face into a refrigerant. Koh et al [74] placed polyethylene molds containing ceramic/camphene slurry directly in a cold water bath to control crystal growth in the radial direction. The steady state growth of crystal can not be realized by these methods due to dynamic change in temperature profile. Improvement of the method was made by Deville et al. [65]. They used polytetrafluoroethylene molds placed between two copper cold fingers and the temperature of copper is regulated to control the speed of the solidification front. Recently, Waschkies et al. calculated temperatures of double side cooling to maintain a constant solidification velocity. [75] However, the easiest method of achieving a pseudo steady state growth of crystal is soaking the container of solution into the cooling medium. The size of materials also can be easily controlled by changing the container. Using this way, Tamon and coworkers prepared several kinds of porous structures [63,71,76-82].

Table 1.1. Summary of freezing point and boiling point of solvents which were used for unidirectional freezing

Solvent	Freezing point (℃)	Boiling point (℃)
Water	0.0	100.0
1,4-Dioxane	11.8	101.1
Tert-butyl alcohol	25.7	82.4
Benzene	5.5	80.1
Diethyl ether	-35.0	83.5
Camphene	45.0-46.0	159.0

1.5. Objective of This Work

As described in the previous section, unique porous structure which has aligned pore channels or fibers can be prepared using unidirectional freezing of polymer solution or ceramic suspension. Up to now, several research groups have investigated unidirectional freezing technique to prepare aligned porous structure. However, the preparation of polymeric porous structure and the control of its morphology using the change of crystal type were not intensively researched. To elucidate morphology control mechanism and to find potential application, further research must be conducted in this area.

In this dissertation, the author propose a method of preparing polymeric honeycomb monolith structure using unidirectional freezing of polymer-solvent binary solution and polymer-polymer-solvent ternary solution. To control the morphology of honeycomb monolith structure, the effect of several factors such as polymer

concentration, freezing rate, polymer blend ratio, and polymer molecular weight were investigated. Poly(L-lactic acid) (PLLA) was used as structuring material because it is very useful for bioscaffold. Poly(ethylene glycol) (PEG) was used as sacrificial template. Then, the research was extended to the unidirectional freezing of colloidal suspension consisted of monodispersed poly[styrene-(co-2-hydroxyethyl methacrylate)] particles and silica particles. The contents of each chapter in this dissertation are as follows:

In chapter II, the preparation method of honeycomb monolith structured poly(L-lactic acid) (PLLA) was investigated by combining pseudo steady state unidirectional freezing and freeze-drying of PLIA/Dehydrated 1,4-dioxane solution. Aligned porous structures, which have either smooth wall microchannels or ladder-like microchannels aligned parallel to the freezing direction and have a honeycomb structure in its vertical direction, were prepared. The effects of polymer concentration, unidirectional freezing rate and water contents on the aligned porous structure were thoroughly investigated. Based on the investigation, a simple and unique method to control smoothness of the microchannel wall and its interconnectivity was suggested.

In chapter III, based on the unidirectional freezing method which was set up in chapter II, a honeycomb monolith structure with a sea-and-island morphology, where PEG domains were dispersed in the PLLA matrix, was developed by inducing polymer-polymer phase separation during a pseudo steady-state unidirectional freezing of polymer-polymer-solvent system; PLLA, Poly(ethylene glycol) (PEG), and dehydrated 1,4-dioxane. Then, pores were created in the channel walls of the honeycomb monolith structure by leaching out the PEG domains. The effects of the PEG molecular weight and the PLLA/PEG weight ratio on the aligned honeycomb structure and the pores in the channel walls were investigated. Based on the cloud point

and freezing point measurements, hypotheses for the mechanism of the cellular to dendritic transition and the formation mechanism of the pores in the channel walls are proposed.

In chapter IV, a honeycomb monolith-structured silica with highly ordered, three-dimensionally interconnected macroporous walls was fabricated by unidirectional freezing and freeze-drying of colloidal suspension of poly[styrene-(co-2-hydroxyethyl methacrylate)] particles and silica particles. The effects of total particle concentrations and freezing rate on the average diameter of the micro-scale channels and the wall thicknesses were investigated. The self-organization mechanism of two kinds of nanoparticles between ice crystals was exploited.

In chapter V, the control of aligned porous structure was discussed by paying attention to the underlying principles of the crystal growth during unidirectional freezing. To discuss the morphology control, several papers were reviewed and classified by raw materials; polymer solution, colloidal suspension which is accompanying sol-gel reaction, ceramic slurry or colloidal suspension which is not accompanying with sol-gel reaction. Based on the investigation of papers and experimental result of this dissertation, strategy to control the morphology of each system was suggested.

In chapter VI, all results in this dissertation are summarized.

1.6. Reference

(1) Deleuze, H.; Schultze, X.; Sherrington, D. C. *Polymer* **1998**, *39*, 6109.

(2) Komolikov, Y. I.; Blaginina, L. A. *Refractories and Industrial Ceramics* **2002**, *43*, 181.

(3) Kersting, R. *Synthetic Polymer Membrane*; Wiley: Newyork, 1985.

(4) Goldstein, A. S.; Zhu, G. M.; Morris, G. E.; Meszlenyi, R. K.; Mikos, A. G. *Tissue Engineering* **1999**, *5*, 421.

(5) Mikos, A. G.; Sarakinos, G.; Leite, S. M.; Vacanti, J. P.; Langer, R. *Biomaterials* **1993**, *14*, 323.

(6) Ma, P. X.; Zhang, R. Y. *Journal of Biomedical Materials Research* **2001**, *56*, 469.

(7) Nishikawa, T.; Nonomura, M.; Arai, K.; Hayashi, J.; Sawadaishi, T.; Nishiura, Y.; Hara, M.; Shimomura, M. *Langmuir* **2003**, *19*, 6193.

(8) Moon, J. W.; Hwang, H. J.; Awano, M.; Maeda, K. *Materials Letters* **2003**, *57*, 1428.

(9) Meador, M. A. B.; Fabrizio, E. F.; Ilhan, F.; Dass, A.; Zhang, G. H.; Vassilaras, P.; Johnston, J. C.; Leventis, N. *Chemistry of Materials* **2005**, *17*, 1085.

(10) Lysenko, V.; Roussel, P.; Remaki, B.; Delhomme, G.; Dittmar, A.; Barbier, D.; Strikha, V.; Martelet, C. *Journal of Porous Materials* **2000**, *7*, 177.

(11) Ishizaki, K., Komarneni,S., Nanko, M. *Porous Materials: Process Technology and Applications*; illustrated ed.; Springer: Dordrecht, 1998.

(12) Kothapalli, C. R.; Shaw, M. T.; Wei, M. *Acta Biomaterialia* **2005**, *1*, 653.

(13) Lu, M. H.; Zhang, Y. *Advanced Materials* **2006**, *18*, 3094.

(14) Nam, Y. S.; Park, T. G. *Biomaterials* **1999**, *20*, 1783.

(15) Hua, F. J.; Park, T. G.; Lee, D. S. *Polymer* **2003**, *44*, 1911.

(16) Kim, J. K.; Taki, K.; Ohshima, M. *Langmuir* **2007**, *23*, 12397.

(17) Taki, K.; Nitta, K.; Kihara, S.; Ohshima, M. *Journal of Applied Polymer Science* **2005**, *97*, 1899.

(18) Lee, M.; Dunn, J. C. Y.; Wu, B. M. *Biomaterials* **2005**, *26*, 4281.

(19) Zhang, H.; Cooper, A. I. *Advanced Materials* **2007**, *19*, 1529.

(20) Zhang, H. F.; Hussain, I.; Brust, M.; Butler, M. F.; Rannard, S. P.; Cooper, A. I. *Nature Materials* **2005**, *4*, 787.

(21) Zhang, R. Y.; Ma, P. X. *Journal of Biomedical Materials Research* **1999**, *44*, 446.

(22) Gendron, R. *Thermoplastic Foam Processing: Principles and Developmet*; CRC Press: Newyork, 2005.

(23) Jacobs, L. J. M.; Kemmere, M. F.; Keurentjes, J. T. F. *Green Chemistry* **2008**, *10*, 731.

(24) Campbell, G. A. *Journal of Applied Polymer Science* **1972**, *16*, 1387.

(25) Colton, J. S.; Suh, N. P. *Polymer Engineering and Science* **1987**, *27*, 500.

(26) Martinivve, J. E.; Suh, N. P.; Waldman, F. A. U.S. Patent 4473665-A, 1984.

(27) Han, X. M.; Shen, J.; Huang, H. X.; Tomasko, D. L.; Lee, L. J. *Polymer Engineering and Science* **2007**, *47*, 103.

(28) Taki, K.; Waratani, Y.; Ohshirna, M. *Macromolecular Materials and Engineering* **2008**, *293*, 589.

(29) Lloyd, D. R.; Kinzer, K. E.; Tseng, H. S. *Journal of Membrane Science* **1990**, *52*, 239.

(30) Lloyd, D. R.; Kim, S. S.; Kinzer, K. E. *Journal of Membrane Science* **1991**, *64*, 1.

(31) Nam, Y. S.; Park, T. G. *Journal of Biomedical Materials Research* **1999**, *47*, 8.

(32) Nishi, T.; Wang, T. T.; Kwei, T. K. *Macromolecules* **1975**, *8*, 227.

(33) Kumacheva, E.; Li, L.; Winnik, M. A.; Shinozaki, D. M.; Cheng, P. C. *Langmuir*

1997, *13*, 2483.

(34) Hopkinson, I.; Myatt, M. *Macromolecules* **2002**, *35*, 5153.

(35) Loeb, S.; Sourirajan, S. *Advances in Chemistry Series* **1962**, *38*, 117.

(36) Wang, H. Y.; Kobayashi, T.; Fujii, N. *Langmuir* **1996**, *12*, 4850.

(37) Wang, H. Y.; Kobayashi, T.; Fukaya, T.; Fujii, N. *Langmuir* **1997**, *13*, 5396.

(38) Ying, L.; Kang, E. T.; Neoh, K. G. *Langmuir* **2002**, *18*, 6416.

(39) Mikos, A. G.; Thorsen, A. J.; Czerwonka, L. A.; Bao, Y.; Langer, R.; Winslow, D. N.; Vacanti, J. P. *Polymer* **1994**, *35*, 1068.

(40) Zeltinger, J.; Sherwood, J. K.; Graham, D. A.; Mueller, R.; Griffith, L. G. *Tissue Engineering* **2001**, *7*, 557.

(41) Fried, J. R. *Polymer science and technology*; 2nd ed.; Prentice Hall: Upper Saddle River, 2003.

(42) Maruyama, N.; Koito, T.; Nishida, J.; Sawadaishi, T.; Cieren, X.; Ijiro, K.; Karthaus, O.; Shimomura, M. *Thin solid Films* **1998**, *327*, 854.

(43) Colombo, P. *Philosophical Transactions of the Royal Society a-Mathematical Physical and Engineering Sciences* **2006**, *364*, 109.

(44) Schwartzwalder, K.; Somers, A. V. U.S. Patent 3090094, 1963.

(45) Byrne, C. E.; Nagle, D. C. *Materials Research Innovations* **1997**, *1*, 137.

(46) Velev, O. D.; Jede, T. A.; Lobo, R. F.; Lenhoff, A. M. *Nature* **1997**, *389*, 447.

(47) Davis, S. A.; Breulmann, M.; Rhodes, K. H.; Zhang, B.; Mann, S. *Chemistry of Materials* **2001**, *13*, 3218.

(48) Fukasawa, T.; Ando, M.; Ohji, T.; Kanzaki, S. *Journal of American Ceramic Society* **2001**, *84*, 230.

(49) Fitzgerald, T. J.; Michaud, V. J.; Mortensen, A. *Journal of Materials Science* **1995**,

30, 1037.

(50) Iskandar, F.; Abdullah, M.; Yoden, H.; Okuyama, K. *Journal of Applied Physics* **2003**, *93*, 9237.

(51) Oh, C. G.; Baek, Y. Y.; Ihm, S. K. *Advanced Materials* **2005**, *17*, 270.

(52) Zakhidov, A. A.; Baughman, R. H.; Iqbal, Z.; Cui, C. X.; Khayrullin, I.; Dantas, S. O.; Marti, I.; Ralchenko, V. G. *Science* **1998**, *282*, 897.

(53) Scheffler, M.; Colombo, P. *Cellular Ceramics*; Wiley-VCH: Weinheim, 2005.

(54) Tomita, T.; Kawasaki, S.; Okada, K. *Journal of Porous Materials* **2004**, *11*, 107.

(55) Colombo, P.; Modesti, M. *Journal of the American Ceramic Society* **1999**, *82*, 573.

(56) Fujiu, T.; Messing, G. L.; Huebner, W. *Journal of the American Ceramic Society* **1990**, *73*, 85.

(57) Colombo, P.; Hellmann, J. R. *Materials Research Innovations* **2002**, *6*, 260.

(58) Studart, A. R.; Gonzenbach, U. T.; Tervoort, E.; Gauckler, L. J. *Journal of the American Ceramic Society* **2006**, *89*, 1771.

(59) Bardhan, P. *Current Opinion in Solid State & Materials Science* **1997**, *2*, 577.

(60) Stuecker, J. N.; Cesarano, J.; Hirschfeld, D. A. *Journal of Materials Processing Technology* **2003**, *142*, 318.

(61) Wang, C. S.; Zhang, X. W.; Appleby, A. J. *Journal of the Electrochemical Society* **2005**, *152*, A205.

(62) Arita, I. H.; Castano, V. M.; Wilkinson, D. S. *Journal of Materials Science-Materials in Medicine* **1995**, *6*, 19.

(63) Nishihara, H.; Mukai, S. R.; Yamashita, D.; Tamon, H. *Chemistry of Materials* **2005**, *17*, 683.

(64) Kim, J. W.; Taki, K.; Nagamine, S.; Ohshima, M. *Chemical Engineering Science*

2008, *63*, 3858.

(65) Deville, S.; Saiz, E.; Nalla, R. K.; Tomsia, A. P. *Science* **2006**, *311*, 515.

(66) Yan, J.; Chen, Z.; Jiang, J.; Tan, L.; Zeng, X. C. *Advanced Materials* **2009**, *21*, 314.

(67) Araki, K.; Halloran, J. W. *Journal of the American Ceramic Society* **2004**, *87*, 1859.

(68) Chen, R. F.; Wang, C. A.; Huang, Y.; Ma, L. G.; Lin, W. Y. *Journal of the American Ceramic Society* **2007**, *90*, 3478.

(69) Zhang, H. F.; Long, J.; Cooper, A. I. *Journal of the American Chemical Society* **2005**, *127*, 13482.

(70) Mahler, W.; Bechtold, M. F. *Nature* **1980**, *285*, 27.

(71) Mukai, S. R.; Nishihara, H.; Shichi, S.; Tamon, H. *Chemistry of Materials* **2004**, *16*, 4987.

(72) Gutierrez, M. C.; Garcia-Carvajal, Z. Y.; Jobbagy, M.; Rubio, T.; Yuste, L.; Rojo, F.; Ferrer, M. L.; del Monte, F. *Advanced Functional Materials* **2007**, *17*, 3505.

(73) Stokols, S.; Tuszynski, M. H. *Biomaterials* **2004**, *25*, 5839.

(74) Koh, Y. H.; Song, J. H.; Lee, E. J.; Kim, H. E. *Journal of the American Ceramic Society* **2006**, *89*, 3089.

(75) Waschkies, T.; Oberacker, R.; Hoffmann, M. J. *Journal of the American Ceramic Society* **2009**, *92*, S79.

(76) Mukai, S. R.; Nishihara, H.; Tamon, H. *Microporous and Mesoporous Materials* **2008**, *116*, 166.

(77) Mukai, S. R.; Nishihara, H.; Tamon, H. *Catalysis Surveys from Asia* **2006**, *10*, 161.

(78) Mukai, S. R.; Nishihara, H.; Tamon, H. *Chemical Communications* **2004**, 874.

(79) Mukai, S. R.; Nishihara, H.; Tamon, H. *Microporous and Mesoporous Materials* **2003**, *63*, 43.

(80) Mukai, S. R.; Nishihara, H.; Yoshida, T.; Taniguchi, K.; Tamon, H. *Carbon* **2005**, *43*, 1563.

(81) Nishihara, H.; Mukai, S. R.; Fujii, Y.; Tago, T.; Masuda, T.; Tamon, H. *Journal of Materials Chemistry* **2006**, *16*, 3231.

(82) Nishihara, H.; Mukai, S. R.; Tamon, H. *Carbon* **2004**, *42*, 899.

Chapter II

Preparation of Poly(L-lactic acid) Honeycomb Monolith Structure by Unidirectional Freezing and Freeze-drying

2.1. Introduction

Polymer materials with porous structures have attracted great attention due to its potential usage as separation filters,[1] catalyst supports,[2] and scaffolds for biological cells.[3-5] Several techniques have been developed to fabricate polymeric porous structures: porogen leaching,[6] microbead patterning,[7] thermally induced phase separation,[8,9] drying of polymer blend solution,[10] gas foaming,[11] 3D printing,[12] and freeze/freeze-drying.[13-16] For the application of porous polymers as scaffolds for tissue engineering, the porosity, biodegradability, interconnectivity, and morphology are very important.[17-19] Organs such as nerves, bones, blood vessels, and ligaments require a scaffold with an aligned porous structure for their cell proliferation. Thus, the controlled preparation of aligned porous materials in the form of 2D surface pattern or a 3D monolithic structure is critical for this purpose. A promising and novel technique for creating aligned porous structures is a unidirectional freezing method, which is relatively simple and cost effective. Mukai et al.[20] and Nishihara et al.[21] proposed a unidirectional freezing method to prepare a honeycomb monolith silica gel. Recently, several studies extended the unidirectional freezing method to polymers and prepared porous polymeric materials with aligned micro-scale channels (cellular or dendritic honeycomb).[13,14,22] Ma et al.[13] prepared an aligned micro-scale channel structure from poly(L-lactic acid) (PLLA) and poly(L-glycolic acid) (PLGA) by freezing

polymer/dioxane solution in liquid nitrogen. They controlled the freezing direction by insulating the sidewall of the vial or beaker containing the polymer solution. Since their cooling process was in a non-steady state, the cooling rate was not controlled at a constant level. Thus, their porous structure was composed of aligned ladder-like micro-scale channels (dendritic honeycomb) and the aligned channel lengths tended to be short in micrometer range. Zhang et al.[15] introduced a pseudo steady state directional freezing method similar to that of Mukai et al.[20] and prepared aligned porous polymer. Their polymer concentration in solution was higher and silica particles were added to the polymer solution to create a composite. As a result, a ladder-like micro-scale channel structure (dendritic honeycomb) was obtained. They did not investigate any of the conditions for preparing aligned smooth-wall polymer micro-scale channels with a honeycomb structure at a cross sectional area perpendicular to the aligned axis, i.e., cellular honeycomb. There is no publication reporting the preparation of honeycomb monoliths with polymeric porous materials and the key factors determining the structure by the solvent unidirectional freezing method remain unidentified.

In this study, a honeycomb monolith structured porous PLLA (a porous PLLA with smooth-walled microchannels or ladder-like microchannels aligned in parallel to the freezing direction, and a honeycomb structure perpendicular to the aligned direction in cross section) was prepared by combining unidirectional freezing and freeze-drying. The key factors controlling the wall thickness and surface feature of micro-scale channel wall were thoroughly investigated.

2.2. Experimental

2.2.1. Materials

PLLA ($\overline{M_w}$ = 2. 8 × 10^5, $\overline{M_w}/\overline{M_n}$ = 2.24, density = 1.12) was used as received. The average molecular weight, $\overline{M_w}$, the number average molecular weight, $\overline{M_n}$, and polydispersity, $\overline{M_w}/\overline{M_n}$ of the polymer were measured by gel permeation chromatography (Shimadzu, model DGU-20A3). The retention time and molecular weight were calibrated using polystyrene (PS) standards. The density of PLLA was measured using an electro density meter (Mirage, model MD-200S). Dehydrated 1,4-dioxane (Wako pure Chemicals Ind. Ltd., Japan) was used as solvent.

2.2.2. Preparation of Porous Structure

By dissolving PLLA into dehydrated 1,4-dioxane at 323 K. The concentration of PLLA in solution was changed at four levels, 3, 5, 7, and to 10 wt% so as to see the effect of polymer concentration on porous structure. After it was cooled down to room temperature, the solution was poured into a polypropylene (PP) test tube with a thickness of 1.2 mm, 100 mm in length, and 10 mm in diameter. The solution was unidirectionally frozen by immersing the test tube into a liquid nitrogen bath at a constant rate. The liquid level of nitrogen in the cooling bath was lowered at a rate of 2.5 cm h^{-1} due to evaporation. The actual tube immersion rate (freezing rate) to the liquid nitrogen became smaller than the set point value. In this dissertation, the actual immersion rate, which was subtracted by 2.5 cm h^{-1} from the set point value, was used to describe the experimental condition. The tube immersion rate was changed in the

range from 3.5 to 17.5 cm h^{-1}. After freezing the solution completely, the solidified sample was freeze-dried at 268 K for 4 days. To investigate the effect of water on the porous structure, especially the ladder-like channel structure, distilled water was added to the PLLA/1,4-dioxane solution. The water concentration varied in the range from 0.04 to 2.0 wt%.

2.2.3. Morphology Characterization

The microstructures of the obtained sample were observed by scanning electron microscopy (Tiny-SEM 1540, Technex Lab Co. Ltd.). For SEM observation, the freeze-dried samples were further frozen by liquid nitrogen to prevent deformation, and cut with a razor blade in both parallel and perpendicular directions to the freezing direction. The prepared sample was coated with gold-palladium *in vacuo*.

2.2.4. Measurement of Density and Porosity of Porous Materials

The volume of the freeze-dried sample, V_S, was calculated by measuring the sample dimensions carefully. The sample mass, M_S was measured using an eclectic balance (AUW220D, Shimadzu). The porosity, P_S, was calculated from M_S, V_S, and density of PLLA, D_{PLLA} (1.12 g cm^{-3}) by following equation.

$$P_S = 1 - M_S / (V_S D_{PLLA}) \tag{2.1}$$

2.3. Results and Discussion

2.3.1. Resulting Honeycomb Monolith Structure

Honeycomb monolith structure was successfully prepared from a 7 wt% polymer solution without water by unidirectional freezing at a tube immersion rate of 3.5 cm h^{-1} into a liquid nitrogen bath. After freezing the solution completely, the solidified sample was freeze-dried at 268 K (Fig. 2.1). Figs. 2.1a and b, respectively, show a photographic image and SEM image of porous PLLA prepared from a 7 wt% polymer solution without water by unidirectional freezing at a tube immersion rate of 3.5 cm h^{-1}. Fig. 2.1b shows that the honeycomb monolith structure was established in the obtained porous PLLA. Channel structure was created in cross section parallel to the freezing direction, and honeycomb structure was created in cross sectional area perpendicular to the freezing direction. Fig. 2.1c clearly shows the honeycomb pattern created in cross section perpendicular to the freeze direction. Fig. 2.1d shows that micro-scale channels with smooth walls were aligned in parallel to the freeze direction. The length of the aligned channel was longer than 1 cm.

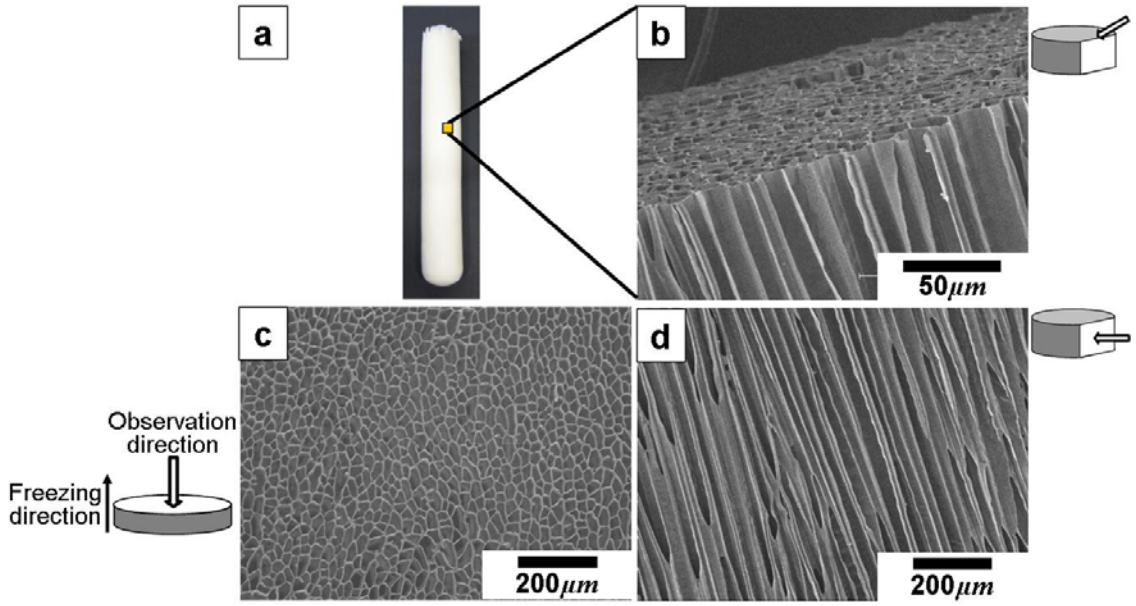

Figure 2.1. (a) Photographic image of porous PLLA prepared from PLLA 7 wt%/dehydrated 1,4-dioxane solution with a tube immersion rate of 3.5 cm hr^{-1}, (b-d) SEM micrographs of (b) honeycomb monolith structure taken at a tilted angle, (c) Cross sectional area perpendicular to freezing direction, and (d) Cross sectional area parallel to freezing direction.

2.3.2. Effect of PLLA Concentration

To investigate the effect of PLLA concentration on the porous structure, four PLLA/1,4-dioxane solutions, of which the polymer weight percentage in solutions were different, were frozen unidirectionally at a constant tube immersion rate of 3.5 cm h^{-1}. Fig. 2.2 shows the SEM micrographs of the porous PLLA materials prepared from these four different solutions. As can be seen, the aligned porous structures were created with all PLLA materials. The walls of the aligned channels were smooth in the porous materials prepared from solutions with polymer concentrations up to 7 wt% (Figs. 2.2a-c and e-g). In the case of freezing in the 10 wt% PLLA solution, the channel

surface morphology was changed from smooth to a ladder form (dendritic honeycomb) and the channels were interconnected to its neighbors by small pores (Figs. 2.2d and h). Fig. 2.3 shows the average diameter and the number density of micro-scale channels in unit area against the polymer concentration. Fig. 2.4 illustrates the average wall thickness against the polymer concentration. The channel diameter, the number density of channels, and the wall thickness were measured from SEM micrographs. The wall thickness increased with an increase in PLLA concentration. The average channel diameter increased and the number density of channels decreased as the polymer concentration was increased.

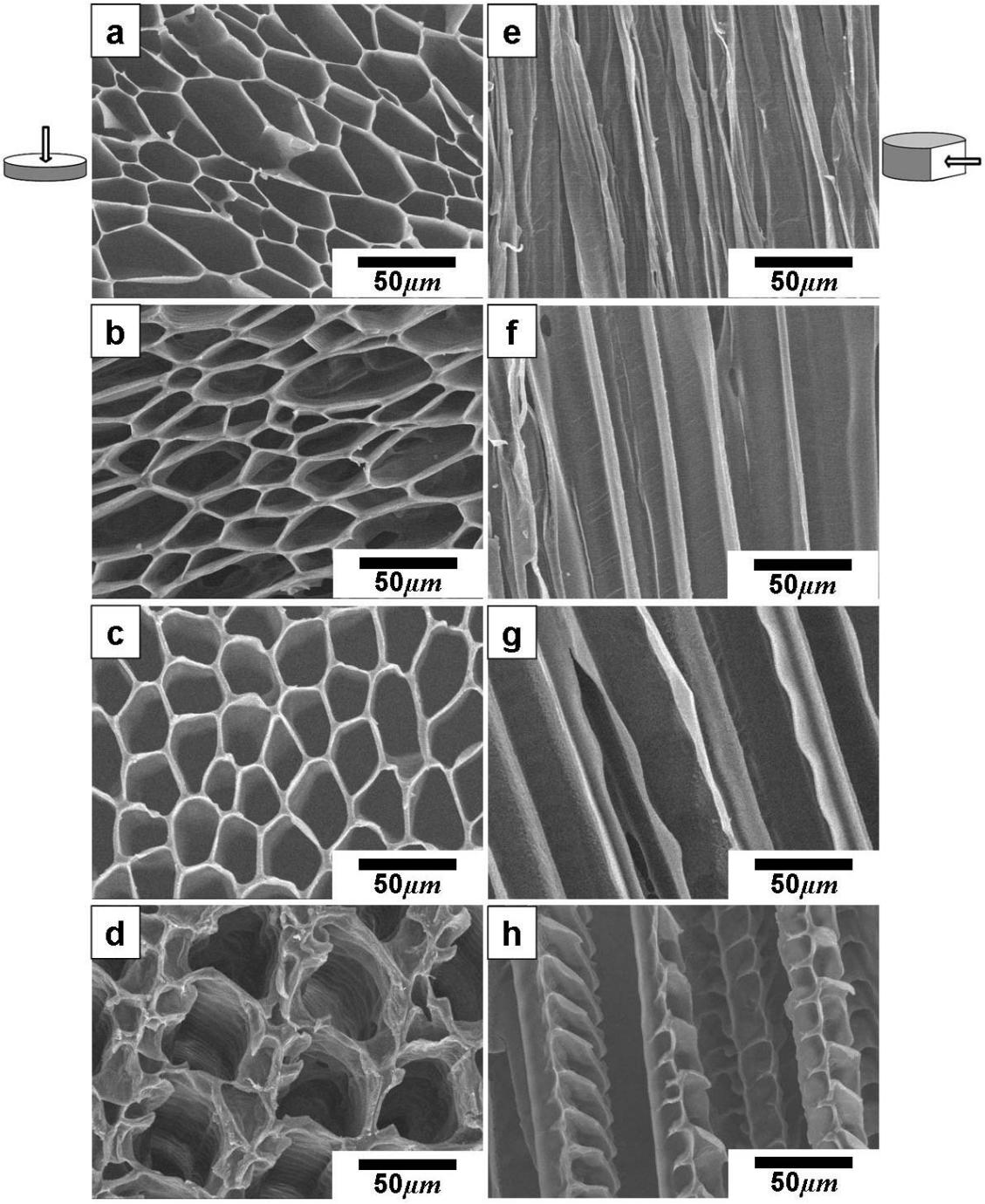

Figure 2.2. Effect of PLLA concentration in solution- SEM micrographs of porous PLLA prepared from PLLA/dehydrated 1,4-dioxane solution at the same immersion rate of 3.5 cm hr^{-1} : (a-d) Cross sectional area perpendicular to freezing direction, (e-h) Cross sectional area parallel to freezing direction, (a and e) 3 wt% of PLLA, (b and f) 5 wt% of PLLA, (c and g) 7 wt% of PLLA , and (d and h) 10 wt% of PLLA.

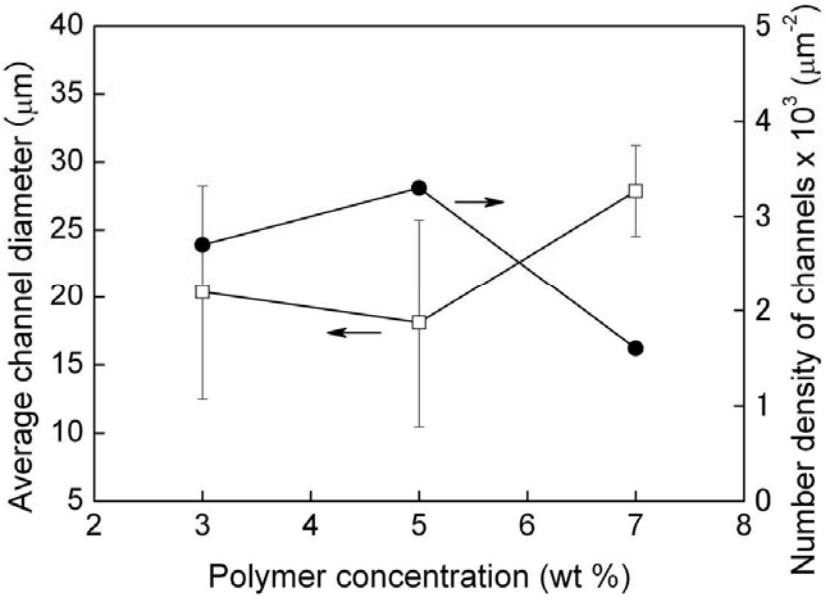

Figure 2.3. Average channel diameter and number density of microchannels per unit area perpendicular to the freezing direction vs. PLLA concentration. (□) average channel diameter and (●) number density.

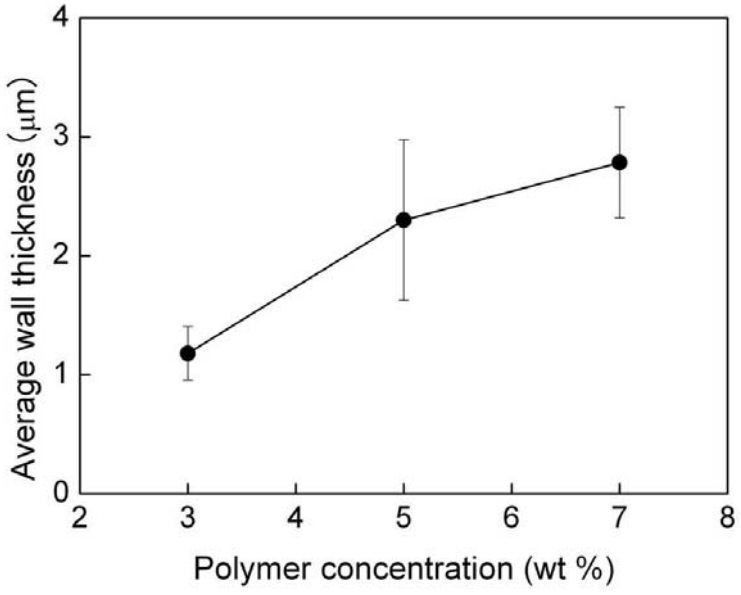

Figure 2.4. Average wall thickness of microchannels vs. PLLA concentration.

2.3.3. Effect of Water Addition

To investigate the effect of water as structure modifier, solutions with different water concentrations and different PLLA concentrations were frozen by immersing the PP tube into liquid nitrogen at a rate of 3.5 cm h^{-1}. Figs. 2.5 and 2.6 show SEM micrographs of the obtained porous PLLA with 7 wt% PLLA solutions. As shown in Fig. 2.5, the porous structure was dramatically changed with the addition of water. The porous PLLA prepared from a solution with 0.04 wt% water content showed a transitional surface morphology from a smooth wall micro-scale channel structure, cellular honeycomb, to a ladder-like channel with an interconnected structure, dendritic honeycomb (Figs. 2.5a and d and 2.6a and d). In the case of the solution with 0.12 wt% water content, a highly ordered interconnected structure was observed (Figs. 2.5b and e and 2.6b and e). For the solution with 2.00 wt% of water content, the number of interconnected pores between the channels was drastically increased (Figs. 2.5c and f and 2.6c and f). The structure resembles the superdendrite crystal observed by Ragnarsson et al.[23] PLLA as well as 1,4-dioxane is likely to contain moisture. The experimental results suggest that small amount of water has dramatic effect on the porous structure, and it is important to control moisture in materials used to prepare honeycomb monolith structures by the unidirectional freeze-drying method. The lack of moisture control may be a reason that honeycomb monolith structures were not created in previous study.[13]

We summarized the effect of water and PLLA concentration as a 2D graph. Fig. 2.7 shows that the porous structure of PLLA is affected by the water content. The morphology shifted from honeycomb monolith structure to transitional structure and then to interconnected structure, and finally highly interconnected structure as function

of the water concentration. However, it was not related with PLLA concentration.

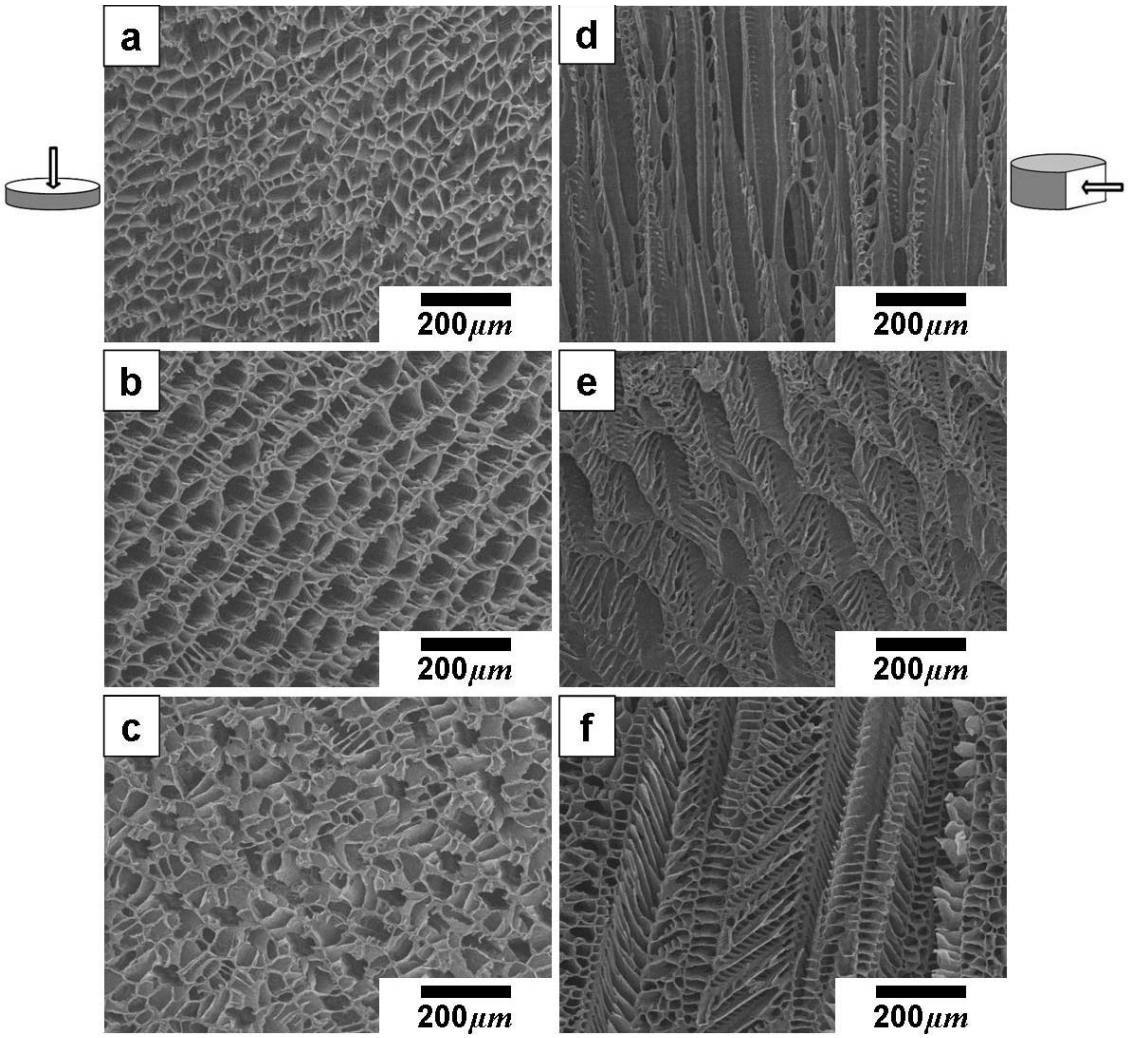

Figure 2.5. Effect of water on structure - SEM micrographs of porous PLLA prepared from 7 wt% of PLLA / 1,4-dioxane solution: (a-c) Cross sectional area perpendicular to the freezing direction, (d-f) Cross sectional area parallel to the freezing direction, (a and d) 0.04 wt% of water, (b and e) 0.12 wt% of water, and (c and f) 2.00 wt% of water.

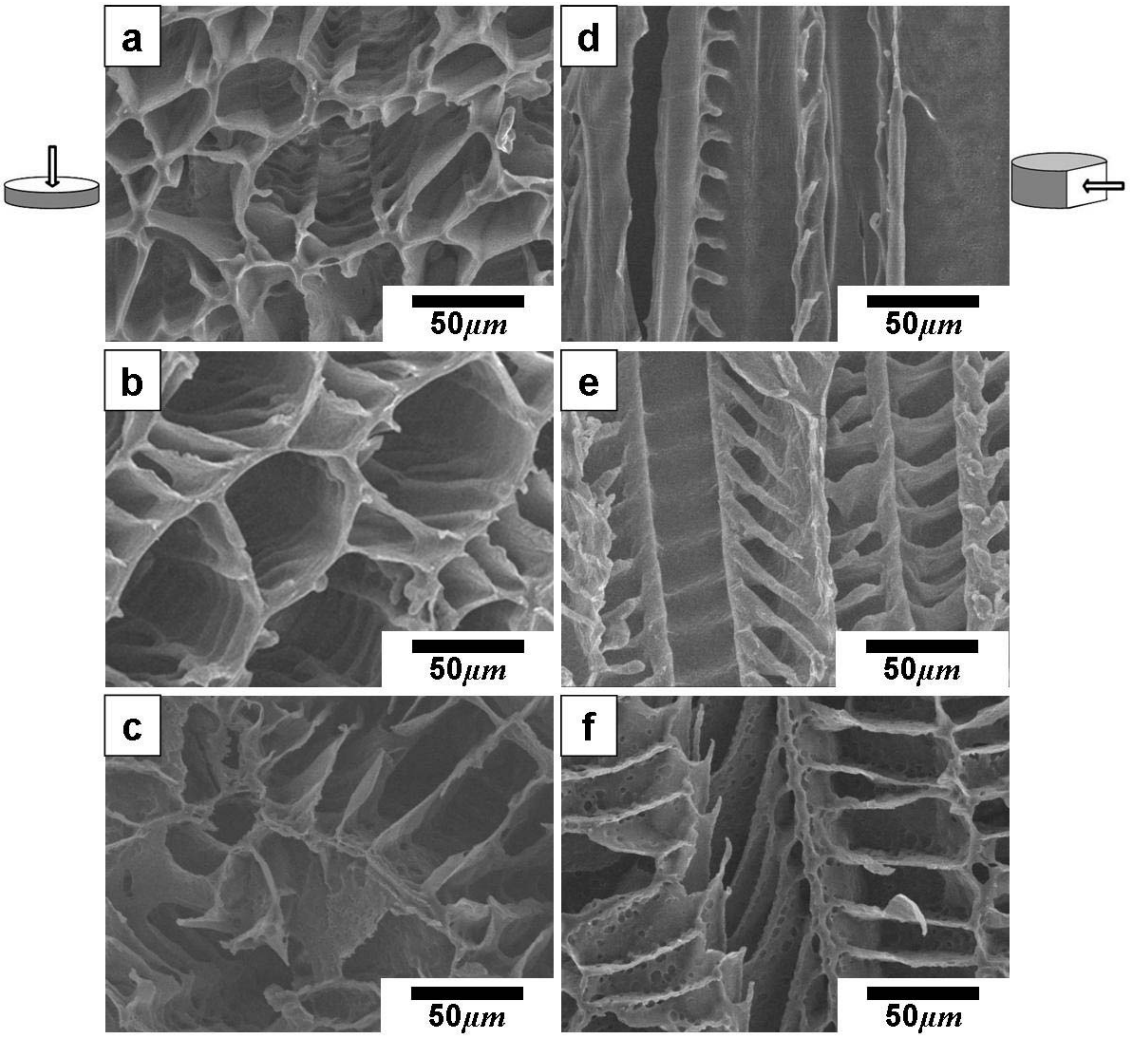

Figure 2.6. Enlarged SEM micrographs of porous PLLA prepared from 7 wt% of PLLA / 1,4-dioxane solution: (a-c) Cross sectional area perpendicular to the freezing direction, (d-f) Cross sectional area parallel to the freezing direction, (a and d) 0.04 wt% of water. (b and e) 0.12 wt% of water, and (c and f) 2.00 wt% of water.

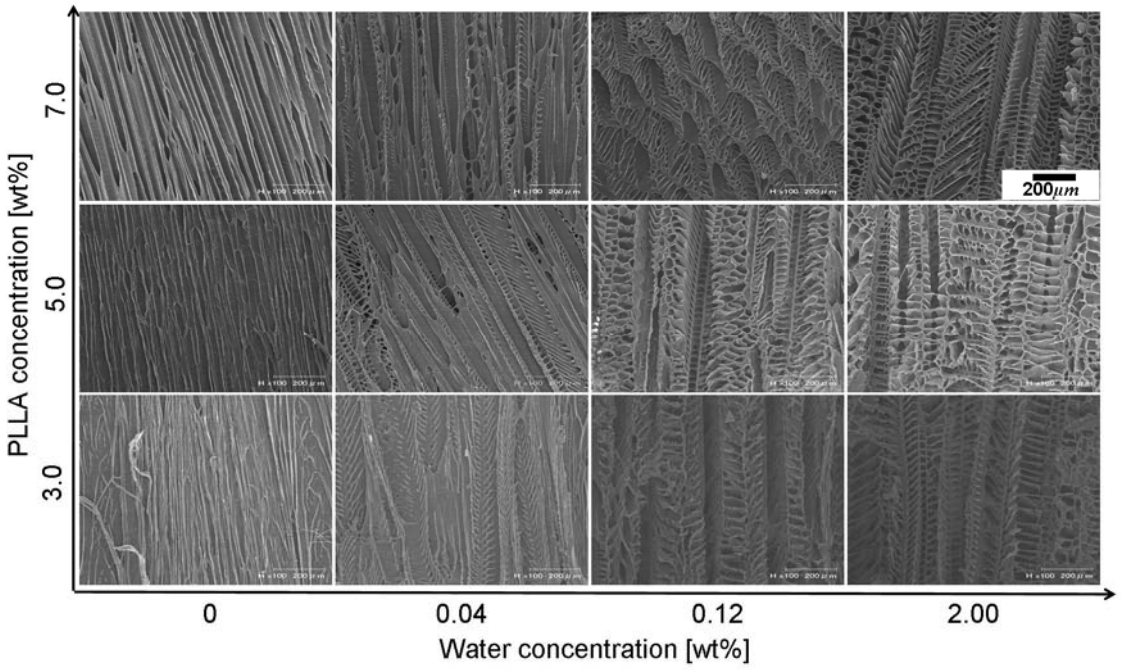

Figure 2.7. Effect of water and PLLA concentration on the porous structure of PLLA.

2.3.4. Effect of Freezing Rate

Fig. 2.8 shows SEM micrographs of a sample cross sectioned perpendicular to the aligned microchannels of the porous PLLA prepared from a 7 wt% solution at two different immersion rates of 7.5, and 17.5 cm h^{-1}. As can be seen, the average diameter of channels decreased with an increase in the immersion rate, which is equivalent to the effects of the cooling rate. This trend coincides with the result of Zhang et al.[15] They measured average spacing of ice crystal of poly(vinyl alcohol) aqueous solution with temperature gradient plate and microscope. The average diameter and number density of channels for three different freezing rates were measured from SEM micrographs and illustrated in Figs. 2.9 and 2.10. The average diameter and wall thickness decreased with an increase in the immersion rate. This is because rapid cooling increases the

degree of supercooling and leads to the enhancement of crystal nucleation of 1,4-dioxane. This result shows that channel diameter and the size of the honeycomb can be controlled by the freezing rate.

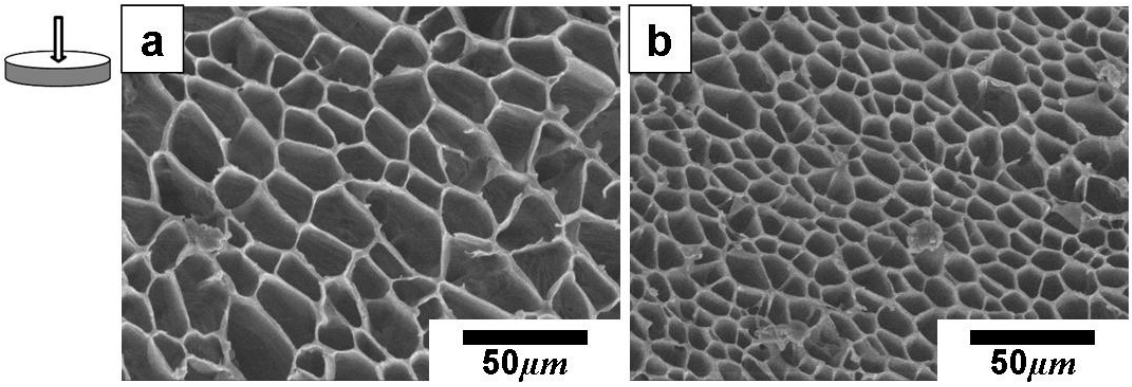

Figure 2.8. Effect of tube immersion rate on honeycomb structure- SEM micrographs of porous PLLA prepared from 7 wt% of PLLA/dehydrated 1,4-dioxane solution at the cross sectional area perpendicular to the freezing direction: immersion rate of (a) 7.5 cm hr^{-1} and (b) 17.5 cm hr^{-1}

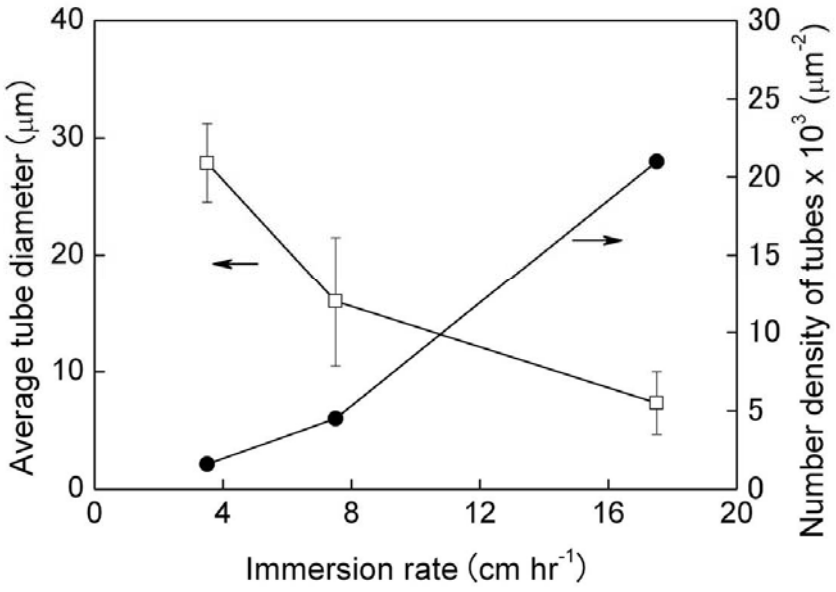

Figure 2.9. Average channel diameter and number density of channels per unit area perpendicular to the freezing direction vs. immersion rate. (□) average channel diameter and (●) number density of channel.

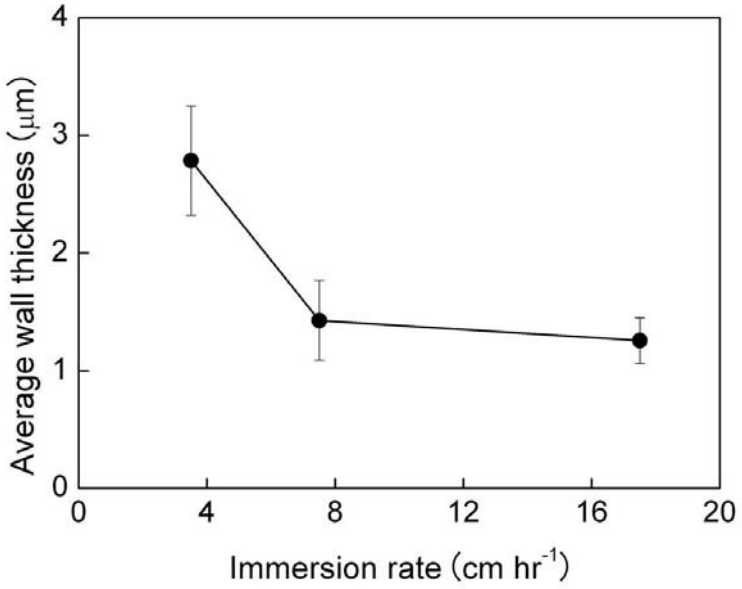

Figure 2.10. Average channel wall thickness vs. immersion rate.

2.3.5. Bulk Density and Porosity

The bulk density and porosity of the resulting porous PLLA is summarized in Table 2.1. The bulk density and porosity were changed by the PLLA concentration in solution. As the concentration increased, the channel wall thickness and density increased and the porosity decreased. It was also noticed that the bulk density and the porosity were affected neither by freezing rate nor by water content.

Table 2.1. Density and porosity of PLLA porous structure

PLLA Concentration [wt%]	Immersion Rate [cm hr^{-1}]	Water Content [wt%]	Bulk Density [g cm^{-3}]	Porosity
3	3.5	Not added	0.057	0.95
5	3.5	Not added	0.097	0.91
7	3.5	Not added	0.145	0.87
7	7.5	Not added	0.140	0.88
7	17.5	Not added	0.128	0.89
7	3.5	0.04	0.148	0.87
7	3.5	0.16	0.147	0.87
7	3.5	2.00	0.136	0.88
10	3.5	Not added	0.091	0.83

2.3.6. Formation Mechanism of Aligned Porous Structures

As shown in Fig. 2.11, for the case in which a single phase solid is formed, the equilibrium concentration of solute in the solid at the interface between solid and liquid is different from the equilibrium concentration of solute in the liquid adjacent to it. In the case of unidirectional freezing, solute is expelled continuously from solid and diffuse toward liquid phase. This causes the pile up of impurities near the solid-liquid interface. The steady state solution of solute distribution was derived for unidirectional freezing by Tiller et al.[24]

$$C_L = C_0\left(1+\frac{1-n}{n}e^{-\frac{V}{D_L}Z}\right) \tag{2.2}$$

C_0 : The initial concentration of solute in the solution

Z : Distance from solid-liquid interface

D_L : Diffusion coefficient of solute in the liquid

V : The constant growth velocity of the interface

n : The partition coefficient given by the ratio of the equilibrium concentration of solute on the solid side of the interface to that on the liquid side of the interface.

As illustrated in Fig. 2.12, higher solute concentration near the solid-liquid interface lowers the melting point in that region. Thus the effective temperature driving of crystal growth is decreased and the crystal growth rate is retarded. This causes the instability of liquid-solid interface that is called constitutional supercooling. When the degree of supercooling is large during the crystallization process, Mullins-Sekerka

instability occurs and the planar interface usually breaks up into cellular or dendritic structures.[23,25] Details of Mullins-Sekerka insatiability was described in chapter V and appendix I.

The porous structure was created by templating the aligned solvent crystals that were formed during unidirectional freezing. In the course of unidirectional freezing, PLLA and impurities were expelled from solvent crystals to the liquid phase and the constitutional supercooling condition was established at the interface. As shown in Fig. 2.13a, the increment of solute concentration in the solid-liquid interface is higher than the increment of solute concentration in the original solution because the difference of equilibrium solute concentration between liquid phase and solid phase increases with the increase of solute concentration in the original solution (Fig. 2.11a). The higher concentration of water and impurities in the solution causes the higher degree of supercooling. Thus, the degree of Mullins-Sekerka instability increased due to the impurity-induced reduction of the freezing point of the solution. The instability created dendrite-type branched crystals. As a result, the unidirectional freezing created ladder-like channels in the presence of water. The interconnectivity of channels increased as the instability increased. As described by Tiller et al.,[24] the concentration gradient of solute increases by the decrease of diffusivity. It is obvious that the diffusivity is decreased with the increase of polymer concentration. This also can induce higher degree of Mullins-Sekerka instability (Fig. 2.13b).

There are some differences in the porous structures between ladder-like channels prepared in the presence of water and ladder-like channels produced with a high-concentration of polymer solution. As shown in Figs. 2.6c and f, small pits, 2 ㎛ in diameter, could be observed on the channel wall. The formation mechanism of these

small pits can be speculated as follows: water was expelled from 1,4-dioxane crystal and concentrated on the solid-liquid interface due to the lower freezing point of water than that of 1,4-dioxane (m.p. 11.8 ˚C). An increase in water caused a liquid-liquid phase separation of polymer solution on the interface before the solution was completely frozen. Since water acted as an anti-solvent to PLLA,[9] the liquid-liquid phase separation created small pits on the channel wall.

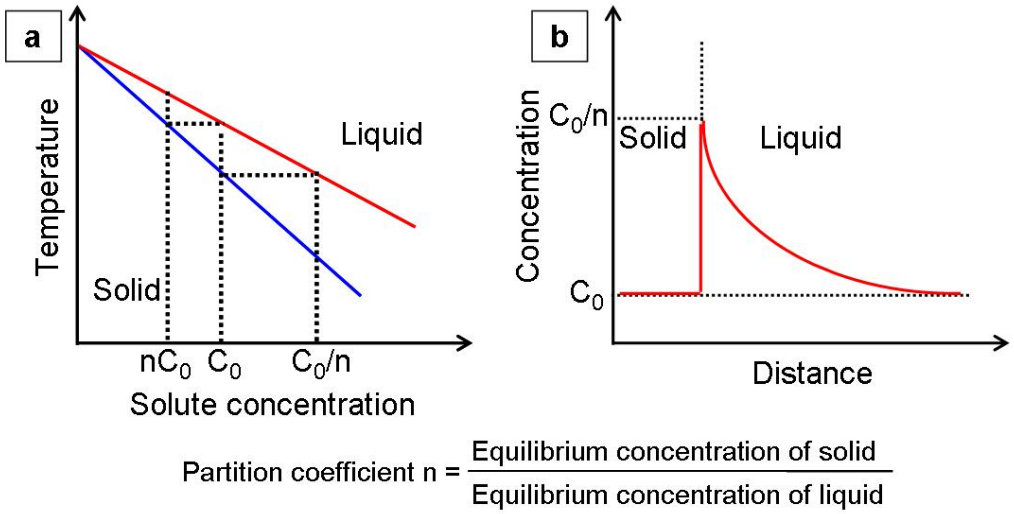

Figure 2.11. The redistribution of solute during the unidirectional freezing of dilute solution. a) portion of phase diagram of binary solution and b) distribution of solute at steady state condition.

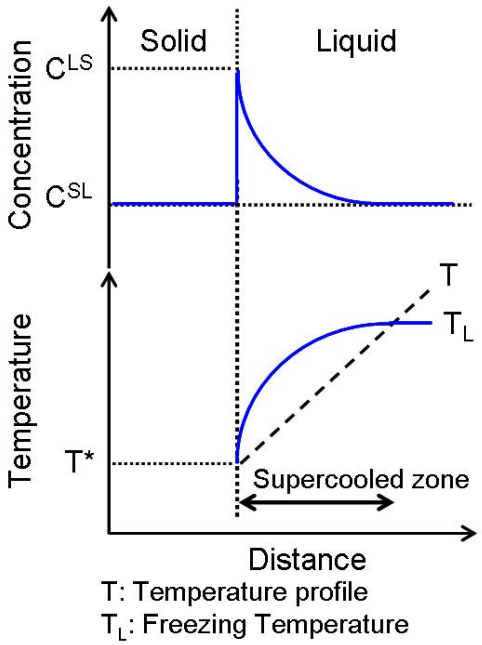

Figure 2.12. Constitutional supercooling.

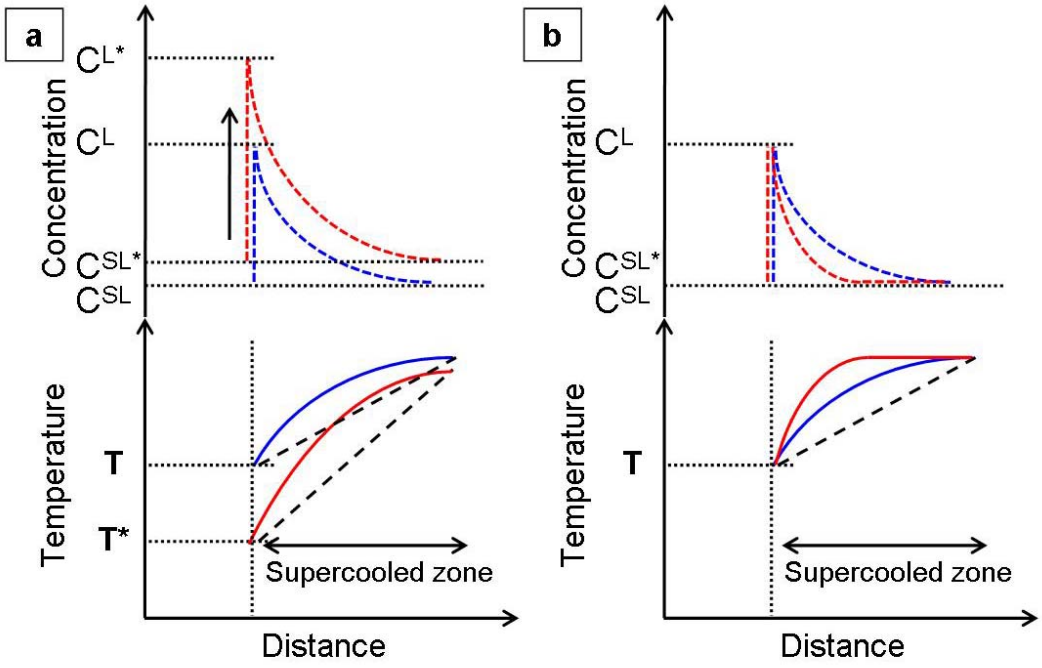

Figure 2.13. The change of constitutional supercooling degree. a) the effect of solute concentration and b) diffusivity of solute. Red line indicates higher degree of constitutional supercooling.

2.4. Conclusion

In this chapter, honeycomb monolith structures of PLLA were successfully prepared by thermally induced solid-liquid phase separation and subsequent solvent sublimation. Water content and polymer concentration are key factors of creating ladder-like structures in aligned microchannels. The interconnectivity of aligned channels can be controlled by adding water to the solution. The average diameter and the number density of channels per unit cross section perpendicular to the aligned direction were controlled by polymer concentration. The wall thickness of channels was controlled by PLLA concentration. We expect that this method has great potential for the design of aligned porous materials for tissue, organic electronics, micro fluidics, and membrane engineering.

2.5. Reference

(1) Kersting, R. *Synthetic Polymer Membrane*; Wiley: Newyork, 1985.

(2) Deleuze, H.; Schultze, X.; Sherrington, D. C. *Polymer* **1998**, *39*, 6109.

(3) Nishikawa, T.; Nishida, J.; Ookura, R.; Nishimura, S. I.; Wada, S.; Karino, T.; Shimomura, M. *Materials Science & Engineering C-Biomimetic and Supramolecular Systems* **1999**, *8-9*, 495.

(4) Nishikawa, T.; Nonomura, M.; Arai, K.; Hayashi, J.; Sawadaishi, T.; Nishiura, Y.; Hara, M.; Shimomura, M. *Langmuir* **2003**, *19*, 6193.

(5) Langer, R.; Vacanti, J. P. *Science* **1993**, *260*, 920.

(6) Kothapalli, C. R.; Shaw, M. T.; Wei, M. *Acta Biomaterialia* **2005**, *1*, 653.

(7) Lu, M. H.; Zhang, Y. *Advanced Materials* **2006**, *18*, 3094.

(8) Nam, Y. S.; Park, T. G. *Biomaterials* **1999**, *20*, 1783.

(9) Hua, F. J.; Park, T. G.; Lee, D. S. *Polymer* **2003**, *44*, 1911.

(10) Kim, J. K.; Taki, K.; Ohshima, M. *Langmuir* **2007**, *23*, 12397.

(11) Taki, K.; Nitta, K.; Kihara, S.; Ohshima, M. *Journal of Applied Polymer Science* **2005**, *97*, 1899.

(12) Lee, M.; Dunn, J. C. Y.; Wu, B. M. *Biomaterials* **2005**, *26*, 4281.

(13) Ma, P. X.; Zhang, R. Y. *Journal of Biomedical Materials Research* **2001**, *56*, 469.

(14) Zhang, H.; Cooper, A. I. *Advanced Materials* **2007**, *19*, 1529.

(15) Zhang, H. F.; Hussain, I.; Brust, M.; Butler, M. F.; Rannard, S. P.; Cooper, A. I. *Nature Materials* **2005**, *4*, 787.

(16) Zhang, R. Y.; Ma, P. X. *Journal of Biomedical Materials Research* **1999**, *44*, 446.

(17) Ma, P. X.; Zhang, R. Y.; Xiao, G. Z.; Franceschi, R. *Journal of Biomedical Materials Research* **2001**, *54*, 284.

(18) Agrawal, C. M.; Ray, R. B. *Journal of Biomedical Materials Research* **2001**, *55*, 141.

(19) Sung, H. J.; Meredith, C.; Johnson, C.; Galis, Z. S. *Biomaterials* **2004**, *25*, 5735.

(20) Mukai, S. R.; Nishihara, H.; Tamon, H. *Chemical Communications* **2004**, 874.

(21) Nishihara, H.; Mukai, S. R.; Yamashita, D.; Tamon, H. *Chemistry of Materials* **2005**, *17*, 683.

(22) Zhang, H. F.; Long, J.; Cooper, A. I. *Journal of the American Chemical Society* **2005**, *127*, 13482.

(23) Ragnarsson, R.; UTTER, B.; BODENSCHATZ, E. In *Proceedings of the Materials Research Society Symposium* 1997; Vol. 481, p 65.

(24) Tiller, W. A.; Jackson, K. A.; Rutter, J. W.; Chalmers, B. *Acta Metallurgica* **1953**, *1*, 428.

(25) Mullins, W. W.; Sekerka, R. F. *Journal of Applied Physics* **1964**, *35*, 444.

Chapter III

Preparation of Porous Poly(L-lactic acid) Honeycomb Monolith Structure by Phase Separation and Unidirectional Freezing

3.1. Introduction

Chapter II presented a method for preparing a honeycomb monolith structured porous poly(L-lactic acid) (PLLA) by unidirectional freezing and freeze-drying. This structure has micro-scale channels aligned parallel to the freezing direction and a honeycomb structure perpendicular to the freezing direction. It was shown that water content and polymer concentration in the initial polymer solution were key factors of changing the interconnectivity of the aligned microchannels. The interconnectivity can be increased by increasing the degree of supercooling of the solvent crystal. However, the uniformity of the honeycomb structure decreased with the increase of the interconnectivity, because the large degree of supercooling enhanced the transition of solvent crystalline structure from cells to dendrites and the resulting microchannel wall texture from smooth to rough.

Interest in the honeycomb monolith structure is dramatically increasing[1-7] because of its inherently high contact efficiency and the controllability of its morphology. This structure has great potential as a catalyst support,[8] catalyst,[9] substrate for drug delivery,[10] or bioscaffold.[11,12] Despite of these prospects, the honeycomb monolith structure (especially when prepared using cellular type solvent crystals as a template)

has a shortcoming in its poor interconnectivity. The lack of connections between microchannels can cause them to become plugged, decreasing the contact efficiency and increasing the pressure drop. If the honeycomb monolith structure were used as a catalyst or catalyst support, plugging of the microchannels would lead to a serious deterioration in reaction performance. For a bioscaffold application, plugging of the microchannels would disturb the proliferation of cells. Poor interconnectivity between microchannels would also cause slow cell growth during cultivation because of the lack of oxygen and inefficiency of nutrient supply and waste elimination.[13,14] When the bioscaffold is made of biodegradable polymers, the degradation rate is strongly affected by the morphology and porosity of the 3D structure.[15,16] Since the degradation rate of the scaffold is very important for cell regeneration,[14,17,18] this characteristic must be controllable. One of the solutions for increasing interconnectivity among the microchannels is to create open pores in the microchannel walls.

In this chapter, liquid-liquid phase separation is integrated with the unidirectional freezing method to prepare a honeycomb monolith structure with highly interconnected microchannels while maintaining the cellular honeycomb structure. As described in chapter I, phase separation of a polymer solution is one of useful methods to create and control polymer morphology. There are several methods to induce phase separation such as thermally induced phase separation (TIPS),[19-22] solvent induced phase separation (SIPS),[23-25] and nonsolvent induced phase separation (NIPS).[26-29] These phase separation methods utilize solubility difference as a driving force for morphology development.

Phase separation of blended polymer was induced by temperature reduction and crystallization of the solvent during unidirectional freezing, causing the microchannel

walls of the honeycomb monolith structure to have an open porous structure, but not changing the degree of supercooling to keep the cellular type solvent crystalline structure. Poly (ethylene glycol) (PEG) was used to blend with the PLLA to prepare a porous PLLA structure. PEG has a very unique property in that the hydrophilicity and solubility of PEG depend on its molecular weight.[30,31] This is because its end group is hydrophilic and the repeating unit is hydrophobic. Thus, PEG can be easily dissolved into water or relatively nontoxic hydrophilic solvents such as ethanol.[32] It can be used to design several interesting polymer blend morphologies by means of its water solubility and controllable hydrophilicity.[33] After preparing a single phase PEG/PLLA/1,4-dioxane solution, the solution was unidirectionally frozen by immersing the sample into liquid nitrogen at a constant rate. 1,4-Dioxane crystals nucleated in the solution and grew in the freezing direction. Using the crystalline structure as a template, the PLLA/PEG mixture was solidified and structured. The mixture of PEG/PLLA formed a sea-and-island morphology, where PEG domains were dispersed in the PLLA matrix, in the honeycomb monolith structure walls depending upon the ratio of two polymers. The solvent crystals were then sublimated by freeze-drying, and the aligned porous structure was developed. The porous structure in the microchannel walls of the honeycomb monolith was created by selectively leaching out the PEG domains.

3.2. Experimental

3.2.1. Materials

PLLA (U0z B-0) was kindly supplied by Toyota Motor Corporation. Four kinds of PEG with weight average molecular weights of 600, 2000, 4000, and 6000 were

purchased from Wako Chemicals Ind. Ltd. PLLA and PEG are dried at room temperature in vacuo for 2 days before using and stored in a vacuum desiccator to avoid absorption of moisture. The gel permeation chromatography (GPC) results of the PLLA and PEG used in this study are summarized in Table 3.1. The weight average molecular weight, $\overline{M_w}$, the number average molecular weight, $\overline{M_n}$, and the polydispersity, $\overline{M_w}/\overline{M_n}$, of the polymer were measured by gel permeation chromatography (Shimadzu, model DGU-20A3). The retention time and molecular weight were calibrated using PEG standards. Dehydrated 1,4-dioxane (Wako Chemicals Ind. Ltd., Japan) and ethanol (Wako Chemicals Ind. Ltd., Japan) were used as a solvent and rinsing liquid, respectively. Dehydrated 1,4-dioxane was stored in a desiccator.

Table 3.1. GPC Results of PLLA and PEG used in this study

Materials	M_w	M_n	M_w/M_n
PLLA	280,000	125,000	2.24
PEG600	440	500	1.14
PEG2000	1,710	1,870	1.09
PEG4000	2,380	2,600	1.09
PEG6000	8,240	8,650	1.05

3.2.2. Preparation of Porous Structure

The PLLA and PEG were codissolved in dehydrated 1,4-dioxane at 323 K. The preparation of the solution was conducted in a working hood to avoid absorption of moisture. A single phase solution could be prepared at this temperature simply by

agitating the mixture with a magnetic stirrer until the solution became transparent. Several solutions were prepared at 7 wt % total polymer concentration with different blend ratios of PLLA to PEG (90/10, 70/30, and 50/50) to test the effect of the PLLA/PEG blend ratio on the morphology of the honeycomb monolith structure and the microchannel walls. After cooling to room temperature, the solution was poured into a polypropylene (PP) test tube of 1.2 mm in wall thickness, 100 mm in length, and 10 mm in diameter, and frozen unidirectionally by immersing the test tube into a liquid nitrogen bath at a constant rate of 2.0 cm h^{-1}. The PP tube was closed with a cap to prevent absorption of moisture. We inserted a syringe needle to avoid pressure depression in the tube, which is caused by freezing of the solution. After freezing the solution completely, the solidified sample was freeze-dried at 268 K for 4 days. The honeycomb monolith structures were then soaked in ethanol for 7 days, and the ethanol was replaced every 12 h to ensure complete leaching of the PEG. After leaching, the samples were soaked in tert-butyl alcohol for 1 day, with the alcohol being replaced every 12 h. Finally, the wet samples were freeze-dried at 273 K.

3.2.3. Morphology Characterization

The microstructures of the resulting polymer samples were observed by scanning electron microscopy (SEM; Tiny-SEM 1540, Technex Laboratory Co. Ltd.). For SEM observation, the freeze-dried samples were frozen by liquid nitrogen to prevent deformation and cut with a razor blade both parallel and perpendicular to the direction of the first freezing (i.e., the unidirectional freezing that created the honeycomb monolith structure). The samples were coated with gold-palladium in vacuo. Since the freezing rate was changed until a pseudo-steady state was established in the

unidirectional freezing process, we cut out the sample piece from 5 cm above the bottom of the tube for SEM observation and penetration tests. This is because Tamon and co-workers[2,8,34] reported that the pseudo-steady state of the ice growth initiated at least 5 cm above the bottom of the tubes and continued until the tube was completely frozen.

3.2.4. Measurement of Freezing Point and Cloud Point

To measure the freezing point depression of PEG/1,4-dioxane solution and to elucidate the phase transitions of the PLLA/PEG/1,4-dioxane solution, cloud point and freezing point measurements were conducted by adopting a simple laser scattering scheme (Keyence,LV-H62).[25] The detail scheme was illustrated in Figure 3.1. The effects of PEG concentration and weight average molecular weight on the cloud point as well as the freezing point were investigated by using PEG/1,4-dioxane binary solutions and PLLA/PEG/1,4-dioxane ternary blend solutions with different PEG concentrations and PEG weight average molecular weights. A sample cell containing a solution was immersed in a temperature controlled water bath, and the temperature of the solution was directly measured with a thermocouple. The whole system was set up in a temperature controlled incubator (ESPEC Corp., LU-113). The temperature was increased until the solution became homogeneous, and then it was decreased at a rate of 0.125 K min^{-1} for the cloud point measurement and at a rate of 0.2 K min^{-1} for the freezing point measurement. Under continuous stirring, the solution became turbid because of phase separation and finally crystallized. The intensity of a laser beam (650 nm wavelength) transmitted through the solution was monitored. The typical time histories of the transmitted intensity and the temperature of the sample solution are

plotted in Figure 3.1b. The cloud point was determined from the temperature at which the light intensity changed drastically. The freezing temperature was determined by the highest temperature of a plateau in the temperature-time curve.

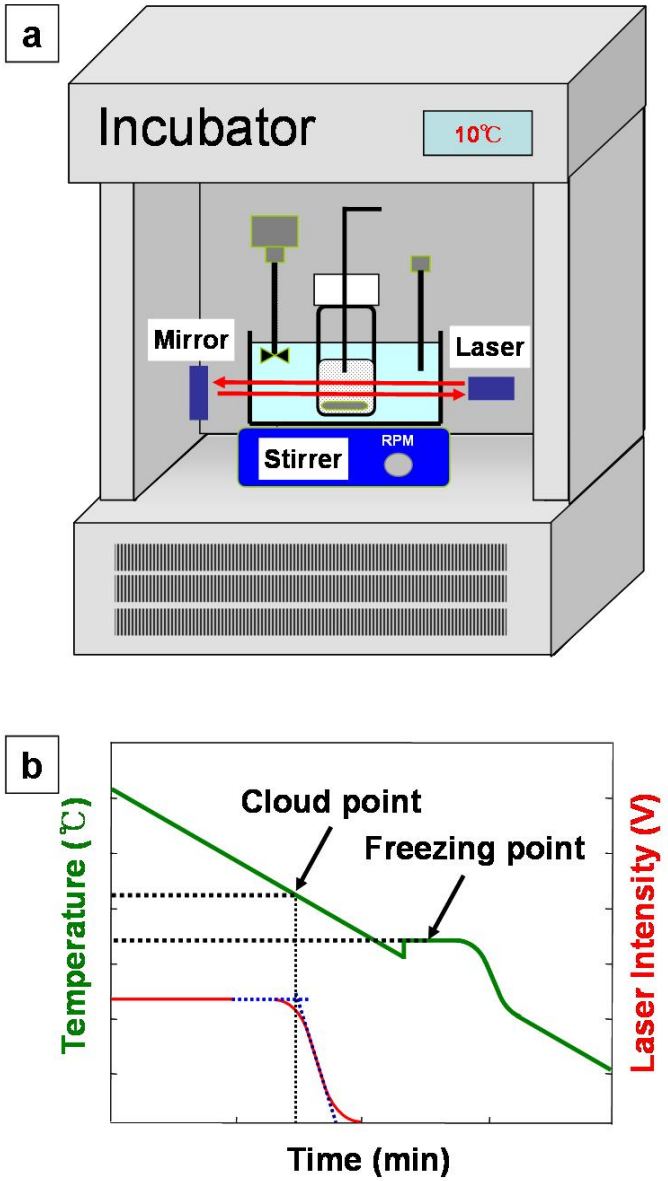

Figure 3.1. Measurement of cloud point and freezing point. a) schematic diagram of experimental apparatus for the measurement of cloud point and freezing point and b) typical graph of laser intensity and temperature

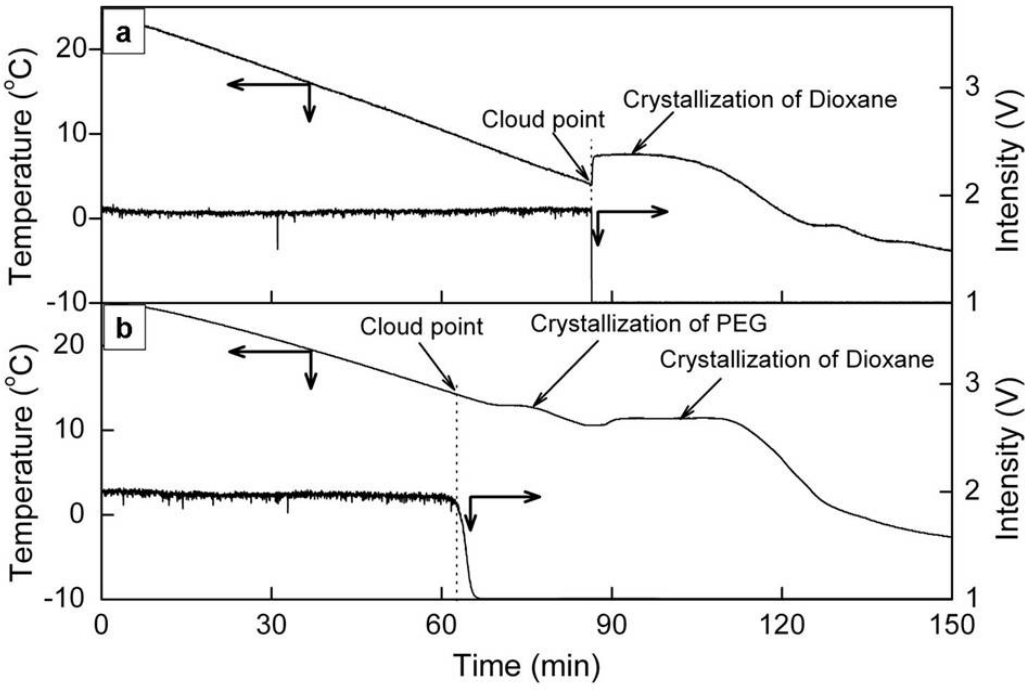

Figure 3.2. Measurement of cloud point and freezing point of PEG/1,4-dioxnae solution. (a) PEG600/1,4-dioxane solution with 10 wt% PEG concentration., (b) PEG2000/1,4-dioxane solution with 30 wt% PEG concentration.

3.3 Results and Discussion

3.3.1. Phase Diagram

The cloud point and freezing points of PEG/1,4-dioxane solutions with different PEG molecular weights and concentrations were measured. Figure 3.2a shows the temperature-time curve of a PEG600/1,4-dioxane solution with 10 wt % PEG concentration. A plateau region was observed just after the laser light intensity drastically dropped. During this plateau, the dioxane crystallized. On the other hand, the temperature-time curve for the PEG2000/1,4-dioxane solution with 30 wt % PEG

concentration had two plateau regions as shown in Figure 3.2b. The temperature of the first plateau region was apparently higher than the solvent freezing temperature. The first plateau may indicate the liquid-liquid phase separation of PEG2000 rich and 1,4-dioxane rich phases, with the crystallization of 1,4-dioxane following in the second plateau. At the beginning of the first plateau, the laser light intensity decreased gradually because of the liquid-liquid phase separation. After the liquid-liquid demixing, the 1,4-dioxane was crystallized. It was difficult to observe the second drop in the intensity corresponding to the crystallization because the intensity had already dropped to an undetectable level at the cloud point. The difference in the intensity curves between the PEG600 and PEG2000 solutions was caused by the difference in the solubility of PEG in 1,4-dioxane. PEG600 is more soluble than PEG 2000 in 1,4-dioxane. However, even for the PEG600 solution, the liquid-liquid phase separation occurred before 1,4-dioxane crystallization until the PEG concentration exceeded 70 wt%.

Figure 3.3 shows the freezing point curves of PEG/dehydrated 1,4-dioxane solutions with different PEG molecular weights and concentrations. The freezing point decreased as the PEG concentration increased up to 50 wt %. The depression of the freezing point with the polymer concentration was very small for the high molecular weight PEGs, while it was very large for PEG600. This effect might be caused by the fact that the molar ratio of higher molecular weight PEG was lower than that of PEG600 when compared at the same weight concentration. Kimizuka et al. reported that the degree of freezing point depression of water/PEG solutions become smaller as the molecular weight of PEG increases.[35] The liquid-liquid phase separation of higher molecular weight PEG is another factor affecting the degree of freezing point

depression. The solubility of PEG in 1,4-dioxane decreases with increasing PEG molecular weight, since the hydrophilicity decreases with increasing molecular weight. The liquid-liquid demixing temperature, at which the PEG was phase separated from the dehydrated 1,4-dioxane solution, increases with increasing polymer concentration as well as increasing polymer molecular weight. Thus, for higher molecular weight PEG, the polymer concentration in solution was reduced by liquid-liquid phase separation before the dioxane began to freeze. As a result, the freezing point was not strongly affected by the polymer concentration for higher molecular weight PEG.

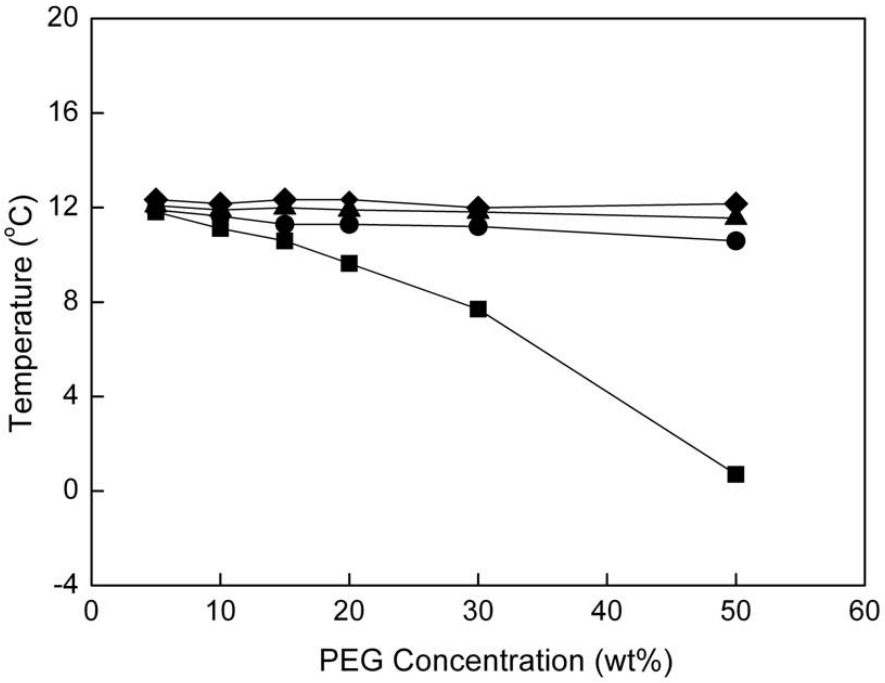

Figure 3.3. Freezing point curves of PEG/1, 4-dioxane solution. (■) PEG600, (●) PEG2000, (▲) PEG4000, and (♦) PEG6000.

The cloud point of the PLLA/PEG/1,4-dioxane ternary systems with different PEG molecular weights and compositions was investigated using the aforementioned method.

It is hard to obtain the phase diagram by achieving thermodynamical equilibrium condition when the cloud point measurement was conducted. It is because the phase separation occurs under a supersaturated condition. Furthermore, it was reported that the cloud point curves did not coincide with the bimodal curve when polydispersed polymers were used; however, the cloud point curves could be utilized as a good criterion dividing the homogeneous and the phase separated regions and explaining the phase separation mechanism as well as the effect of quenching depth in the TIPS process.[22,36] Therefore, we used the measured cloud point curves to evaluate the effects of PEG molecular weight and PLLA/PEG blend ratio on the morphology of the channel wall. Figure 3.4 shows the liquid-liquid demixing temperature of the ternary systems with different PEG molecular weights. In making these measurements, the total polymer concentration was varied while keeping the PLLA/PEG weight ratio at 50/50. The liquid-liquid demixing temperature increased with increasing total polymer concentration as well as increasing PEG molecular weight. The PLLA/ PEG600 solution did not show PEG phase separation before the dioxane started freezing until the PEG concentration exceeded 25 wt %. It was impossible to measure the cloud point of the PLLA/PEG600 solution for PEG concentrations over 25 wt % because of the very high viscosity of the solution. Figure 3.5 shows the change in the liquid-liquid demixing temperature of PLLA/PEG6000/dehydrated 1,4-dioxane systems versus total polymer concentrations and PLLA to PEG ratio with four PLLA/PEG weight ratios. The liquid-liquid demixing temperature apparently increased with increasing total polymer concentration for all PEG blend ratios.

From the freezing point depression data, the crystallization temperature of the polymer blend solutions during unidirectional freezing can be estimated to be 283 K.

The compositions of the PLLA/PEG/1,4-dioxane ternary system, for which the liquid-liquid phase separation occurred at temperatures below the freezing point, 283 K, were calculated with the measured liquid-liquid demixing temperature and total polymer composition data. The calculated compositions were plotted on a phase diagram (Figure 3.6). The solubility of the PLLA/PEG blend in 1,4-dioxane decreased with increases in both the PEG blend ratio and the PEG molecular weight. The results for the ternary system agreed with those for the PEG/1,4-dioxane binary solution.

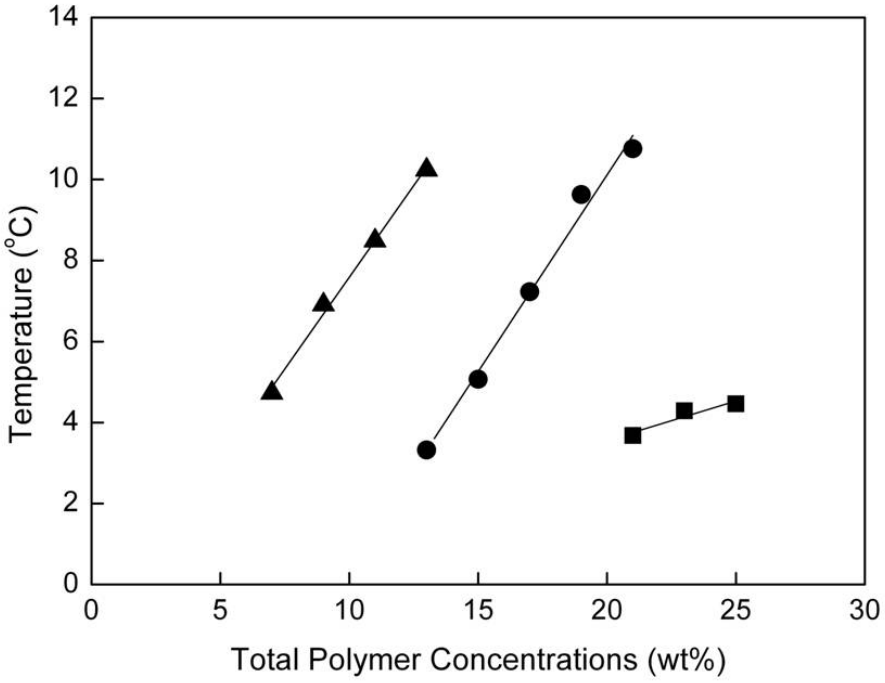

Figure 3.4. Cloud point curves of PLLA/PEG/1, 4-dioxane ternary solution with different PEG weight average molecular weight at 50/50 PLLA/PEG blend ratio. (■) PEG2000, (●) PEG4000, and (▲) PEG6000.

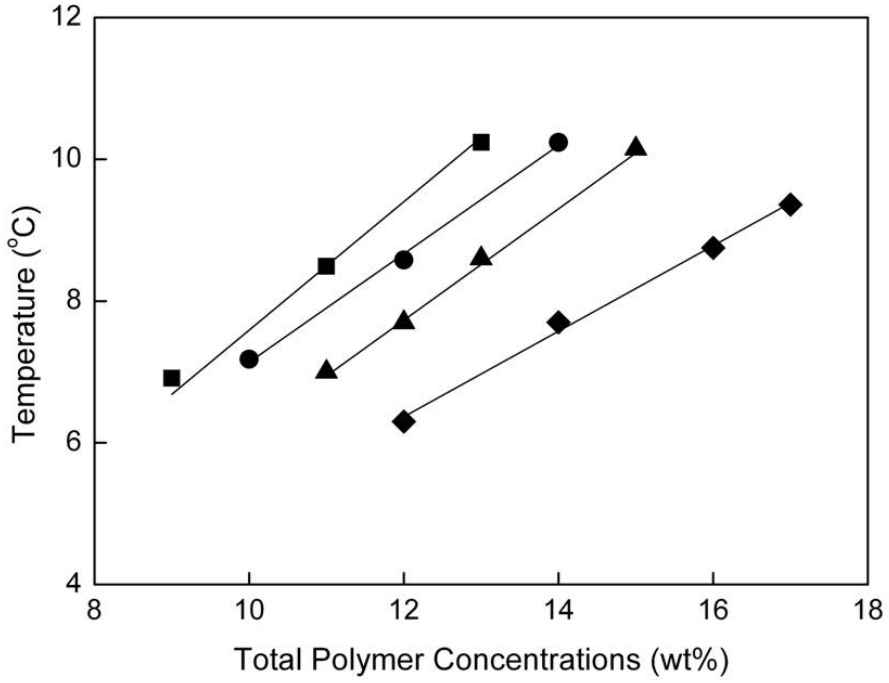

Figure 3.5. Cloud point curves of PLLA/PEG6000/1, 4-dioxane ternary solution with different blend ratios of PLLA to PEG of 90/10, 80/30, 70/30 and 50/50. (■) PLLA/PEG=50/50, (●) PLLA/PEG=70/30, (▲) PLLA/PEG=80/20, and (♦) PLLA/PEG=90/10.

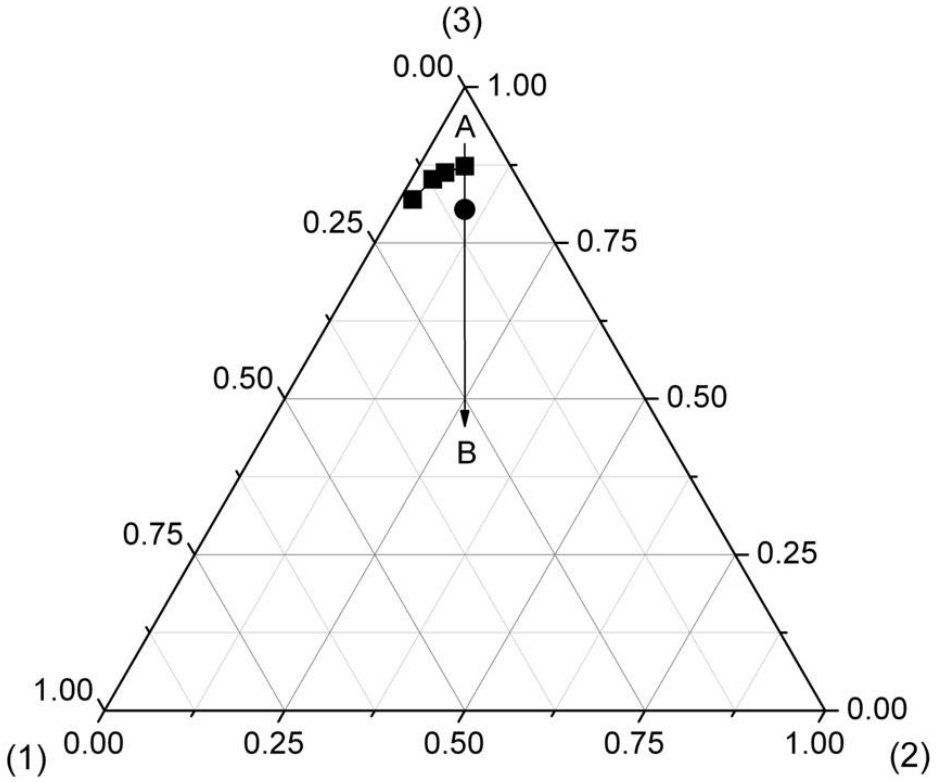

Figure 3.6. Phase diagram of PLLA (1)/PEG (2)/1, 4-dioxane (3) solutions at 283K. (●) PEG4000 and (■) PEG6000. The region A indicates homogeneous phase and the region B indicates liquid-liquid phase separated region.

3.3.2 Resulting Porous Honeycomb Monolith Structure

Figure 3.7a and b shows a pair of SEM micrographs of a PLLA/PEG blend after unidirectional freezing and freeze-drying but before leaching treatment. This sample was made from a PLLA/PEG 6000/1,4-dioxane solution with 7 wt % total polymer concentration, 90/10 PLLA/PEG ratio, and 2.0 cm h^{-1} immersion rate. Figure 3.7a shows a cross-sectional view perpendicular to the freeze direction. Figure 3.7b shows a view parallel to the freeze direction. Both micrographs clearly show a honeycomb

monolith structure, which has smooth-walled microchannels aligned along the freezing direction and a honeycomb structure in cross section (cellular honeycomb).

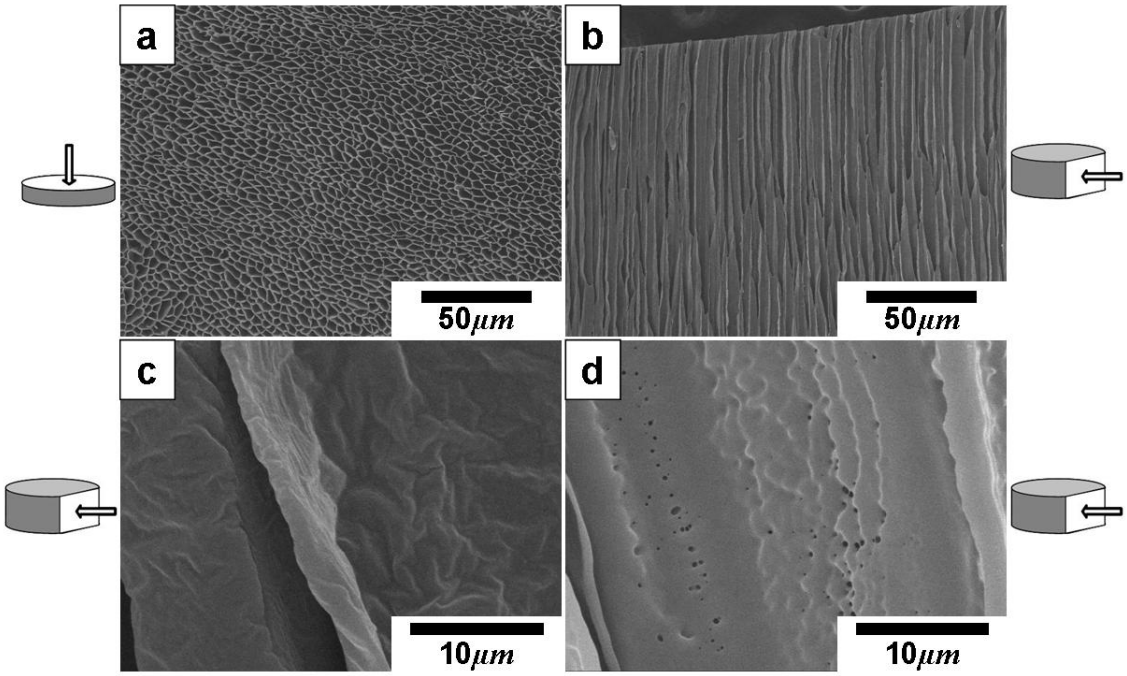

Figure 3.7. SEM micrographs of honeycomb monolith structures prepared from PLLA/PEG6000 blend (90/10) and dehydrated 1,4-dioxane solution (7 wt% total polymer concentration). (a) cross sectional area perpendicular to freezing direction, (b)-(c) cross sectional area parallel to freezing direction, (d) cross sectional area parallel to freezing direction after leaching with ethanol

We prepared several SEM micrographs of cross sectional area parallel to freezing direction. As shown in Figure 3.8, the pore channels in the z-axis are homogeneous in shape. The maximum observable length of the aligned microchannel was longer than 1 cm. We also conducted the ink-penetration test with methylene blue/ethanol solution to confirm the unidirectional pore channels in the z-axis were open. The similar test was

previously done by Nishihara et al.[8] As shown in Figure 3.9, we dropped dye solution on the center of top of honeycomb monolith structure (about 1.2 cm in length). Dropped dye solution was penetrated to bottom of structure through inner pore channels. This result also shows that pore channels are open.

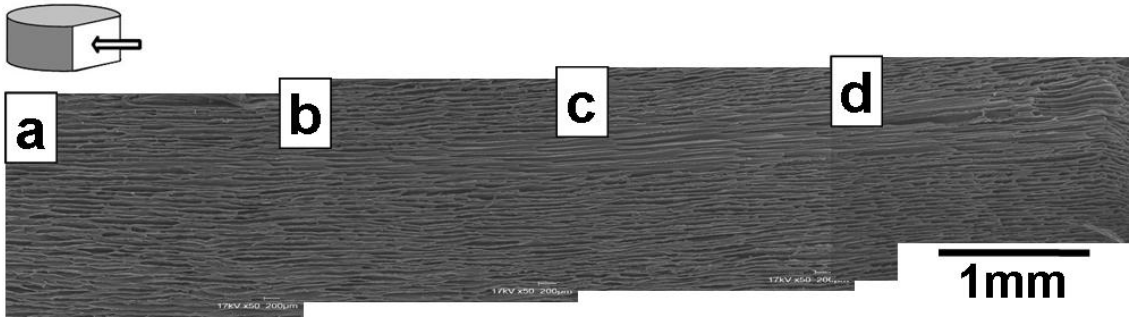

Figure 3.8. Cross sectional areas of honeycomb monolith structure prepared from PLLA/PEG6000 blend (70/30)

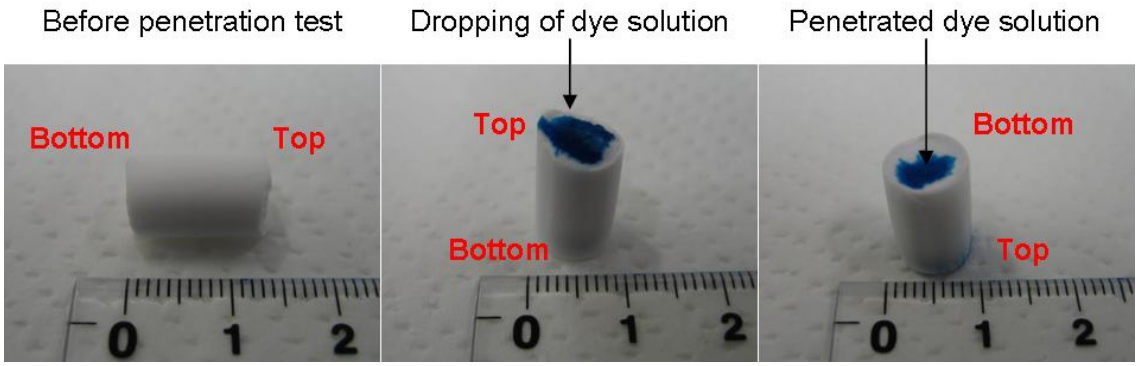

Figure 3.9. Photographic images of penetration test.

As described in previous chapters, the honeycomb monolith structure was created by using the solvent's crystalline structure as a template to solidify the polymer. The crystal was then sublimated by freeze-drying. The solvent was crystallized and grown in the freezing direction by constitutional supercooling. When the degree of supercooling was large, the crystal structure formed dendrite (ladder-like) structures, following the

Mullins-Sekerka instability theory.[37,38] In chapter II, moisture in the polymer acted as an impurity, increasing the instability and enhancing the transition from a cellular to a dendritic structure. In the polymer blends studied in this chapter, the minor polymer did not hinder the creation of smooth-walled microchannels (cellular honeycomb) when the compatibility of both polymers was high.

To prepare micro-honeycomb monolith structures with porous channel walls, the sample was then immersed in ethanol, and the PEG contents were leached out. Figure 3.7c and d shows, respectively, SEM micrographs of a microchannel wall before and after leaching. As can be seen, small pores are observed on the wall after leaching. We measured the weight difference of the samples before and after PEG leaching and confirmed that PEG was successfully removed by leaching treatment.

3.3.3. Effect of PEG Molecular Weight on Honeycomb Monolith Structure

To investigate the effect of PEG molecular weight on the morphology of the honeycomb monolith structure, we varied the PEG molecular weight while keeping the weight ratio of PLLA to PEG at 90/10 and the polymer concentration at 7 wt %. Every sample was prepared by freezing the solution unidirectionally at a constant tube immersion rate of 2.0 cm h^{-1}. Figure 3.10 shows pairs of SEM micrographs of the honeycomb monolith structures made from different PEG molecular weights. The structure made from a PLLA/PEG600 blend solution only exhibited a dendritic (ladder-like) microchannel structure (dendritic honeycomb) as illustrated in Figure 3.10a and e. On the other hand, the honeycomb monolith structures made from the

solutions in which the PEG molecular weight was greater than 2000 had cellular type microchannels (cellular honeycomb), as illustrated in Figure 3.10b-d and f-h. As can be seen in these figures, the character of the microchannels in the honeycomb monolith structure changed with the PEG molecular weight even when the polymer blend ratio and the initial polymer concentration in the solution were kept the same. As described in chapter II, the morphology could be controlled by adding the small amount of water. The morphology of PLLA/PEG600 blend only showed a dendritic (ladder-like) microchannel structure. The results indicated that water content could be highly controlled in the PEG2000, 4000, and 6000 solutions. To confirm the moisture content of PEG600 which was dried and stored in vacuum desiccator, we measured water content of it using Karl Fischer titration method and water content was 388 ppm (max 13.6 ppm in solution). In chapter II, the transitional morphology from cellular honeycomb to dendritic honeycomb occurred at 400 ppm and regular dendritic morphology occurred at 1200 ppm. Thus, it is believe that the water content did not affect the sample structure in this study.

The dendritic microchannel structure appears when the degree of supercooling is larger. As can be seen in Figure 3.3, the degree of freezing point depression induced by the polymer concentration was largest in the PEG600/dioxane solution. When the solvent was crystallized, the polymer was expelled from the crystallizing solvent, and a steep polymer concentration gradient was established at the solid-liquid interface. The degree of freezing point depression becomes larger with increasing polymer concentration, especially for PEG600. A steep gradient of freezing point depression at the solid-liquid interface was also established in association with the polymer concentration gradient. As a result, the degree of Mullins-Sekerka instability became

highest in the PLLA/PEG600 solution and dendritic microchannels were created.

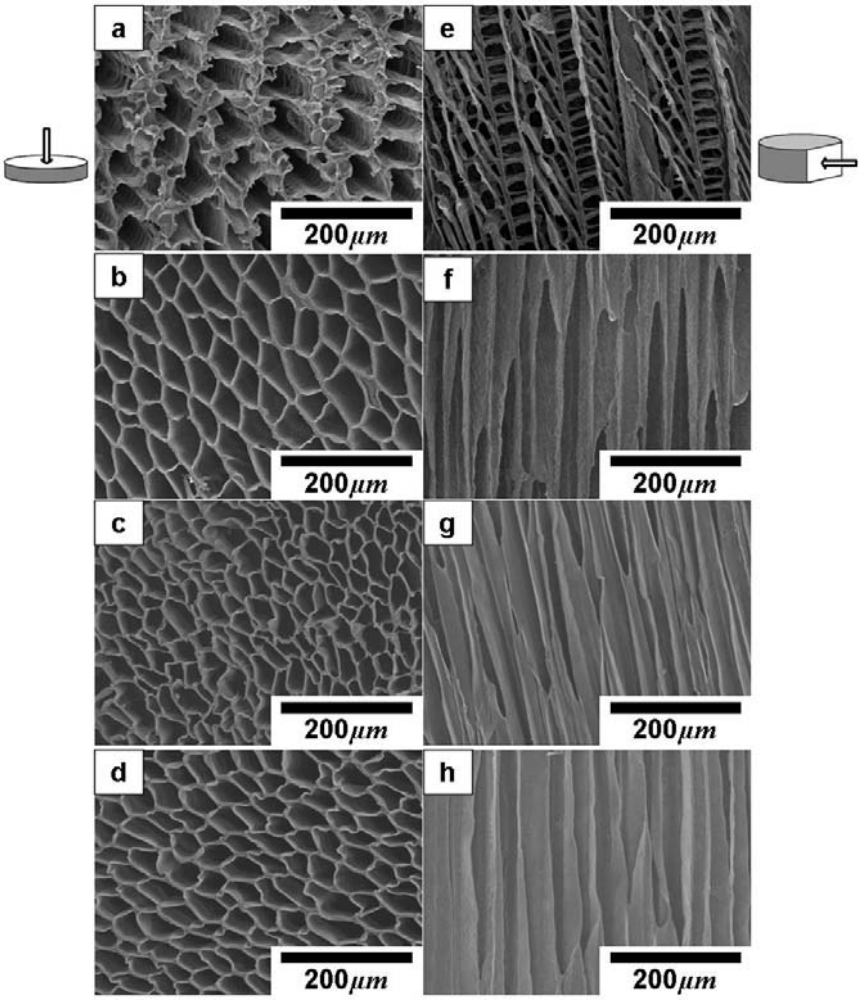

Figure 3.10. Effect of PEG molecular weight on structure - SEM micrographs of honeycomb monolith structures prepared from PLLA/PEG blend (90/10) and dehydrated 1,4-dioxnae solution (7 wt% total polymer concentration). (a)-(d) cross sectional area perpendicular to freezing direction. (e)-(h) cross sectional area parallel to freezing direction. (a) and (e) PEG600, (b) and (f) PEG2000, (c) and (g) PEG4000, and (d) and (h) PEG6000

3.3.4. Effect of PEG Molecular Weight on Pores in the Channel Wall

The effect of PEG molecular weight in the polymer blend solution on the morphology of the pores in the microchannel walls was also investigated. Four PLLA/PEG/1,4-dioxane solutions with different PEG molecular weights (PEG600, PEG2000, PEG4000, and PEG 6000) were prepared and leached in ethanol after creating a honeycomb monolith structure by unidirectional freezing and freeze-drying treatments. Figure 3.11 shows SEM micrographs of pores in the microchannel walls in the structures prepared from four different PEG molecular weight solutions. As shown in Figure 3.11, the pore structures were created in the tube wall by leaching. Note that the scale of Figure 3.11a is different from the others. The pore size was the smallest in the structure prepared from the PLLA/PEG600 solution. The pore size increased, and the number of pores decreased, with increasing PEG molecular weight. From the freezing point and cloud point data illustrated in Figures 3.2 and 3.4-6, one can infer that the liquid-liquid phase separation in the PLLA/PEG600 solution occurred at a lower temperature and a higher total polymer concentration than those in other solutions. The viscosity of the polymer solution when liquid-liquid phase separation occurred was higher in PLLA/PEG600 solution than in other solutions. As a result, the coalescence or aggregation of the precipitated PEG droplets was suppressed by the higher viscosity. The domain size of PEG in the PLLA/PEG blend was therefore smallest in the PLLA/PEG600 blend.

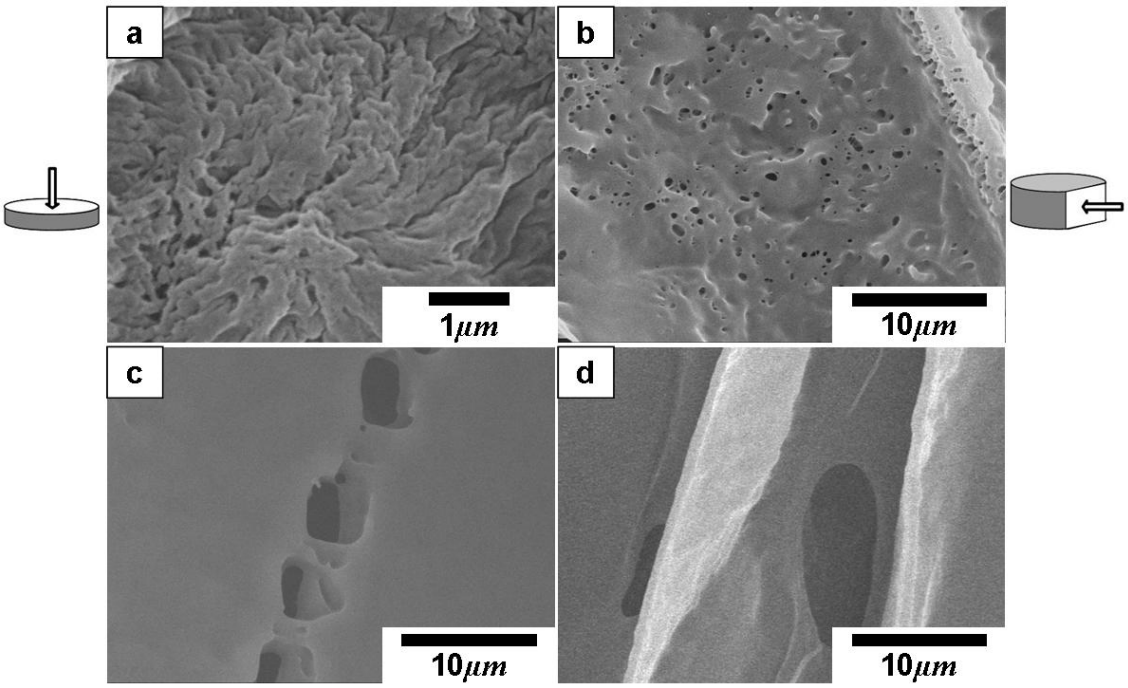

Figure 3.11. Effect of PEG molecular weight on the morphology of channel walls - SEM micrographs of ethanol leached cross sections perpendicular to the freezing direction prepared from PLLA/PEG blend (70/30) and dehydrated 1,4-dioxnae solution (7 wt% total polymer concentration). (a) PEG600, (b) PEG2000, (c) PEG4000, and (d) PEG6000

3.3.5 Effect of PLLA/PEG Blend Ratio on Pore Size in the Microchannel Wall

Figure 3.12 shows SEM micrographs of microchannel walls in honeycomb monolith structures prepared from four PLLA/PEG2000/1,4-dioxane solutions with different PLLA/PEG blend ratios. As can be seen, the pore size increased with increasing PEG content of the polymer. It was clearly observed for both 70/30 and 50/50 blend ratios that the microchannels were connected to each other through these

pores. The effect of the blend ratio on the degree of interconnectivity could be explained by the onset timing of liquid-liquid phase separation and the degree of aggregation of PEG during the unidirectional freezing process. As the PEG content increased in the polymer blend, the onset temperature of liquid-liquid separation increased (as shown in Figure 3.5), and the viscosity of the PLLA/dioxane solution at the moment of phase separation decreased. The lower viscosity enhanced the aggregation of the PEG domains and produced larger pores. The effects of PEG blend ratio and PEG molecular weight (PEG2000, 4000, and 6000) on the pore diameter in the channel wall were analyzed with SEM micrographs, and the results are illustrated in Figure 3.13. The average diameter of the pores on the channel wall increased with the increase in PEG blend ratio as well as the PEG molecular weight. However, in the case of PEG2000, the increase of pore diameter was not so large. The result could be explained by the cloud point curve of PLLA/PEG2000 in Figure 3.4 as follows: The slope of the cloud point curve of PLLA/PEG2000 was gentler than other curves prepared with high molecular weight PEG blend solutions. The average pore diameter could not be measured for PEG600 because the porous structure totally differs from others and the pore diameters were too small to compare with those of the other samples.

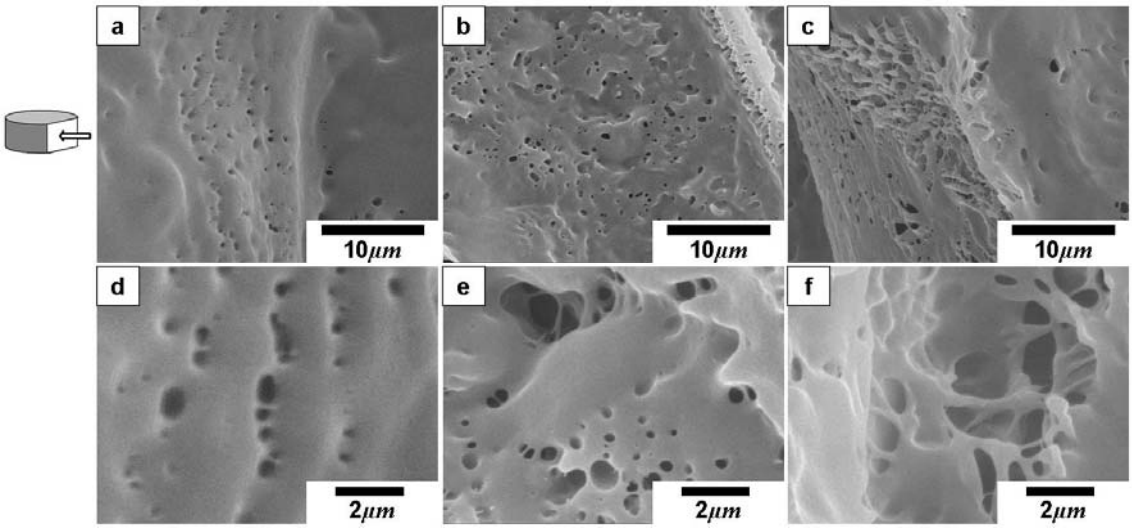

Figure 3.12. Effect of PLLA/PEG blend ratio on the morphology of channel walls - SEM micrographs of ethanol leached cross sections perpendicular to the freezing direction for different PLLA/PEG2000 blend ratios in dehydrated 1,4-dioxnae solutions (7 wt% total polymer concentration). (a) and (d) PLLA:PEG=90:10, (b) and (e) PLLA:PEG=70:30, and (c) and (f) PLLA:PEG=50: 50.

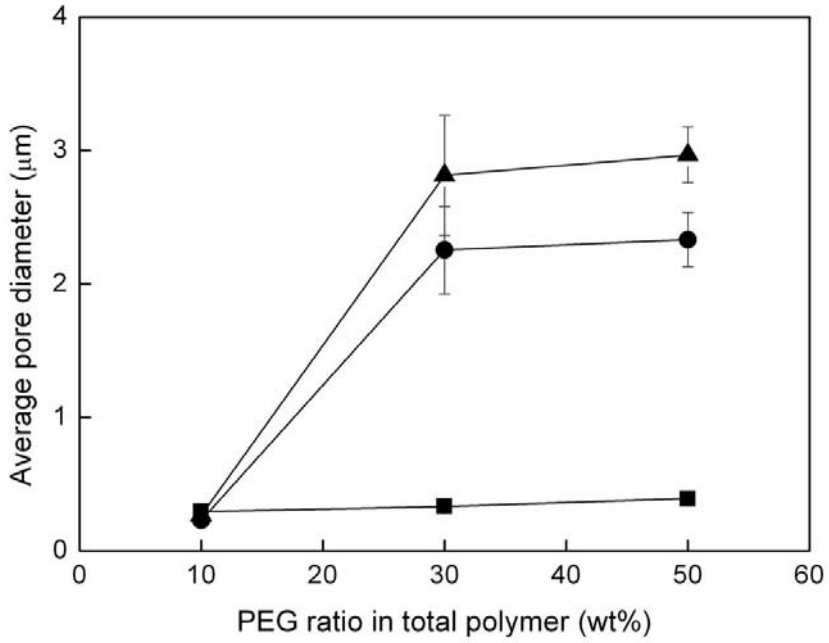

Figure 3.13. Average pore diameter in the channel wall versus PEG blend ratio. (■) PLLA/PEG2000, (●) PLLA/PEG4000, and (▲) PLLA/PEG6000.

3.3.6. Formation Mechanism of Pores on Channel Wall

The pores were created in the microchannel walls from the spaces occupied by the PEG domains in the blended polymer. Understanding the formation mechanism of the PEG domain is important for controlling the pore size. The phase separation of the PEG rich domain from the solution occurs in the course of unidirectional freezing. The phase separation of this process could be regarded as a thermally induced phase separation (TIPS) from the viewpoint that the phase separation was induced by lowering the temperature of the polymer solution. However, the cell morphology created by the unidirectional freezing is different from the one prepared by the conventional TIPS process. The conventional TIPS process uses phase separation between solvent and polymer to create a porous structure even for the case of a polymer-polymer-solvent ternary solution.[39] The cell morphology was determined by its quenching depth and period.[22,36] On the other hand, the cell morphology prepared by the unidirectional freezing was created by two different mechanisms, that is, solvent crystallization and phase separation between two polymers. The polymer-polymer phase separation occurs in the space surrounded by solvent crystal. As we described in chapter II, the unidirectional channel structure was created by templating of the aligned solvent crystals. The solvent was crystallized and grown in the freezing direction due to the constitutional supercooling mechanism. When the degree of supercooling was large during the crystallization process, Mullins-Sekerka instability occurred and created crystals with cellular or dendritic structures.[37,38] While the crystals grow, the polymers are expelled from the solvent crystal. In the course of unidirectional freezing, the concentration of PLLA and PEG in the liquid phase surrounded by 1,4-dioxane crystals increased, and the 1,4-dioxane content decreased (Figure 3.14). The change in solvent

concentration induced a liquid-liquid phase separation; the phase separation of the PEG dispersed domain from the PLLA matrix. The pore morphology in the channel wall was created by the polymer-polymer phase separation. It was difficult to exactly describe the phase separation mechanism of the polymer blend solution surrounded by solvent crystal because we could not observe the initial stage of phase separation. However, the final porous morphology was dominantly determined by coalescence of PEG disperse domains. When the liquid-liquid phase separation occurs at the beginning of solvent crystallization, the precipitated PEG is easily aggregated to form droplets until the solvent is completely crystallized. On the other hand, if the liquid-liquid phase separation occurs toward the end of solvent crystallization, the coalescence of the PEG domains is limited by the viscosity of the polymer solution, where the solvent concentration is reduced by crystallization. As the molecular weight of PEG increases, the solubility of PEG in the solvent decreases, and liquid-liquid phase separation occurs at a lower polymer concentration in the solvent as illustrated in Figure 3.14, resulting in a lower viscosity of the polymer solution. This leads to larger PEG domains in the PLLA matrix and therefore larger pores.

The increase of pore size with increasing PEG blend ratio can be explained by the same principle. That is, the increase in PEG content reduces the polymer concentration at which liquid-liquid phase separation occurs and accelerates coalescence of PEG domains.

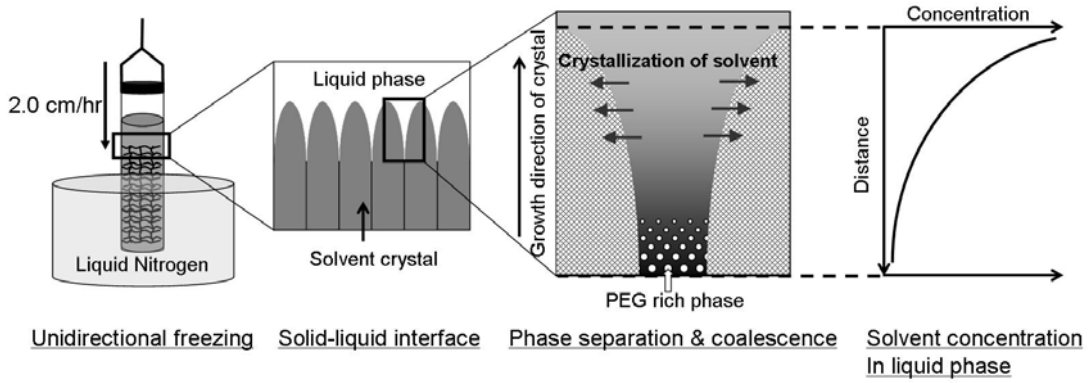

Figure 3.14. Schematic diagram to explain the unidirectional freezing and the phase separation and coalescence of the PEG-rich phase

3.4. Conclusion

In this chapter, honeycomb monolith structured PLLA with micro/submicron scale porous walls was successfully fabricated by combining the unidirectional freezing technique and phase separation of the polymer blend solution. PEG was used to create pores in the microchannel walls in the honeycomb monolith structure. The pore size could be influenced by controlling the onset of liquid-liquid phase separation and solvent crystallization by changing the molecular weight of the PEG as well as the blend ratio. We expect that this method has a potential of improving the contact efficiency of aligned porous materials for tissue scaffolds, catalysts, organic electronics, microfluidics, and membrane engineering.

3.5. Reference

(1) Fukasawa, T.; Deng, Z. Y.; Ando, M.; Ohji, T.; Kanzaki, S. *Journal of the American Ceramic Society* **2002**, *85*, 2151.

(2) Nishihara, H.; Mukai, S. R.; Yamashita, D.; Tamon, H. *Chemistry of Materials* **2005**, *17*, 683.

(3) Mukai, S. R.; Nishihara, H.; Yoshida, T.; Taniguchi, K.; Tamon, H. *Carbon* **2005**, *43*, 1563.

(4) Zhang, H. F.; Hussain, I.; Brust, M.; Butler, M. F.; Rannard, S. P.; Cooper, A. I. *Nature Materials* **2005**, *4*, 787.

(5) Zhang, H.; Cooper, A. I. *Advanced Materials* **2007**, *19*, 1529.

(6) Zhang, H.; Edgar, D.; Murray, P.; Rak-Raszewska, A.; Glennon-Alty, L.; Cooper, A. I. *Advanced Functional Materials* **2008**, *18*, 222.

(7) Todo, M.; Kuraoka, H.; Kim, J.; Taki, K.; Ohshima, M. *Journal of Materials Science* **2008**, *43*, 5644.

(8) Nishihara, H.; Mukai, S. R.; Tamon, H. *Carbon* **2004**, *42*, 899.

(9) Mukai, S. R.; Nishihara, H.; Shichi, S.; Tamon, H. *Chemistry of Materials* **2004**, *16*, 4987.

(10) Gutierrez, M. C.; Garcia-Carvajal, Z. Y.; Jobbagy, M.; Rubio, T.; Yuste, L.; Rojo, F.; Ferrer, M. L.; del Monte, F. *Advanced Functional Materials* **2007**, *17*, 3505.

(11) Stokols, S.; Tuszynski, M. H. *Biomaterials* **2004**, *25*, 5839.

(12) Ma, P. X.; Zhang, R. Y. *Journal of Biomedical Materials Research* **2001**, *56*, 469.

(13) Freed, L. E.; Marquis, J. C.; Nohria, A.; Emmanual, J.; Mikos, A. G.; Langer, R. *Journal of Biomedical Materials Research* **1993**, *27*, 11.

(14) Freed, L. E.; Vunjaknovakovic, G.; Langer, R. *Journal of Cellular Biochemistry*

1993, *51*, 257.

(15) Braunecker, J.; Baba, M.; Milroy, G. E.; Cameron, R. E. *International Journal of Pharmaceutics* **2004**, *282*, 19.

(16) Wu, L. B.; Ding, J. D. *Journal of Biomedical Materials Research Part A* **2005**, *75A*, 767.

(17) Gordon, T. D.; Schloesser, L.; Humphries, D. E.; Spector, M. *Tissue Engineering* **2004**, *10*, 1287.

(18) Sung, H. J.; Meredith, C.; Johnson, C.; Galis, Z. S. *Biomaterials* **2004**, *25*, 5735.

(19) Nishi, T.; Wang, T. T.; Kwei, T. K. *Macromolecules* **1975**, *8*, 227.

(20) Lloyd, D. R.; Kinzer, K. E.; Tseng, H. S. *Journal of Membrane Science* **1990**, *52*, 239.

(21) Nam, Y. S.; Park, T. G. *Journal of Biomedical Materials Research* **1999**, *47*, 8.

(22) Nam, Y. S.; Park, T. G. *Biomaterials* **1999**, *20*, 1783.

(23) Kumacheva, E.; Li, L.; Winnik, M. A.; Shinozaki, D. M.; Cheng, P. C. *Langmuir* **1997**, *13*, 2483.

(24) Hopkinson, I.; Myatt, M. *Macromolecules* **2002**, *35*, 5153.

(25) Kim, J. K.; Taki, K.; Ohshima, M. *Langmuir* **2007**, *23*, 12397.

(26) Loeb, S.; Sourirajan, S. *Advances in Chemistry Series* **1962**, *38*, 117.

(27) Wang, H. Y.; Kobayashi, T.; Fujii, N. *Langmuir* **1996**, *12*, 4850.

(28) Wang, H. Y.; Kobayashi, T.; Fukaya, T.; Fujii, N. *Langmuir* **1997**, *13*, 5396.

(29) Ying, L.; Kang, E. T.; Neoh, K. G. *Langmuir* **2002**, *18*, 6416.

(30) Kawakami, M.; Egashira, M.; Kagawa, S. *Bulletin of the Chemical Society of Japan* **1976**, *49*, 3449.

(31) Liu, B.; Du, Q. G.; Yang, Y. L. *Journal of Membrane Science* **2000**, *180*, 81.

(32) Lin, W. J.; Lu, C. H. *Journal of Membrane Science* **2002**, *198*, 109.

(33) Chakrabarty, B.; Ghoshal, A. K.; Purkait, M. K. *Journal of Membrane Science* **2008**, *309*, 209.

(34) Mukai, S. R.; Nishihara, H.; Tamon, H. *Chemical Communications* **2004**, 874.

(35) Kimizuka, N.; Viriyarattanasak, C.; Suzuki, T. *Cryobiology* **2008**, *56*, 80.

(36) Tsai, F. J.; Torkelson, J. M. *Macromolecules* **1990**, *23*, 775.

(37) Mullins, W. W.; Sekerka, R. F. *Journal of Applied Physics* **1964**, *35*, 444.

(38) Ragnarsson, R.; UTTER, B.; BODENSCHATZ, E. In *Proceedings of the Materials Research Society Symposium* 1997; Vol. 481, p 65.

(39) Matsuyama, H.; Okafuji, H.; Maki, T.; Teramoto, M.; Tsujioka, N. *Journal of Applied Polymer Science* **2002**, *84*, 1701.

Chapter IV

Honeycomb Monolith-Structured Silica with Highly Ordered, Three-Dimensionally Interconnected Macroporous Walls

4.1. Introduction

In chapter II and III, the preparation method of PLLA honeycomb monolith structures was discussed. In this chapter, unidirectional freezing technique was extended to colloidal suspension system. As shown in previous chapters, unidirectional freezing is a relatively simple and cost-effective method for the creation of microhoneycomb monolith structures. It has been used to prepare various kinds of materials, such as ceramics,[1] polymers,[2] carbon,[3] etc. The unidirectional freezing method has been applied to several systems, including sol-gel[4] and polymer-solvent systems.[2] However, there have been no applications of this method to prepare highly ordered and three-dimensionally interconnected structure by adopting particle templating technique.

Velev et al.[5] were the first to report a unique method for preparation of highly ordered, three-dimensionally interconnected silica structures using a colloid crystal as a template. Since then, materials with ordered structures have been investigated intensively by many researchers over the last decade.[5-14] The unique structure reported by Velev's group was determined by Zakhidov et al. to be an inverse opal.[6] The resulting 3D structures have great potential as photonic crystals, catalysts, electrodes, and bio materials.[15,16] Several methods, such as filtration,[5,7,8] centrifugation,[17] and

drying[9] have been proposed for fabricating the regularly aligned colloid crystals. Infiltration of an inorganic precursor into a prearranged template has often been used to prepare the inverse opal structure.[5-8] Recently, a new method was developed, involving direct introduction of colloid particles into precursor solutions.[12,13] Iskandar et al.[12] prepared a reverse opal structure from silica by dip coating a colloidal suspension of SiO_2 and polystyrene latex (PSL) mixture without preordered arrangement of PSL. Oh et al.[13] conducted a sol-gel synthesis of the mesoporous silicate in the presence of the polymer latex. However, these methods do not provide materials of large size and uniform structure. More development is necessary to discover a simple method for preparation of relatively large structures for commercial applications, such as catalysts and adsorbents.

In this chapter, the unidirectional freezing of a colloidal suspension composed of two kinds of monodispersed nanoparticles was tried to produce a honeycomb monolith structure with highly ordered, three-dimensionally interconnected macroporous walls.

4.2. Experimental

4.2.1. Materials

Silica sol and monodispersed poly[styrene-(co-2-hydroxyethyl methacrylate)] (PSHEMA) latex were used for this study. Silica sol (Snowtex OS) was kindly supplied by Nissan Chemical Industries Co., LTD. The diameter of the silica nanoparticles was in the range of 8-11 nm.

4.2.2. Preparation of PSHEMA Particles

Monodispersed PSHEMA latex used in this study was prepared by modifying the procedure reported by Reese and Asher.[18] The latex was prepared by batch emulsion copolymerization of styrene and 2-hydroxyethyl methacrylate using potassium persulfate as initiator. Sodium dodecyl sulfate was added as a surfactant, to decrease the diameter of PSHEMA submicroparticles. The amounts of reagent used in this study were as follows: 70 g styrene, 2 g 2-hydroxyethyl methacrylate, 210 mL of distilled water, 20 mg of Sodium dodecyl sulfate, and 0.11 g potassium persulfate. Emulsion polymerization was conducted with three different contents of sodium dodecyl sulfate of 0, 10, and 20 mg. The monodispersed PSHEMA particles were collected by centrifugation, washed several times with water by repeating centrifugation and dispersion, and dried in vacuo for 2 days. As shown in Figure 4.1, spherical PSHEMA particles with uniform diameter were obtained. The average particle diameters and the CV values were calculated by image analysis of the SEM micrographs. The average particle diameter and the CV value of PSHMA decreased with an increase of the content of sodium dodecyl sulfate. We summarized the average diameters and the CV values in Table 4.1. PSHEMA particles with an average diameter of 385 nm and the a CV value of 2.86% were used for this study.

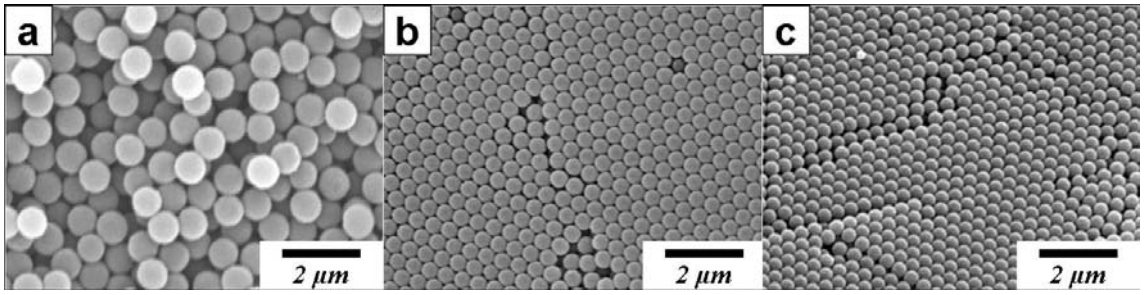

Figure 4.1. SEM images of PSHEMA submicroparticles prepared with sodium dodecyl sulfate content of (a) 0 mg, (b) 10 mg, and (c) 20 mg.

Table 4.1. the average diameters and the CV values of PSHEMA particles.

Addition amount of sodium dodecyl sulfate (mg)	Average diameter (nm)	CV value (%)
0 (0.0 ppm)	855	10.20
10 (35.4 ppm)	460	3.18
20 (70.9 ppm)	385	2.86

4.2.3. Preparation of Porous Silica Structure

The dried PSHEMA particles were added to the silica sol with a 74.2/25.8 PSHEMA/silica volume ratio. The PSHEMA particles were dispersed by stirring and ultrasonic treatment. Several compositions were prepared with three different levels of total particle concentrations of 10, 20, and 30 vol % to investigate the effect on the structure. After dispersion treatment, the colloidal solution was poured into a polypropylene (PP) test tube, 100 mm in length and 10 mm in diameter. The test tube was then frozen unidirectionally by immersion into a liquid nitrogen bath at a constant rate（2.0-17.5 cm hr^{-1}). After freezing the solution completely, the solidified sample was freeze-dried at 268 K for 4 days. The freeze-dried sample was then calcined at 723 K to

remove PSHEMA particles.

4.2.4. Morphology Characterization

The morphologies of the resulting porous samples were observed by scanning electron microscopy (SEM; Tiny-SEM 1540, Technex Lab Co. Ltd.). The samples were cut with a razor blade parallel and perpendicular to the direction of freezing. They were then coated with gold-palladium in vacuo for scanning electron microscopy (SEM) observation. In the unidirectional freezing process, the freezing rate changes until a pseudo-steady state is established in the unidirectional freezing process. Tamon and co-researchers[4,19] suggested that the pseudo-steady state of the ice growth is established at least 5 cm above the bottom of the tubes. Because of this, we harvested a sample from 5 cm above the bottom of the tube for SEM observation.

4.3. Result and Discussion

4.3.1. Resulting Porous Honeycomb Monolith Structure

Figure 4.2a shows a photographic image of calcined honeycomb monolith-structured silica, several centimeter in length and about 8 mm in diameter. The test results for laser transmission perpendicular and vertical to the freezing direction were illustrated in Figure 4.2b and Figure 4.2c, respectively. The light could transmit through the sample structure. When the laser was perpendicular to the freezing direction, the strength of the transmitted light was strongest in the center area and some light transmitted thorough the sidewall because the porous structure had highly ordered, three-dimensionally interconnected macroporous walls. The strength of the light

transmitted vertical to the freezing direction was weaker than the strength of the light transmitted through perpendicular to freezing direction. This indicated that the material has unidirectionally aligned continuous pores, micro-scale channels, in the freezing direction.

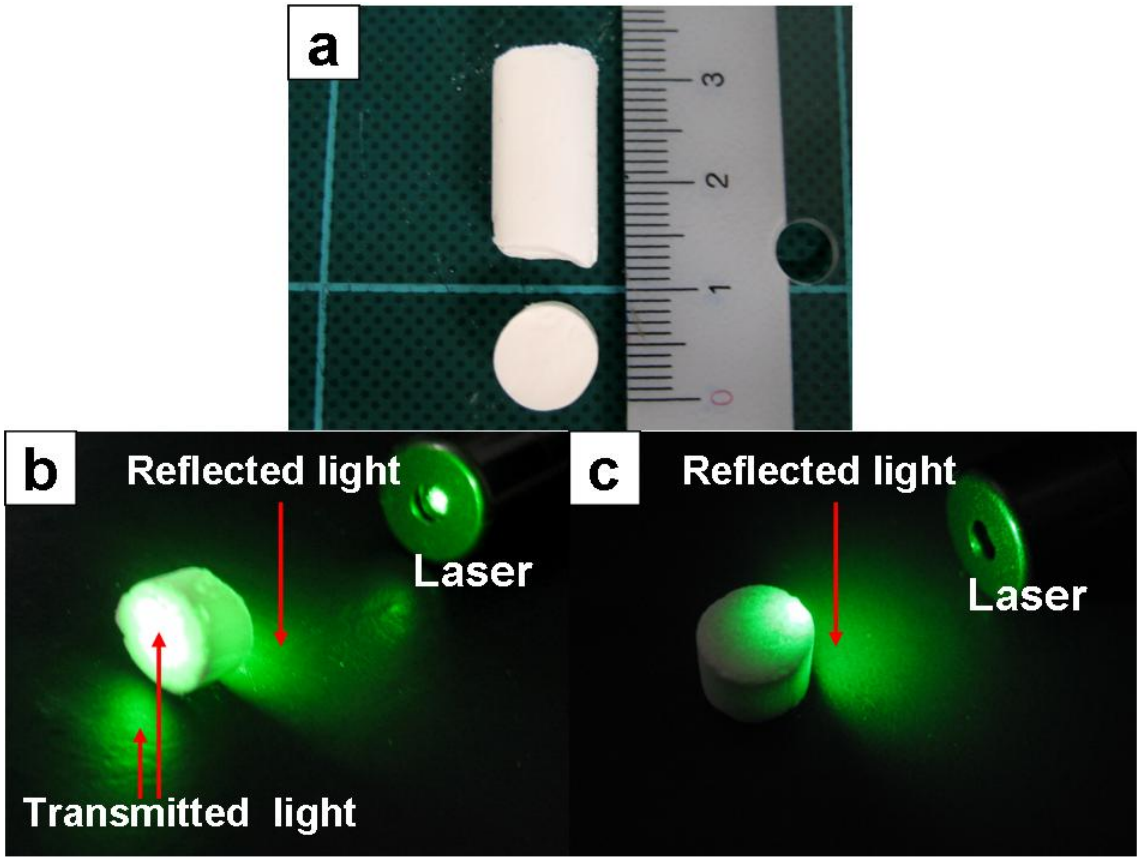

Figure 4.2. Photographs of Honeycomb monolith-structured silica. (a) overall image of the calcined sample, and (b) the result of laser irradiation through perpendicular to the freezing direction, and (c) the result of laser irradiation through vertical to freezing direction.

Figure 4.3 shows typical SEM micrographs of prepared silica micro-scale, honeycomb structures. The SEM sample was prepared from PSHEMA/silica sol with a 20 vol%

total particle concentration, a 74.2/25.8 PSHEMA/silica volume ratio, and a 3.5 cm hr^{-1} immersion rate. Figures 4.3a and b show SEM micrographs of cross-sectional areas of the sample, cut in parallel and perpendicular to the freezing direction, respectively. Both images clearly show a honeycomb monolith structure in the cross-section, with smooth-walled micro-scale channels aligned along the freezing direction. The magnified SEM micrograph of the cross-sectional area parallel to freezing direction is shown in Figures 4.3c. Macropores can be observed on the walls of the silica honeycomb monolith structure. The pores originated from PSHEMA and were well aligned in three-dimensions. This result indicates the spontaneous alignment and packing of two particles with different sizes, occurring during the unidirectional freezing process. Figure 4.3d clearly shows that the walls have highly ordered and three-dimensionally interconnected macropores. The macropore size was determined by the size of the PSHEMA particles. The size of the macropore is about 300 nm, which is smaller than the particle size due to shrinkage during calcination.

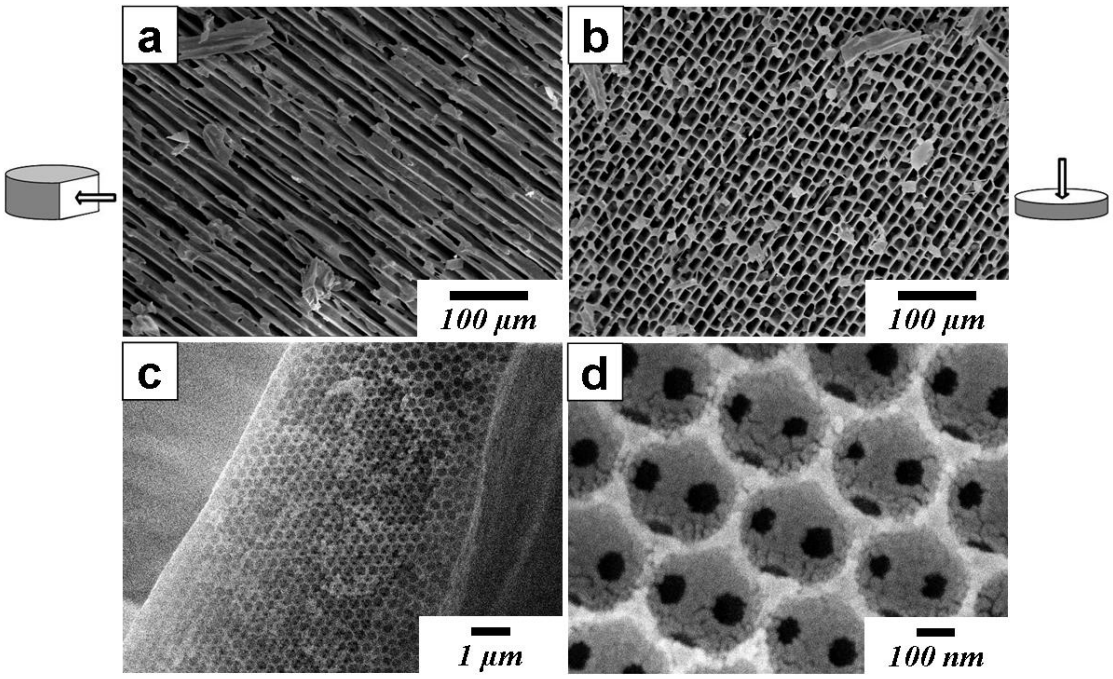

Figure 4.3. Micrographs of honeycomb monolith structures prepared from PSHEMA/silica sol with a 20 vol% total particle concentration, a 74.2/25.8 PSHEMA/silica volume ratio and a 3.5 cm h^{-1} immersion rate. (a) cross-sectional area parallel to the freezing direction, (b) cross-sectional area perpendicular to the freezing direction, (c) magnified cross-sectional area parallel to freezing direction, and (d) magnified micrograph that shows interconnected macropores prepared by calcination.

The nitrogen adsorption-desorption isotherms were measured at 77 K to confirm the existence of mesopores and the result was shown in Figure 4.4. The inset shows that the pore size distribution calculated from the adsorption branches. The isotherms were measured with the sample prepared with a 20 vol% total particle concentration, a 74.2/25.8 PSHEMA/silica volume ratio, and a 3.5 cm hr^{-1} immersion rate. The BET surface area was 281 m^2 g^{-1}. The pore size distribution was determined using the BJH method.[20] As shown in the inset of Figure 4.4, there was a peak at ca. 2.6 nm of pore

diameter. The mesopore volume of the sample was small because the sample has highly macroporous morphology and mesopore structure was formed with only several layers of silica particles. The isotherm was compared with a nonporous silica standard [21] (LiChrosphere Si-1000) in reduced units (divided by the adsorbed volume at a reduced pressure P/P_0 equal to 0.4), which was previously reported by Cabanas et al. to determine the existence of micropores.[22] As shown in Figure 4.5, comparison of adsorption data of Honeycomb monolith-structured silica showed almost complete overlapping with the standard in the low-pressure range before nitrogen condensation, which indicates the absence of microporosity in the sample.

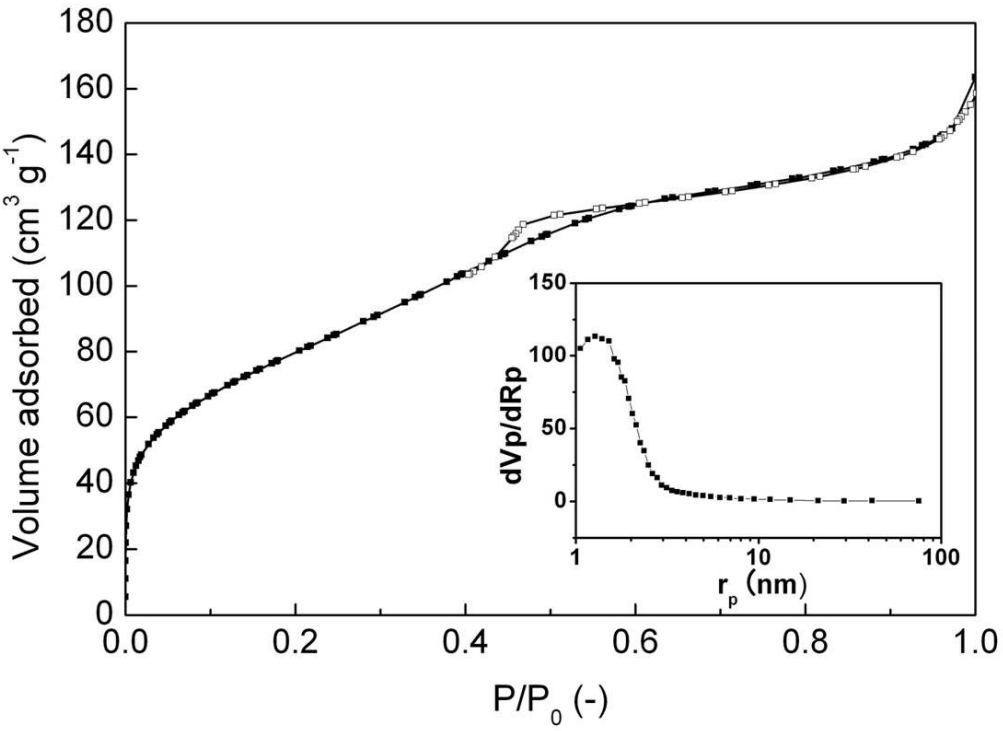

Figure 4.4. Nitrogen adsorption-desorption isotherms. The inset shows the pore size distribution from the desorption branches. (■) adsorption and (□) desorption.

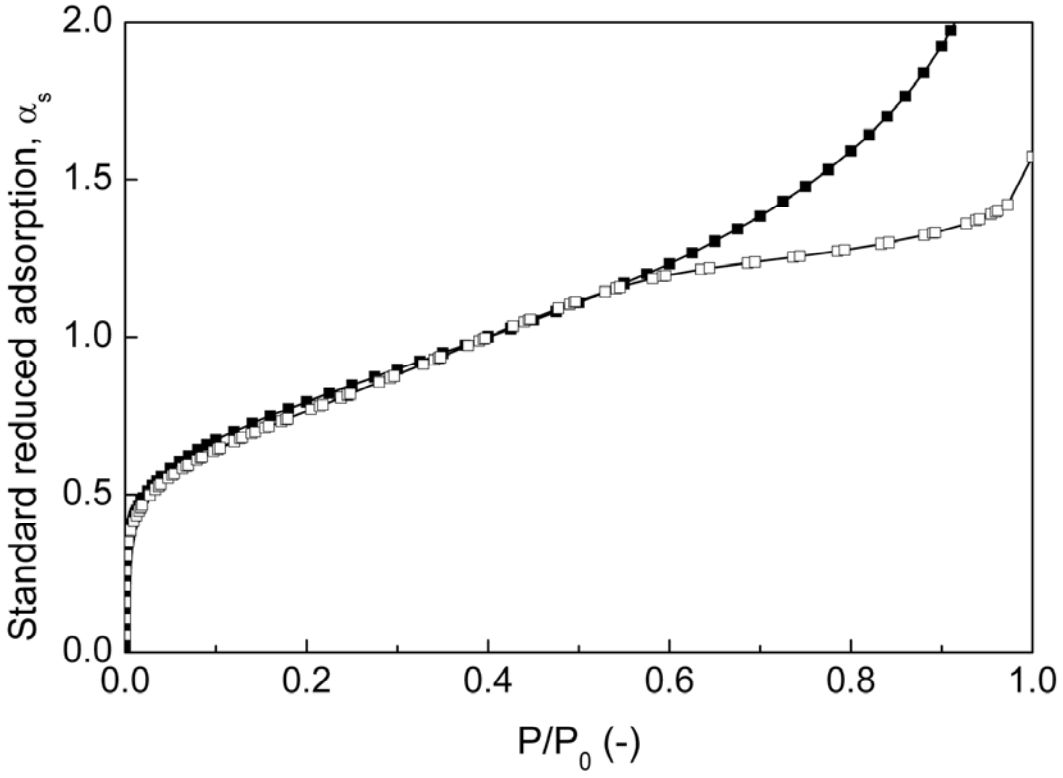

Figure 4.5. Comparison of the standard reduced nitrogen adsorption data for macroporous silica LiChrospher Si-1000 with data of honeycomb monolith-structured silica. (■) LiChrospher Si-1000 and (□) honeycomb monolith-structured silica.

4.3.2. Effect of Freezing Rate and Total Particle Concentration

The schematic diagram of the fabricated structure is illustrated in Figure 4.6. The structure has three different kinds of pores; micro-scale channels prepared by templating ice crystals, highly ordered and three-dimensionally interconnected macropores prepared by templating PSHEMA particles, and mesopores between silica particles. The average diameter and the wall thicknesses of micro-scale channels can be controlled by the immersion rate (freezing rate) and total particle concentration. The test results are shown in Figures 4.7 and 4.8. The effects of the freezing rate and the total particle

concentration on the micro-scale channel diameter and the wall thickness were investigated using SEM micrographs. The average micro-scale channel diameter decreased with the increase in the freezing rate and total particle concentration. The average wall thickness decreased with the increase in freezing rate and a decrease in total particle concentration (Figure 4.9-10).

As shown in Figure 4.11, macroporosity was measured using mercury porosimetry (Pore Master-60, Quantachrome .Instruments). The result clearly showed a bimodal pore size distribution. The sample which was prepared with a 20 vol% total particle concentration and 3.5 cm hr^{-1} immersion rate showed a clear peak at 8.63 μm. The peak corresponds to the micro-scale channels. As previously shown in Figure 4.9, the average diameter of micro-scale channels was calculated from SEM images and the result was 9.61 μm. The change in the average channel diameter coincided with the result of SEM image analysis. The average channel diameter decreased with the increase in the freezing rate and the pore volume of micro-scale channels decreased with the increase in the total particle concentration. Even though all samples have macropores in 300 nm diameter, the result of mercury porosimetry clearly showed clear a peak at ca. 70 nm. This peak could be corresponding to the small holes interconnecting macropores. As shown in Figure 4.3d, the average size of small holes was ca. 70 nm. Considering the principle of mercury porosimetry measurement, this may be proper result for the inverse opal structure.

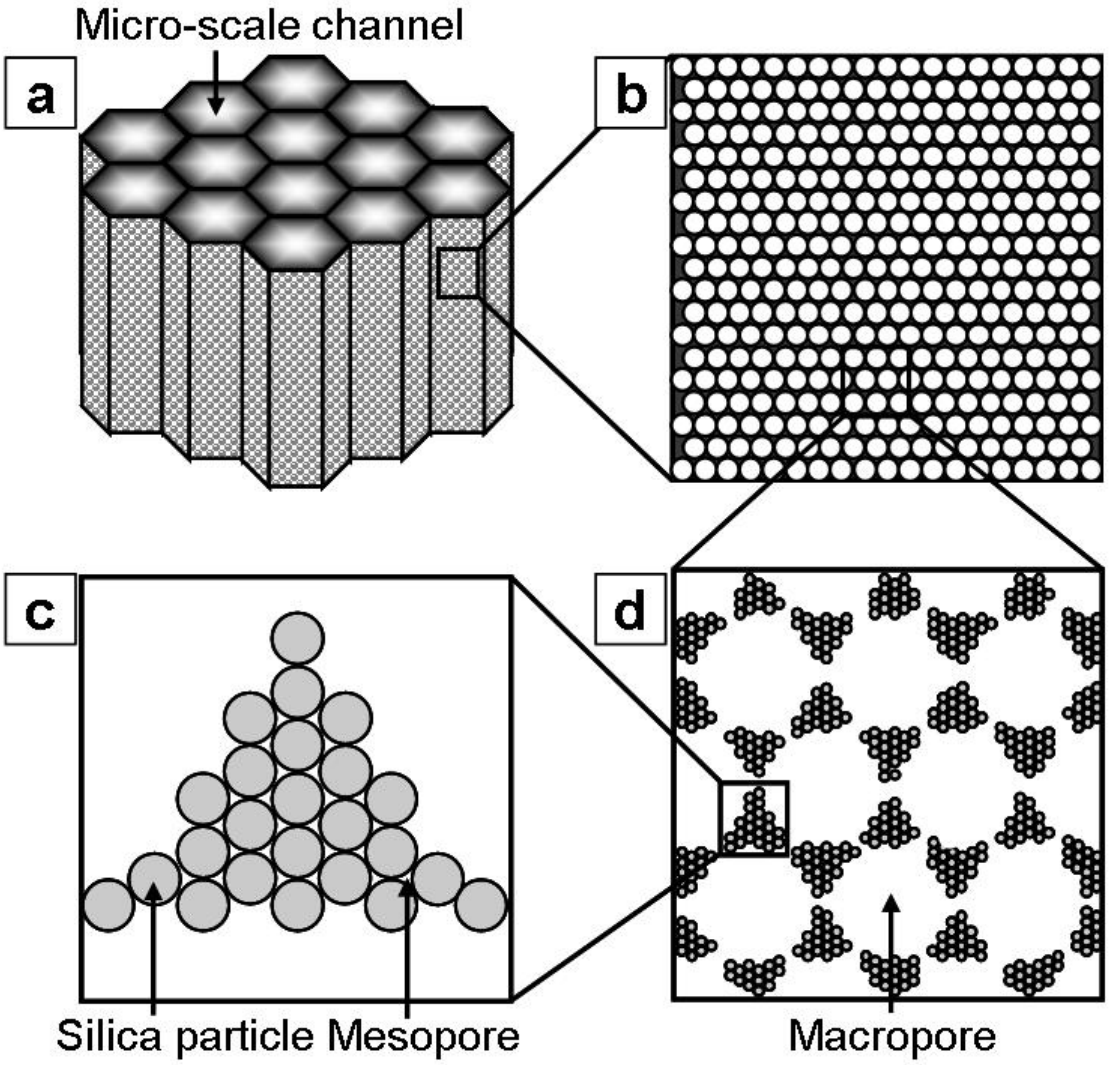

Figure 4.6. Schematic diagram of the fabricated structure. (a) Honeycomb monolith structure, (b) highly ordered macropores, (c) magnified macropores interconnected three-dimensionally to each other, and (d) packed silica particles.

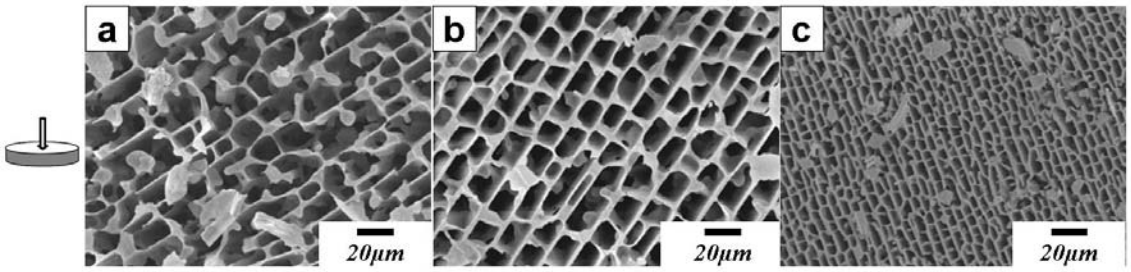

Figure 4.7. SEM images of cross-sectional area perpendicular to the freezing direction of honeycomb monolith structures prepared from PSHEMA/silica sol with a 20 vol% total particle concentration, a 74.2/25.8 PSHEMA/silica volume ratio and an immersion rate of (a) 2.0 cm hr^{-1}, (b) 3.5 cm hr^{-1}, and (c) 17.5 cm hr^{-1}.

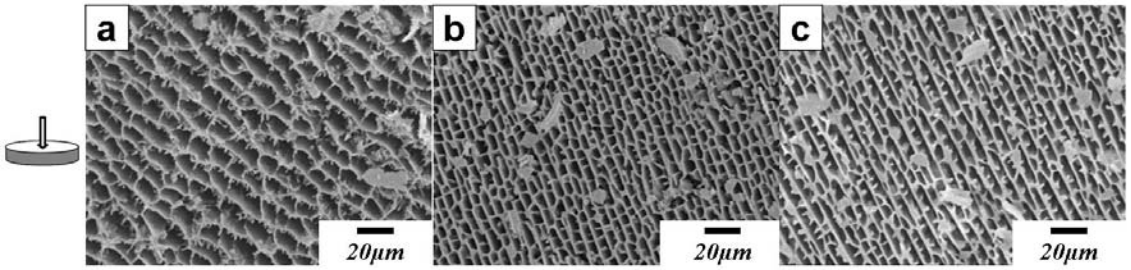

Figure 4.8. SEM images of cross-sectional area perpendicular to the freezing direction of honeycomb monolith structures prepared from PSHEMA/silica sol with a 74.2/25.8 PSHEMA/silica volume ratio, a 17.5 cm hr^{-1} immersion rate, and a total particle concentration of (a) 10 vol%, (b) 20 vol%, and (c) 30 vol%.

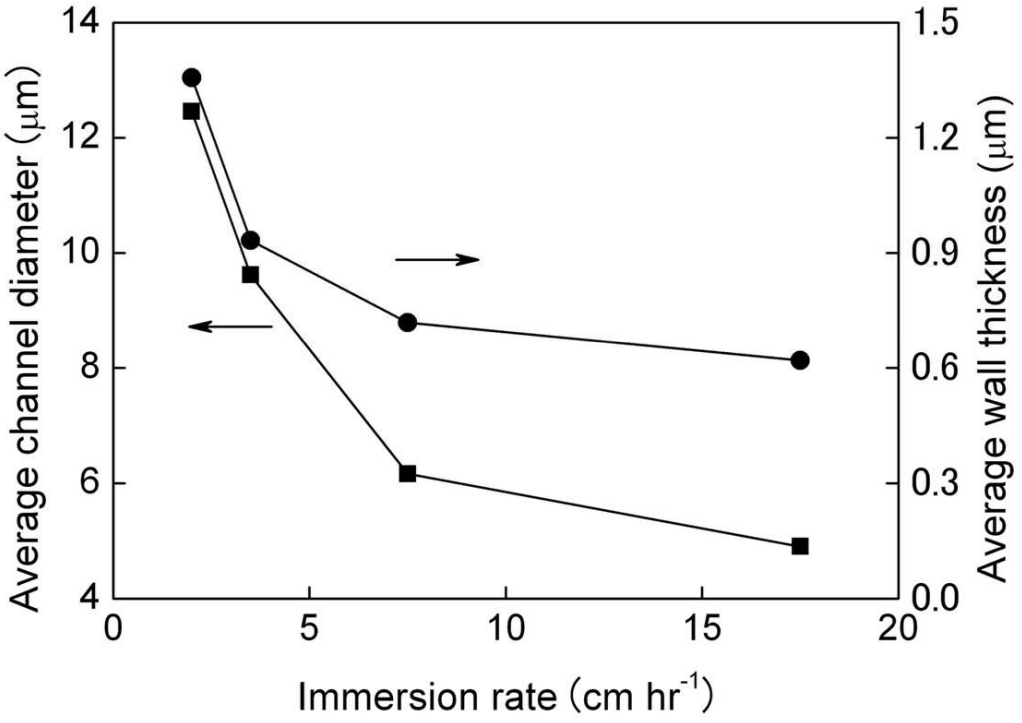

Figure 4.9. Effect of the immersion rate on the average channel diameter and the average wall thickness at a 20 vol% total particle concentration. (■) average channel diameter and (●) average wall thickness.

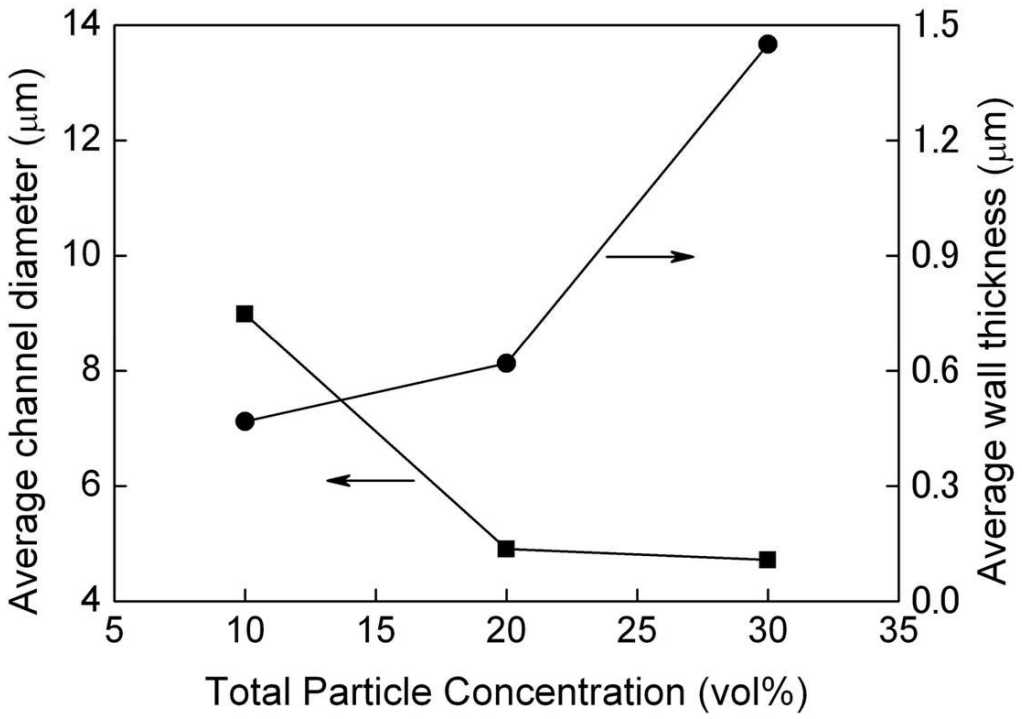

Figure 4.10. Effect of the total particle concentration on the average channel diameter and the average wall thickness at a 17.5 cm hr^{-1} immersion rate. (■) average channel diameter and (●) average wall thickness.

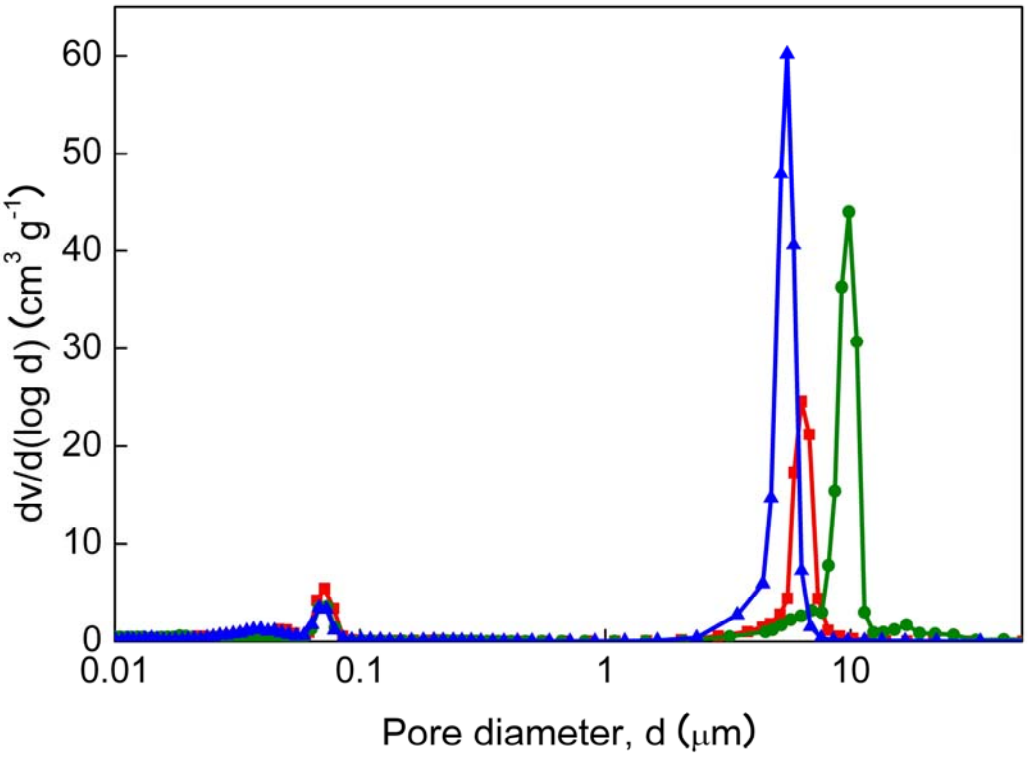

Figure 4.11. The result of mercury porosimetry measurement. Samples were prepared with (●) a 20 vol% total particle concentration and a 3.5 cm hr^{-1} immersion rate, (▲) 20 vol% total particle concentration and 7.5 cm hr^{-1} immersion rate, and (■) 30 vol% total particle concentration and 3.5 cm hr^{-1} immersion rate.

4.3.3. Formation Mechanism of Honeycomb Structure and Particle Packing

In the previous chapters, a honeycomb monolith structure was created from poly (L-lactic acid) (PLLA) and a dehydrated 1,4-dioxane solution, where the 1,4-dioxane crystalline structure was used as a template. The solvent was crystallized and the crystals grow in the freezing direction under the constitutional supercooling condition. Thus, the crystal growth followed the Mullins-Sekerka instability theory.[23] Impurities in the solution increase instability and enhance transition from a cellular to a dendritic structure in solvent crystals. However, in the colloidal solution used in the present work, the existence of particles in the freezing solution did not seem to change the degree of constitutional supercooling and instability. Therefore, the creation of smooth-walled (cellular type) micro-scale channels was not hindered by the particles. The speculated mechanism of particle packing and self-organization in the ice template is illustrated in Figure 4.12. In the course of unidirectional crystal growth of water, the particles were expelled from the growing ice crystals.[2,24] The concentration of water in the colloidal liquid phase surrounded by the ice was gradually decreased according to the growth of the ice. On the other hand, the particle density in the colloidal liquid phase increased while maintaining dispersion, and finally the particles were closely packed. The growth rate of the ice crystals could be considered to affect the repulsion of particles and the ordered arrangement of PSHEMA/silica particles.

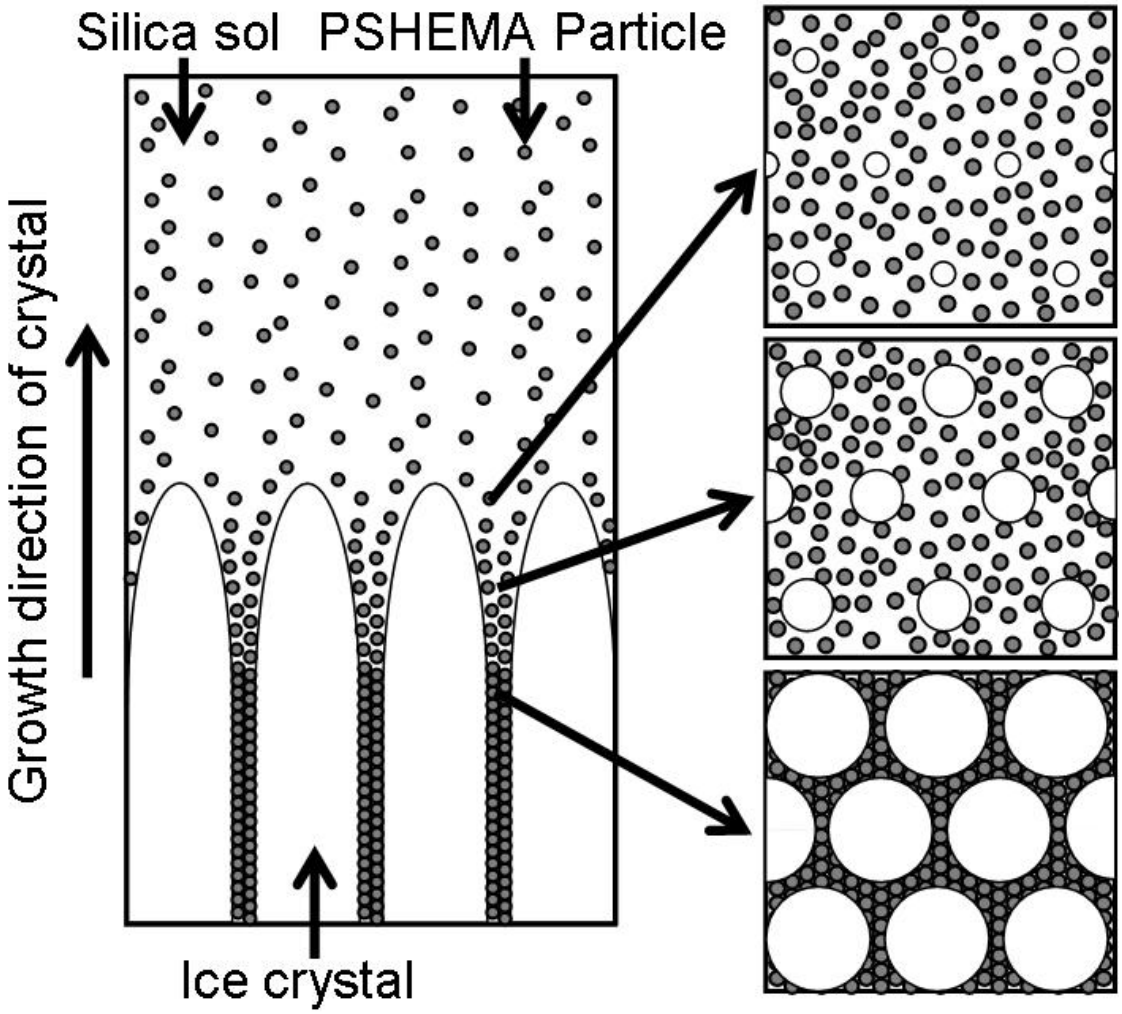

Figure 4.12. Schematic diagram explaining particle packing by unidirectional growth of ice crystals

4.4. Conclusion

In conclusion, the unidirectional freezing scheme is proposed as a simple method for packing colloidal silica and preparing honeycomb monolith-structured silica, with highly ordered, three-dimensionally interconnected macroporous walls. The relatively large size inverse opal structure, which has aligned micro-scale channels, can be easily produced using this method. The experimental results indicate that three-dimensionally interconnected macroporous structures develop by spontaneous self-organization of two kinds of particles in the growing ice template. This new method could be applied to a range of nanoparticle suspensions for particle packing and colloidal crystals preparation. We expect potential applications in a wide range of areas, such as catalysts, adsorbents, tissue scaffolds, ultralightweight materials, and micro fluidics.

4.5. Reference

(1) Fukasawa, T.; Ando, M.; Ohji, T.; Kanzaki, S. *Journal of American Ceramic Society* **2001**, *84*, 230.

(2) Zhang, H. F.; Hussain, I.; Brust, M.; Butler, M. F.; Rannard, S. P.; Cooper, A. I. *Nature Materials* **2005**, *4*, 787.

(3) Mukai, S. R.; Nishihara, H.; Yoshida, T.; Taniguchi, K.; Tamon, H. *Carbon* **2005**, *43*, 1563.

(4) Nishihara, H.; Mukai, S. R.; Yamashita, D.; Tamon, H. *Chemistry of Materials* **2005**, *17*, 683.

(5) Velev, O. D.; Jede, T. A.; Lobo, R. F.; Lenhoff, A. M. *Nature* **1997**, *389*, 447.

(6) Zakhidov, A. A.; Baughman, R. H.; Iqbal, Z.; Cui, C. X.; Khayrullin, I.; Dantas, S. O.; Marti, I.; Ralchenko, V. G. *Science* **1998**, *282*, 897.

(7) Park, S. H.; Xia, Y. N. *Advanced Materials* **1998**, *10*, 1045.

(8) Holland, B. T.; Blanford, C. F.; Stein, A. *Science* **1998**, *281*, 538.

(9) Yang, P. D.; Deng, T.; Zhao, D. Y.; Feng, P. Y.; Pine, D.; Chmelka, B. F.; Whitesides, G. M.; Stucky, G. D. *Science* **1998**, *282*, 2244.

(10) Iskandar, F.; Mikrajuddin; Okuyama, K. *Nano Letters* **2001**, *1*, 231.

(11) Iskandar, F.; Mikrajuddin; Okuyama, K. *Nano Letters* **2002**, *2*, 389.

(12) Iskandar, F.; Abdullah, M.; Yoden, H.; Okuyama, K. *Journal of Applied Physics* **2003**, *93*, 9237.

(13) Oh, C. G.; Baek, Y. Y.; Ihm, S. K. *Advanced Materials* **2005**, *17*, 270.

(14) Woo, S. W.; Dokko, K.; Sasajima, K.; Takei, T.; Kanamura, K. *Chemical Communications* **2006**, 4099.

(15) Stein, A.; Schroden, R. C. *Current Opinion in Solid State & Materials Science*

2001, *5*, 553.

(16) Yuan, Z. Y.; Su, B. L. *Journal of Materials Chemistry* **2006**, *16*, 663.

(17) Wijnhoven, J.; Vos, W. L. *Science* **1998**, *281*, 802.

(18) Reese, C. E.; Asher, S. A. *Journal of Colloid and Interface Science* **2002**, *248*, 41.

(19) Nishihara, H.; Mukai, S. R.; Tamon, H. *Carbon* **2004**, *42*, 899.

(20) Barrett, E. P.; Joyner, L. G.; Halenda, P. P. *Journal of the American Chemical Society* **1951**, *73*, 373.

(21) Jaroniec, M.; Kruk, M.; Olivier, J. P. *Langmuir* **1999**, *15*, 5410.

(22) Cabanas, A.; Enciso, E.; Carbajo, M. C.; Torralvo, M. J.; Pando, C.; Renuncio, J. A. R. *Chemistry of Materials* **2005**, *17*, 6137.

(23) Mullins, W. W.; Sekerka, R. F. *Journal of Applied Physics* **1964**, *35*, 444.

(24) Asthana, R.; Tewari, S. N. *Journal of Materials Science* **1993**, *28*, 5414.

Chapter V

General Discussion: from the Viewpoint of Cell Morphology Control.

5.1. Introduction

In chapter II, III, and IV, the preparation methods of honeycomb monolith structures of PLLA as well as silica were discussed. The morphology was successfully controlled using several methods such as the addition of third components, phase separation of polymer blend and leaching, and PSHEMA particle templating and burning out of it. In chapter V, the control of aligned porous structure will be discussed by paying attention to the underlying principles of the crystal growth during unidirectional freezing. To discuss the control of morphology, several papers that have been reported up to now were reviewed and classified by raw materials; 1) polymer solution, 2) colloidal suspension which is accompanying sol-gel reaction, and 3) ceramic slurry and colloidal suspension which is not accompanying sol-gel reaction.

In order to control the morphology, several parameters affecting the final structure have been reported such as raw material concentration,[1] particle size of ceramic slurry,[2,3] addition of third component,[4] and freezing rate.[5-7] Almost of all papers discussed about controllability of wall thickness and micro-scale channel diameter of honeycomb by changing raw material concentration and freezing rate, but did not discussed controllability of the cell structure. In general, the average micro-scale channel diameter decreased with the increase in freezing rate as well as raw material concentration. The average wall thickness decreased with the increase in freezing rate

and as well as with the decrease in raw material concentration. Recently, Deville et al.[2] summarized the relation between morphology and ice front velocity by observing the change in morphology during the initial period of unidirectional freezing of alumina slurry. Even though several research group reported the preparation of porous structure using unidirectional freezing, the controllability of cell morphology in pseudo-steady state freezing has not yet intensively investigated excluding unidirectional freezing of colloidal suspension accompanying sol-gel reaction.[8] The change in crystal type of the used solvent was pointed out only by Deville et al.[9] Therefore, to investigate the relationship of morphology with solvent and raw material composition, the result reported by several papers were analyzed. On the base of the analysis, the effect of solvent and the raw material composition on the morphology were intensively discussed. The unidirectional growth of solvent crystal was explained in the frame of Mullins-Sekerka instability[10] and Jackson and Hunt theory[11] which were representative theories for the unidirectional growth of binary and eutectic alloy.

5.2. Theories of the Unidirectional Growth of Binary and Eutectic Alloy

A schematic phase diagram of binary alloy was illustrated in Figure 5.1. In general, during solidification of alloy, solute is piled up ahead of the solid-liquid interface due to the smaller solubility of solid when the partition coefficient is less than unit (A region of Figure 5.1). The partition coefficient is the ratio of the equilibrium concentration of solute on the solid side of the interface to that on the liquid side of the interface. Interfacial concentration gradient of solute, which is established by diffusion of solute

expelled from solvent crystals, leads to depression of freezing point. This is one of the main factors that cause instability of solid-liquid interface. Freezing point depression is the phenomenon where the freezing point of a liquid (a solvent) is depressed when a solute is added. In other word, a solution has a lower freezing point than a pure solvent.

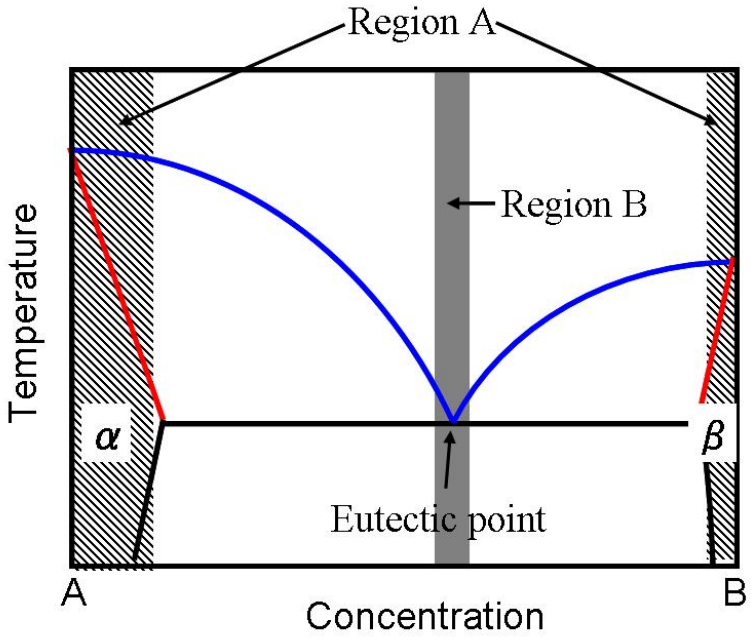

Figure 5.1. A schematic representation of phase diagram of binary alloy.

As shown in Figure 5.2, cells or dendrites crystal is usually formed at the region A where a single phase solid is formed by unidirectional freezing of binary alloy. This structure development in the region A can be explained by the theory of Mullins and Sekerka.[10]

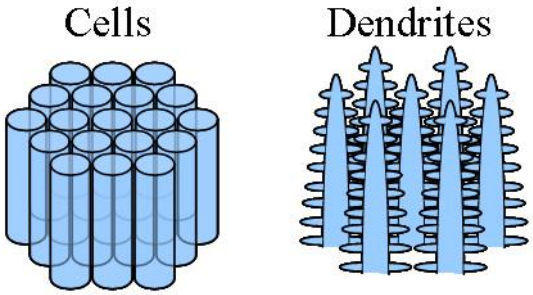

Figure 5.2. Schematic representation of cellular and dendritic structure prepared by unidirectional freezing of binary alloy

However, long-range diffusion and solute pile up do not occur at or near the eutectic composition (in the region B of Figure 5.1.) since the solute is rejected by one phase is used for the growth of the other phase. The unidirectional freezing of eutectic alloy is different from the solidification of single phase in terms of structure. As shown in Figure 5.3, lamellar or rods structure is usually formed by unidirectional freezing of eutectic alloy. Jackson and Hunt[11] analyzed the conditions for the stability of the rod and lamellar structures.

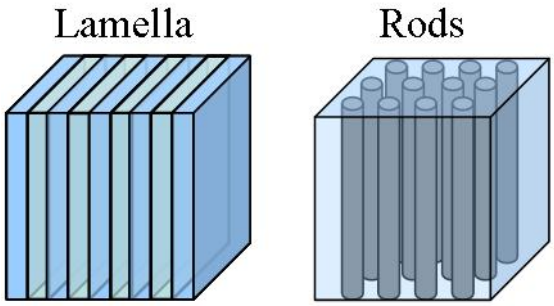

Figure 5.3. Schematic representation of lamellar and rods structure prepared by unidirectional freezing of eutectic alloy

5.2.1. Mullins-Sekerka Instability

Mullins and Sekerka[10] described that the instability of planar interface, which is unidirectionally freezing at constant velocity, is governed by competition between the destabilizing the solute interfacial concentration gradient and the surface energy and the temperature gradient that stabilize the solid-liquid interface. The stability of the planar interface was analyzed by introducing a sinusoidal perturbation to the infinitesimal initial interface and calculating the time dependent behavior of the amplitude. Linear stability analysis yields the following expression for the growth rate of a perturbation (δ) to the planar interface, of magnitude $\dot{\delta}$ as a function of the instability wavelength ($2\pi/\omega$):

$$\frac{\dot{\delta}}{\delta} = \frac{V\omega\left\{-2T_m\Gamma\omega^2\left[\omega^*-(V/D)p\right]-(\wp'+\wp)\left[\omega^*-(V/D)p\right]+2mG_c\left[\omega^*-(V/D)\right]\right\}}{2\omega mG_c+(\wp'-\wp)\left[\omega^*-(V/D)p\right]} \tag{5.1}$$

$$\omega^* = (V/2D)+\left[(V/2D)^2+\omega^2\right]^{\frac{1}{2}}$$

$$\bar{k} = \frac{1}{2}(k_S+k_L)$$

$$\wp = (k_L/\bar{k})G$$

$$\wp' = (k_S/\bar{k})G'$$

$$p = 1-n$$

$\delta(t)$: The amplitude of the sinusoidal ripple

V : The constant mean growth velocity of the interface

ω : The frequency of the sinusoidal ripple

T_M : The melting temperature of a flat interface

$\Gamma = \sigma/L$: The ratio of the surface energy and the latent heat of fusion

D : Diffusion coefficient of solute in the liquid

n : The partition coefficient given by the ratio of the equilibrium concentration of solute on the solid side of the interface to that on the liquid side of the interface

G and G' : The thermal gradients in the liquid and solid at the flat interface

G_C : The concentration gradient in the liquid at the interface

k_S and k_L : The conductivity of solid and liquid

m : The slope of the liquidus line on the phase diagram including sign

As explained by Kurz and Fisher,[12] cellular type crystal grows under conditions close to the limit of constitutional supercooling of the corresponding planar interface. On the other hand, dendrite type crystal grows when the degree of Mullins-Sekerka instability is high. Detail derivation of Mullins-Sekerka instability was described in appendix I.

5.2.2. Jackson and Hunt Theory.

The formation of lamella and rods structure of metal alloy is investigated by Jackson and Hunt.[11] They analyzed the conditions for the stability of rod and lamellar structures. They concluded that stable growth occurs at or near the minimum interface undercooling for a given growth rate. They derived mathematical model for the undercooling of interface of lamellar and rod-type eutectic. The following expression was proposed for the undercooling of lamellar and rod-type eutectic as a function of lamellar spacing, λ, or rod spacing, R, and growth rate, v:

For the undercooling of lamellar interface

$$\frac{\Delta T}{m} = V\lambda Q^L + \frac{a^L}{\lambda} \tag{5.2}$$

$$\frac{1}{m} = \frac{1}{m_\alpha} + \frac{1}{m_\beta}$$

$$Q^L = \frac{P\left(1+\zeta\right)^2 C_0}{\zeta D}$$

$$P = \sum_{n=1}^{\infty}\left(\frac{1}{n\pi}\right)^3 \sin^2\left(\frac{n\pi S_\alpha}{S_\alpha + S_\beta}\right)$$

$$a^L = 2\left(1+\zeta\right)\left(\frac{a_\alpha^L}{m_\alpha} + \frac{a_\beta^L}{m_\beta}\right)$$

$$\zeta = S_\alpha / S_\beta$$

$$C_0 = C_0^\alpha + C_0^\beta$$

m_α and m_β: The slopes of the α and β liquidus lines, respectively.

V : The constant mean growth velocity of the interface

$\lambda = 2\left(S_\alpha + S_\beta\right)$: Lamellar spacing

S_α and S_β: The half of the widths of α and β phase, respectively

T_E: The eutectic temperature

a_α^L and a_β^L: The constants of the α and β phase given by the Gibbs-Thompson relationship

C_0^α and C_0^β: The amounts of B and A, respectively, rejected when unit volume of the α and ß phase freeze

For the undercooling of rod interface

$$\frac{\Delta T}{m} = VRQ^R + \frac{a^R}{R} \tag{5.3}$$

$$Q^R = \frac{4(1+\zeta)}{D\zeta} C_0 M$$

$$\zeta = r_\alpha / r_\beta$$

$$M = \sum_{n=1}^{\infty} \frac{1}{\gamma_n^3} \frac{J_1^2\left(\frac{r_\alpha \gamma_n}{r_\alpha + r_\beta}\right)}{J_0^2(\gamma_n)}$$

$$a^R = 2\sqrt{1+\zeta}\left(\frac{a_\alpha^R}{m_\alpha} + \frac{a_\beta^R}{\zeta m_\beta}\right)$$

$r = 2(r_\alpha + r_\beta)$: Rod spacing

r_α and r_β The radius of α and β phase, respectively

Jackson and Hunt derived the condition for rod formation at a given growth velocity by comparing Eq. 5.2 with Eq. 5.3. They concluded that the growth of rod-type eutectic occurs when the volume difference of two phases is very big. Detail derivation of Jackson and Hunt theory was described in appendix II.

5.3. Unidirectional Freezing of Polymer Solution

Preparation of porous polymeric material using unidirectional freezing has been mainly investigated for bio-scaffold usage in cell cultivation[13] or drug delivery[1] using natural, biodegradable, or biocompatible polymers. The controllability of channel diameter and inherently aligned micro-scale channel are the reason why unidirectional freezing is adopted to this area. Papers related with unidirectional freezing of polymer solution were reviewed and summarized in Table 5.1. As shown in Table 5.1, unidirectional freezing of polymeric solution caused cellular honeycomb or dendritic honeycomb. When water was used as sacrificial template, cellular honeycomb or

dendritic honeycomb was prepared. However, only dendritic honeycomb was prepared with organic solvents excluding benzene[13] and dehydrated 1,4-dioxane cases of chapter II and III. Ma and Zhang[13] prepared cellular honeycomb using poly(L-lactic acid)/benzene solution and dendritic honeycomb using poly(L-lactic acid)/1,4-dioxane solution. They claimed that the morphology could be changed by the used solvent. However, cellular honeycomb was also successfully prepared with poly(L-lactic acid)/dehydrated 1,4-dioxane solution as described in chapter II and III of this dissertation. It was also confirmed experimentally that honeycomb morphology could be transited from cellular structure to dendritic one by the increase of water content. The cellular to dendritic transition of honeycomb structure can be explained by the theory of Mullins-Sekerka instability. As described in Section 5.2.1, crystal type is determined by the degree of Mullins-Sekerka instability. As explained in appendix I, the degree of Mullins-Sekerka instability increases with the increase of solute concentration, slope of liquidus line of phase diagram, and diffusivity of solute in the solution. On the opposite, degree of Mullins-Sekerka instability decreases with the increase of interfacial energy, temperature gradient.

Interfacial concentration gradient of solute, which is established by diffusion of solute expelled from solvent crystals, leads to freezing point depression. Freezing point depression is a colligative property, which means that it is dependent on the dissolved particles and their number, but not their identity. The degree of freezing point depression is proportional to the molar mass of the solution as given by the following equation.

$$\Delta T_f = K_f \times m_B \tag{5.4}$$

ΔT_f: The difference between the freezing point of the pure solvent and the solution.

K_f: The cryoscopic constant, which is dependent on the properties of the solvent.

m_B : Molar mass of solute.

This means that the degree of supercooling can be altered by the used solvent even though the same amount of impurity is dissolved. Therefore, crystal type may be changed with different kind of solvent at the same level of impurity content. The cryoscopic constant was summarized in Table 5.2 for the solvents, which were usually used for unidirectional freezing. As shown in Table 5.2, the cryoscopic constant of water is much smaller than that of 1,4-dioxane. This means that the degree of Mullins-Sekerka instability induced in water is much smaller than that of 1,4-dioxane at the same molar mass of solute and condition.

Table 5.1 Summary of materials, used solvents, and morphology (polymer solutions).

Materials	Solvent	Morphology	Reference
30 mg/ml Agarose aqueous solution	Water	Cellular honeycomb	14
1:1 v/v mixture of 5 wt% PVA aqueous solution and 30 wt% 15 nm silica colloidal suspension	Water	Cellular honeycomb	6
5-15 % (w/v) gelatin aqueous solution	Water	Cellular or dendritic honeycomb	15
2.5-10 wt% PVA	Water	Dendritic honeycomb	1
5 wt% PVA	Water	Dendritic honeycomb	6
2.5-10 wt% PLLA or poly(D,L-lactic acid-co-glycolic acid)	Benzene or 1,4-dioxane	Cellular honeycomb (benzene), Dendritic honeycomb(1,4-dioxane)	13
3-10 wt% PLLA	Dehydrated 1,4-dioxane	Cellular or dendritic honeycomb	Chapter II
7 wt% PLLA/PEG blend	Dehydrated 1,4-dioxane	Cellular or dendritic honeycomb	Chapter III
2.5-5.0 wt% PLLA or PLGA/HAP(PLLA or PLGA/HAP: 30-100/0-70 weight ratio)	1,4-dioxane	Dendritic honeycomb	7
12 wt % 1,2,3,4,6-pentaacetyl β-D-galactose (BGAL)	Liquid CO_2	Dendritic honeycomb	16

Table 5.2 Cryoscopic constants of solvents usually used for unidirectional freezing[17]

Solvent	Cryoscopic constant (K kg/mol)
Water	-1.86
1,4-Dioxane	-4.63
Tert-butyl alcohol	-8.37
Benzene	-5.12
Diethyl ether	-1.79
Camphene	-37.6

5.4. Unidirectional Freezing of Colloidal Suspensions Accompanying Sol-Gel Reaction

Several research groups have reported preparation of porous structure using water base sol and gel. Morphology of unidirectionally frozen structure, which was prepared with colloidal suspension system accompanying sol-gel reaction, was summarized in Table 5.3. Since Mahler and Bechtold[18] reported the preparation of lamellar and polygonal fiber using unidirectional freezing of silica sol or gel, various structure of silica, titania, silica/alumina composites were prepared by the unidirectional freezing method. The method of controlling morphology was well explained by Tamon and coworkers using mobility of silica.[8] They reported the preparation of lamella, flat fibers, and cellular honeycomb by controlling the relaxation time of the hydrosol at the time of freezing and the gelation time of the hydrosol. Cellular honeycomb, polygonal fibers, and powder were also prepared by controlling elapsed time between gelation and freezing, and the gelation time of the hydrogel. Recently, honeycomb of mullite ($3Al_2O_3/2SiO_2$) ceramics which had dendritic feature was also reported by Ding et al.[19] They added poly(vinyl alcohol) (PVA) as binder and acetic acid as stabilizer to form a stable alumina sol. The formation of dendritic honeycomb can be explained by the

Mullins-Sekerka instability. Acetic acid piles up on the solid-liquid interface and causes freezing point depression. The addition of PVA leads to the increase of viscosity, which disturbs the diffusion of acetic acid to liquid side. Nishihara[20] also pointed out that dendrite type ice crystals were grown with titania gel which includes impurity. To prepare polygonal titania fibers, he removed impurities, ethanol and isopropanol, by dialysis. Mahler and Bechtold[18] also reported that fiber formation was precluded by the presence of more than 0.025 M salts.

Table 5.3. Summary of materials, used solvents, and morphology (colloidal suspensions accompanying sol-gel reaction)

Materials	Solvent	Morphology	Reference
0.5-5 mol/l silica gel with less than 0.025 mol/l salt	Water	Lamellar or polygonal fiber	18
Zirconia gel	Water	Polygonal fiber	21
Titania gel	Water	Polygonal fiber	22
Alumina gel	Water	Polygonal fiber	23
0.5–2 mol/l silica sol or gel	Water	Lamella, flat fiber, cellular honeycomb, or polygonal fibers	24
1.6 or 1.9 mol/l silica gel	Water	Cellular honeycomb	25
TiO_2 hydrogel	Water	Polygonal fibers	26
Resorcinol–formaldehyde (RF) hydrogel	Water	Cellular honeycomb	27
Resorcinol–formaldehyde (RF) hydrogel	Water	Cellular honeycomb, polygonal fibers, or self standing bundle	28
1.0-9 mol/l silica gel	Water	Cellular honeycomb	5
Silica sol	Water	Lamella, flat fibers, cellular honeycomb, or polygonal fibers	29
SiO_2/Al_2O_3 gel (Si/Al ratio = 1.9-9.5)	Water	Cellular honeycomb or polygonal fibers	30
0.5-2.0 mol/l silica sol or gel	Water	Lamella, flat fiber, cellular honeycomb, polygonal fibers or powder	8
10 wt% SiO_2/Al_2O_3 (2:3 30 nm SiO_2 powder/Al_2O_3 sol) with PVA (PVA/Al2O_3 1:10 weight ratio)	Water	Dendritic honeycomb	19

5.5. Unidirectional Freezing of Ceramic Slurries or Colloidal Suspensions not Accompanying Sol-Gel Reaction

Recently, unidirectional freezing of ceramic slurry or colloidal suspension, which is not accompanying sol-gel reaction, has been also investigated to prepare porous ceramic materials. Papers related with unidirectional freezing of this system were summarized in Table 5.4. So far, water and camphene were mainly used as solvent due to the environmental friendliness of water, and high freezing point of (±)-camphene (44°C–48°C).[31] Deville[9] summarized papers related with the preparation of porous ceramics using unidirectional freezing. He explained that the formation of lamellar structure in aqueous slurry with the anisotropy of crystal growth kinetics of water and pointed out the formation of dendritic honeycomb with camphene. However, the method of controlling morphology was not intensively investigated. As summarized in Table 5.4, almost all results of unidirectional freezing that were prepared from aqueous slurry showed lamellar or transitional structure of lamellar and cellular honeycomb. However, very recently, preparation of dendritic honeycomb of titania was reported by Ren et al.[32] They prepared titania aqueous suspensions with ammonium polyacrylate as a dispersant, polyvinyl alcohol as a binder, and polyethylene glycol as a plasticizer. This means that morphology can be intentionally controlled by the addition of several additives, which work as impurities and increase the degree of Mullins-Sekerka instability.

The formation mechanism of lamellar structure with aqueous slurry may be analogous to lamellar eutectic growth. In the case of lamellar eutectic growth, long-range diffusion and solute pile up do not occur at the eutectic composition since the solute rejected by one phase is needed for the growth of the other. In the colloidal

suspension, the existence of particles in the freezing solution does not change the degree of constitutional supercooling and instability. This may be the reason why lamellar structure is formed by unidirectional freezing of aqueous slurry.

As shown in Table 5.4, unidirectional freezing of aqueous alumina slurry, which is believed most pure system, leads to lamella structure formation. Furthermore, Jackson and Hunt[11] reported that the lamellar to dendrite transition of eutectic growth occurred when the volume difference of two phases was very big. The formation of thin fiber with 1 wt% of 80 nm PS nanoparticle suspension is another example showing that the unidirectional freezing of colloidal suspension is analogues to unidirectional eutectic growth. Several research results obtained from aqueous slurry, dealt with system with dispersant and impurities, showed transitional structure of lamellar and cellular honeycomb, continuous open pores with flat shape. Even though the reason was not explained, Gutierrez et al.[33] reported the morphology transition of unidirectionally frozen structure of multiwall carbon nanotube (MWCNT) aqueous suspension with small amount of chitosan (1 wt%). The morphology transited from transitional structure of lamellar and cellular honeycomb (2 wt% of MWCNT) to cellular honeycomb (8 wt%) by the increase of MWCNT. These results can be explained by the change in impurity concentration in slurry. The increase of impurities induced the transition from the system analogues to lamella eutectic growth to the system affected by Mullins-Sekerka instability. To confirm this speculation, the morphology transition of alumina lamellar structure was tested. 0.2 μm alumina powder was used for this experiment (99.99 % purity, TM-5D, Taimei Chemicals Co., Ltd.). PEG with weight average molecular weights of 70,000 were used (Wako Chemicals Ind. Ltd.). PEG was dissolved in distilled water. The concentration of PEG was varied from 2 vol% to 8

vol%. Then, 8 vol% of alumina was added in the solution. The alumina particles were dispersed by stirring and ultrasonic treatment. After dispersion treatment, the alumina colloidal suspension was poured into a PP tube. The prepared tube was unidirectionally frozen at the constant speed of 3.5 cm hr^{-1} by soaking into liquid nitrogen. After freezing the solution completely, the solidified sample was freeze-dried at 268 K for 4 days. The SEM images of the experimental results were shown in Figure 5.4. The morphology was changed from lamella structure (2 vol% of PEG) to transitional structure of lamellar and cellular honeycomb (4 and 6 vol% of PEG), and finally to cellular honeycomb (8 vol% of PEG). As calculated by Tiller et al,[34] the concentration gradient in the liquid near the solid-liquid interface was increased by the decrease in diffusivity that can be caused by the increase of viscosity. Ragnarsson et al.[35] pointed out that the dominating effect of using a polymer solute is the reduction of solute diffusivity. They used purified succinonitrile and poly(ethylene oxide) of varying molecular weight as solvent and solute in their experiment. Furthermore, the formation of dendritic honeycomb from titania aqueous slurry with 0.2 wt% NH_4PAA (Dispersant), 2.5 wt% Poly (vinyl alcohol) (Binder) and 3.8 wt% PEG400 (Plasticizer) coincides with the speculation.[32] As described by Deville,[9] the formation of dendritic honeycomb with camphene slurry was reported several times. This result also can be explained with severe Mullins-Sekerka instability which was caused by the low purity (97 %) and the high cryoscopic constant (-37.6 K kg/mol) of used camphene.

Table 5.4. Summary of materials, used solvents, and morphology (ceramic slurries or colloidal suspensions not accompanying sol-gel reaction) continued.

Materials	Solvent	Morphologies	Reference
0.3 μm alumina aqueous solution	Water	Lamella	36
Alumina with dispersant (Darvan 811, 1 wt% of alumina), PVA (2 wt% of alumina)	Water	Lamella	2
80 nm 1 wt% PS nanoparticle	Water	Round Fiber	37
17-37 vol% HAP with 1 wt% dispersant (Darvan 811) and 1 wt% PVA	Water	Lamella, TLC*	38
Hydroxy aphataite (HAP)	Water	TLC	36
4.9 g (45 μm) of 9.6 g (125 μm) titanium with 3.6ml deionized water, 0.2 wt% agar and 1 μl neutral detergent	Water	TLC	3
28-45 vol% alumina with a small amount of dispersant, Alon A-6114	Water	TLC	39, 40
30 vol% $Al_2O_3/Al(OH)_3$ mixture with Aron A-6114 (1 wt% of powder)	Water	TLC	41
20-30 vol% $Si_3N_4/Y_2O_3/Al_2O_3$ (95/5/2 weight ratio) with a small amount of dispersant, Alon A-6114	Water	TLC	42
$La_{0.6}Sr_{0.4}Co_{0.2}Fe_{0.8}O_3$-delta-$Ce_{0.9}Gd_{0.1}O_{1.95}$	Water	TLC	43
45-65 % ceramic powder/silica sol mixture	Water	TLC	44
22 vol% titanium with 0.2 wt% Agar	Water	TLC	45
30 vol% alumina with 0.53 wt% dispersant (Dolapix CE 64) and 10 wt% binder (Optapix PAF 60)	Water	TLC	46

TLC: transitional structure of lamellar and cellular honeycomb.

Table 5.4. Summary of materials, used solvents, and morphology (ceramic slurries or colloidal suspensions not accompanying sol-gel reaction) continued.

Materials	Solvent	Morphologies	Reference
2-8 wt% MWCNTs or Pt/MWCNTs with small amount of chitosan	Water	TLC, cellular honeycomb	33
10-50 wt% TiO_2 with 0.2 wt% NH4PAA (Dispersant), 2.5 wt% PVA (Binder) and 3.8 wt% PEG400 (Plasticizer)	Water	Dendritic honeycomb	32
20-50 vol% alumina with dispersant (an amine derivative of a fatty acid condensation polymer, Perfad 9100)	Camphene	Dendritic honeycomb	47
5 vol% alumina with 3 wt% dispersant (oligomeric polyester Hypermer KD-4) and 10-30 vol% PS of alumina	Camphene	Dendritic honeycomb	48
20 vol% bioglass (a composition of 46.1 % SiO2, 24.4% Na_2O, 26.9% CaO, and 2.6% P_2O_5 in mol%) with 3 wt% dispersant, KD-4	Camphene	Dendritic honeycomb	49
5-20 vol% alumina with 3 wt% dispersant, KD-4	Camphene	Dendritic honeycomb	50
5-25 wt% polycarbosilane	Camphene	Dendritic honeycomb	51
10 vol% SiC/camphene with polycarbosilane (0-20 wt% of SiC)and 3 wt% dispersant, KD-4	Camphene	Dendritic honeycomb	52
20 vol.% of 1:1 wt.% mixture of nickel oxide (NiO) and yttria-stabilized zirconia (YSZ) doped with 8 mol% Y2O3	Camphene	Dendritic honeycomb	53
10-25 vol% Lead zirconate titanate-lead zinc niobate (PZT-LZN) with 3 wt% dispersant, KD-4	Camphene	Dendritic honeycomb	54

TLC: transitional structure of lamellar and cellular honeycomb.

Table 5.4. Summary of materials, used solvents, and morphology (ceramic slurries or colloidal suspensions not accompanying sol-gel reaction)

Materials	Solvent	Morphologies	Reference
10-20 vol% HAP with 6 wt% dispersant, KD-4	Camphene	Dendritic honeycomb	55, 56, 57
HAP with PS (0-30 vol% of HA), and dispersant, KD4	Camphene	Dendritic honeycomb	58

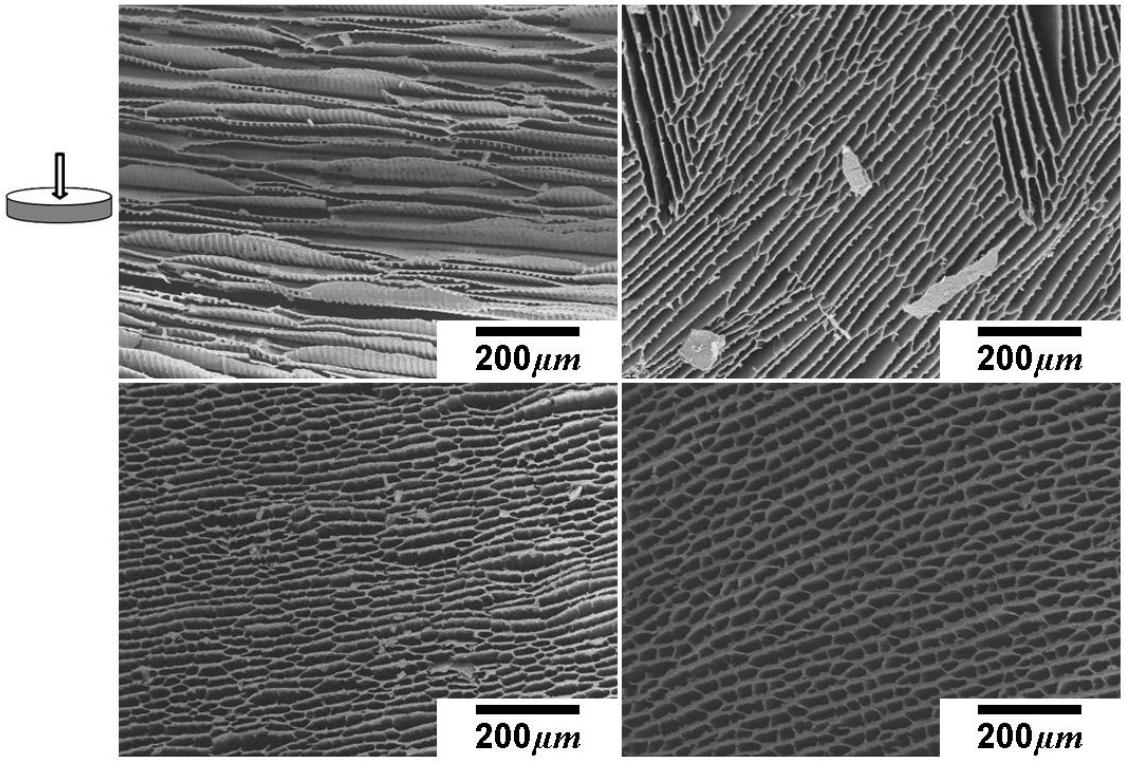

Figure 5.4. Effect of PEG concentration on structure - SEM micrographs of honeycomb monolith structures prepared from Alumina/PEG/water slurry. (a) 8/2/90 volume ratio, (b) 8/4/88 volume ratio, (c) 8/6/86 volume ratio, and (d) 8/8/84 volume ratio.

5.6. Conclusion.

In summary, Mullins-Sekerka instability and Jackson and Hunt theory must be considered to control aligned porous morphology prepared by unidirectional freezing. To control the morphology, the proper selection of solvent and raw material composition is necessary. The relationship between Mullins-Sekerka instability and the structure prepared by unidirectional freezing is summarized in Figure 5.5. By the increase in the degree of Mullins-Sekerka instability, the structure is changed from round fiber and lamellar to transitional structure of lamellar and cellular honeycomb, cellular honeycomb, and finally dendritic honeycomb. The degree of Mullins-Sekerka instability increases with the increase of solute concentration, slope of liquidus line of phase diagram, and diffusivity of solute in the solution. On the opposite, degree of Mullins-Sekerka instability decreases with the increase of interfacial energy, temperature gradient.

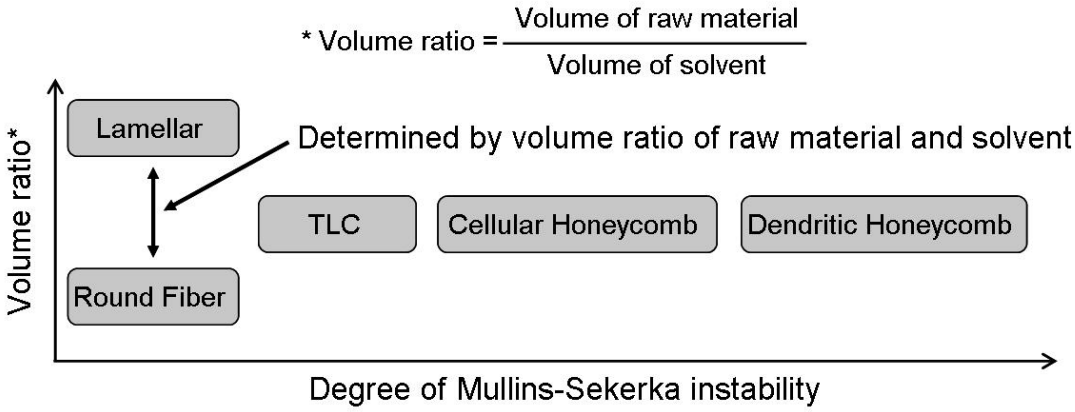

Figure 5.5. Relation of Mullins-Sekerka instability and structure prepared by unidirectional freezing. TLC means transitional structure of lamellar and cellular honeycomb.

Detail strategy to control the morphology of each system can be summarized as follows;

1. Polymer solution

It is better to use water or organic solvent that has low cryoscopic constant for the preparation of cellular honeycomb. To prepare dendritic honeycomb, the addition of impurity or the use of organic solvent instead of water can be helpful. In the case of polymers, which are insoluble in water or solvent with low cryoscopic constant, highly purified organic solvent and polymer have to be used to prepare cellular honeycomb.

2. Colloidal suspension accompanying sol-gel reaction

The morphology can be changed by controlling mobility; the relaxation time of the hydrosol at the time of freezing and the gelation time of the hydrosol, and the elapsed time between gelation and freezing as well as the gelation time of the hydrogel. Sol has to be prepared by special route to prevent contamination by impurities or has to be purified to avoid the formation of dendritic honeycomb.

3. Colloidal suspension not accompanying sol-gel reaction

To prepare lamellar structure, the use of water or organic solvent with low cryoscopic constant is helpful. To prepare round fibers, small volume fraction of particle must be used. To prepare lamellar or round fiber, the raw material has to be purified and the addition of additives must be minimized. On the other hand, to make cellular or dendritic honeycomb, the selection of solvent with high cryoscopic constant or addition of additives such as polymer is necessary.

5.8. Reference

(1) Gutierrez, M. C.; Garcia-Carvajal, Z. Y.; Jobbagy, M.; Rubio, T.; Yuste, L.; Rojo, F.; Ferrer, M. L.; del Monte, F. *Advanced Functional Materials* **2007**, *17*, 3505.

(2) Deville, S.; Saiz, E.; Tomsia, A. P. *Acta Materialia* **2007**, *55*, 1965.

(3) Chino, Y.; Dunand, D. C. *Acta Materialia* **2008**, *56*, 105.

(4) Sofie, S. W.; Dogan, F. *Journal of American Ceramic Society* **2001**, *84*, 6.

(5) Nishihara, H.; Mukai, S. R.; Yamashita, D.; Tamon, H. *Chemistry of Materials* **2005**, *17*, 683.

(6) Zhang, H. F.; Hussain, I.; Brust, M.; Butler, M. F.; Rannard, S. P.; Cooper, A. I. *Nature Materials* **2005**, *4*, 787.

(7) Zhang, R. Y.; Ma, P. X. *Journal of Biomedical Materials Research* **1999**, *44*, 446.

(8) Mukai, S. R.; Nishihara, H.; Tamon, H. *Microporous and Mesoporous Materials* **2008**, *116*, 166.

(9) Deville, S. *Advanced Engineering Materials* **2008**, *10*, 155.

(10) Mullins, W. W.; Sekerka, R. F. *Journal of Applied Physics* **1964**, *35*, 444.

(11) Jackson, K. A.; Hunt, J. D. *Transactions of the Metallurgical Society of Aime* **1966**, *236*, 1129.

(12) Kurz, W.; Fisher, D. J. *Fundamentals of Solidification*; Forth ed.; Trans Tech Publications Ltd.: Zurich, 1998.

(13) Ma, P. X.; Zhang, R. Y. *Journal of Biomedical Materials Research* **2001**, *56*, 469.

(14) Stokols, S.; Tuszynski, M. H. *Biomaterials* **2004**, *25*, 5839.

(15) Van Vlierberghe, S.; Cnudde, V.; Dubruel, P.; Masschaele, B.; Cosijns, A.; De Paepe, I.; Jacobs, P. J. S.; Van Hoorebeke, L.; Remon, J. P.; Schacht, E. *Biomacromolecules* **2007**, *8*, 331.

(16) Zhang, H. F.; Long, J.; Cooper, A. I. *Journal of the American Chemical Society* **2005**, *127*, 13482.

(17) 日本化学会 *化学便覧基礎編 II*; 丸善(株)出版事業部, 1993.

(18) Mahler, W.; Bechtold, M. F. *Nature* **1980**, *285*, 27.

(19) Ding, S. Q.; Zeng, Y. P.; Jiang, D. L. *Journal of the American Ceramic Society* **2007**, *90*, 2276.

(20) Nishihara, H., PhD Dissertation, Kyoto University, 2005.

(21) Kokubo, T.; Teranishi, Y.; Maki, T. *Journal of Non-Crystalline Solids* **1983**, *56*, 411.

(22) Maki, T.; Teranishi, Y.; Kokubo, T.; Sakka, S. *Japan Sangyoukyokaisi* **1985**, *93*, 387.

(23) Maki, T.; Sakka, S. *Journal of Non-Crystalline Solids* **1986**, *82*, 239.

(24) Mukai, S. R.; Nishihara, H.; Tamon, H. *Microporous and Mesoporous Materials* **2003**, *63*, 43.

(25) Mukai, S. R.; Nishihara, H.; Tamon, H. *Chemical Communications* **2004**, 874.

(26) Mukai, S. R.; Nishihara, H.; Shichi, S.; Tamon, H. *Chemistry of Materials* **2004**, *16*, 4987.

(27) Nishihara, H.; Mukai, S. R.; Tamon, H. *Carbon* **2004**, *42*, 899.

(28) Mukai, S. R.; Nishihara, H.; Yoshida, T.; Taniguchi, K.; Tamon, H. *Carbon* **2005**, *43*, 1563.

(29) Mukai, S. R.; Nishihara, H.; Tamon, H. *Catalysis Surveys from Asia* **2006**, *10*, 161.

(30) Nishihara, H.; Mukai, S. R.; Fujii, Y.; Tago, T.; Masuda, T.; Tamon, H. *Journal of Materials Chemistry* **2006**, *16*, 3231.

(31) Araki, K.; Halloran, J. W. *Journal of the American Ceramic Society* **2004**, *87*, 1859.

(32) Ren, L. L.; Zeng, Y. P.; Jiang, D. L. *Journal of the American Ceramic Society* **2007**, *90*, 3001.

(33) Gutierrez, M. C.; Hortiguela, M. J.; Amarilla, J. M.; Jimenez, R.; Ferrer, M. L.; del Monte, F. *Journal of Physical Chemistry C* **2007**, *111*, 5557.

(34) Tiller, W. A.; Jackson, K. A.; Rutter, J. W.; Chalmers, B. *Acta Metallurgica* **1953**, *1*, 428.

(35) Ragnarsson, R.; UTTER, B.; BODENSCHATZ, E. In *Proceedings of the Materials Research Society Symposium* 1997; Vol. 481, p 65.

(36) Deville, S.; Saiz, E.; Nalla, R. K.; Tomsia, A. P. *Science* **2006**, *311*, 515.

(37) Yan, J.; Chen, Z.; Jiang, J.; Tan, L.; Zeng, X. C. *Advanced Materials* **2009**, *21*, 314.

(38) Deville, S.; Saiz, E.; Tomsia, A. P. *Biomaterials* **2006**, *27*, 5480.

(39) Fukasawa, T.; Ando, M.; Ohji, T.; Kanzaki, S. *Journal of American Ceramic Society* **2001**, *84*, 230.

(40) Fukasawa, T.; Deng, Z. Y.; Ando, M.; Ohji, T.; Goto, Y. *Journal of Materials Science* **2001**, *36*, 2523.

(41) Fukasawa, T.; Deng, Z. Y.; Ando, M.; Ohji, T. *Journal of the Ceramic Society of Japan* **2001**, *109*, 1035.

(42) Fukasawa, T.; Deng, Z. Y.; Ando, M.; Ohji, T.; Kanzaki, S. *Journal of the American Ceramic Society* **2002**, *85*, 2151.

(43) Moon, J. W.; Hwang, H. J.; Awano, M.; Maeda, K.; Kanzaki, S. *Journal of the Ceramic Society of Japan* **2002**, *110*, 479.

(44) Koch, D.; Andresen, L.; Schmedders, T.; Grathwohl, G. *Journal of Sol-Gel Science and Technology* **2003**, *26*, 149.

(45) Fife, J. L.; Li, J. C.; Dunand, D. C.; Voorhees, P. W. *Journal of Materials Research*

2009, *24*, 117.

(46) Waschkies, T.; Oberacker, R.; Hoffmann, M. J. *Journal of the American Ceramic Society* **2009**, *92*, S79.

(47) Araki, K.; Halloran, J. W. *Journal of the American Ceramic Society* **2005**, *88*, 1108.

(48) Koh, Y. H.; Lee, E. J.; Yoon, B. H.; Song, J. H.; Kim, H. E.; Kim, H. W. *Journal of the American Ceramic Society* **2006**, *89*, 3646.

(49) Song, J. H.; Koh, Y. H.; Kim, H. E.; Li, L. H.; Bahn, H. J. *Journal of the American Ceramic Society* **2006**, *89*, 2649.

(50) Koh, Y. H.; Song, J. H.; Lee, E. J.; Kim, H. E. *Journal of the American Ceramic Society* **2006**, *89*, 3089.

(51) Yoon, B. H.; Lee, E. J.; Kim, H. E.; Koh, Y. H. *Journal of the American Ceramic Society* **2007**, *90*, 1753.

(52) Yoon, B. H.; Park, C. S.; Kim, H. E.; Koh, Y. H. *Journal of the American Ceramic Society* **2007**, *90*, 3759.

(53) Koh, Y. H.; Sun, J. J.; Kim, H. E. *Materials Letters* **2007**, *61*, 1283.

(54) Lee, S. H.; Jun, S. H.; Kim, H. E.; Koh, Y. H. *Journal of the American Ceramic Society* **2007**, *90*, 2807.

(55) Lee, E. J.; Koh, Y. H.; Yoon, B. H.; Kim, H. E.; Kim, H. W. *Materials Letters* **2007**, *61*, 2270.

(56) Yoon, B. H.; Koh, Y. H.; Park, C. S.; Kim, H. E. *Journal of the American Ceramic Society* **2007**, *90*, 1744.

(57) Yoon, B. H.; Park, C. S.; Kim, H. E.; Koh, Y. H. *Materials Letters* **2008**, *62*, 1700.

(58) Yook, S. W.; Kim, H. E.; Yoon, B. H.; Soon, Y. M.; Koh, Y. H. *Materials Letters* **2009**, *63*, 955.

Chapter VI

General Conclusion

In this dissertation, the preparation of honeycomb monolith structure using the unidirectional freezing of polymer solutions and a colloidal suspension has been investigated and the morphologies have been manipulated using the addition of third component, phase separation of polymer blend and leaching of polymer, and burning out of polymer particles. The key factors for controlling the aligned porous morphology have been fully investigated. The detailed contents were summarized for each chapter as follows.

In chapter II, honeycomb monolith structures of PLLA were successfully prepared by the unidirectional freezing and a subsequent solvent sublimation. Water content and polymer concentration were key factors for the creation of ladder-like structures in aligned microchannels. The interconnectivity of aligned channels could be controlled by the concentration of polymer and the addition amount of water. The microscale channel diameter and the number density of pore channel per unit cross section perpendicular to the aligned direction were controlled by the PLLA concentration and the freezing rate. The wall thickness of channel wall was also controlled by the PLLA concentration and freezing rate.

In chapter III, honeycomb monolith-structured PLLA with micro/nanoscale porous walls was successfully fabricated by combining the unidirectional freezing technique and the phase separation of the polymer blend solution. PEG was used to create pores in the microchannel wall in the honeycomb monolith structure. The pore

size was controlled by the onset time of liquid-liquid phase separation by changing the molecular weight of the PEG as well as the blend ratio of PLLA/PEG. The effect of PEG molecular weight on the freezing point depression was investigated by the freezing point measurement. A ternary phase diagram for PLLA, PEG, and 1,4-dioxane was obtained from cloud point measurements data. Based on the measurement of the freezing point depression and the phase diagram, hypotheses for the mechanism of the cellular-dendritic transition and the formation mechanism of the pores in the channel walls were proposed.

In chapter IV, unidirectional freezing scheme was proposed as a simple method for packing colloidal silica and preparing honeycomb monolith-structured silica, with highly ordered, three-dimensionally interconnected macroporous walls. Relatively large size inverse opal structure, which has aligned micro-scale channels, was successfully produced using this method. The experimental results indicated that three-dimensionally interconnected macroporous structures develop by the spontaneous self-organization of two kinds of particles in the growing ice template.

In chapter V, the key factors to control the aligned porous morphology were investigated by reviewing several papers. To discuss the control of morphology, several papers were classified by used raw materials; polymer solution, colloidal suspension which is accompanying sol-gel reaction, ceramic slurry or colloidal suspension which is not accompanying sol-gel reaction. The importance of Mullins-Sekerka instability was discussed with several cases. To control Mullins-Sekerka instability, the proper selection of solvent and raw material composition is necessary. Detail strategies to control the morphology of each system were summarized respectively.

As can be seen above, the preparation and the control of morphology of

honeycomb monolith structure were experimentally investigated and were discussed by reviewing several papers. The result showed that general formation mechanism is based on the growth morphology of solvent crystal, which is affected by impurities and the properties of solvent itself.

The transition of cellular to dendritic honeycomb (In chapter II and III) and the transition of lamellar to cellular honeycomb (In chapter V) were shown in this thesis. However, the preparation of all morphologies (round fiber, lamellar, transitional structure of lamellar and cellular honeycomb, and dendritic honeycomb) with same raw materials and solvent is not reported. Thus, further study to verify the speculation of chapter V must be conducted in the future. Despite of unique properties such as aligned channel, high contact efficiency, and high permeability, there are not so many research results to utilize the structure prepared by unidirectional freezing. Further studies should be conducted for the utilization of these novel porous structures.

Appendix I

Stability of a Planar Interface during Solidification of a Dilute Binary Alloy: Mullins-Sekerka Instability

A1.1. Introduction

As shown in Fig. A1.1, for the case in which a single phase solid is formed, the equilibrium concentration of solute in the solid at the interface between solid and liquid is different from the equilibrium concentration of solute in the liquid adjacent to it. In the case of unidirectional freezing, solute is expelled continuously from solid and diffuse toward liquid phase. This causes the instability of liquid-solid interface. n is the partition coefficient given by the ratio of the equilibrium concentration of solute on the solid side of the interface to that on the liquid side of the interface

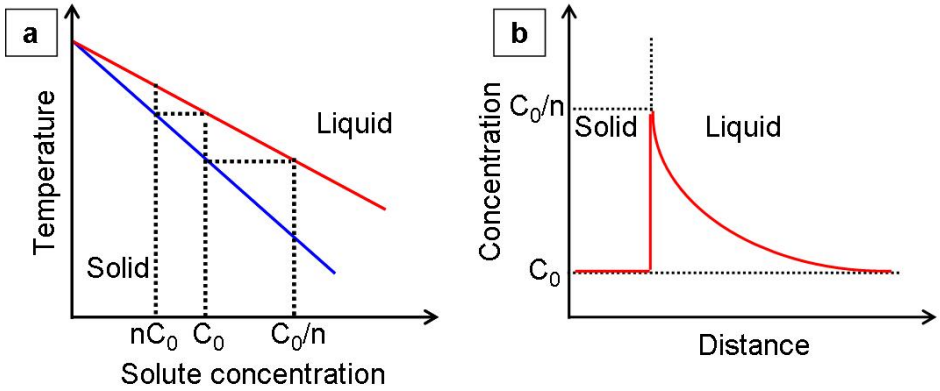

Figure A1.1. The redistribution of solute during the unidirectional freezing of dilute solution. a) portion of phase diagram of binary solution and b) distribution of solute at steady state condition.

The stability of a planar interface during unidirectional freezing has been studied systematically by Mullins and Sekerka. They considered a planar interface moving along z-axis with constant velocity V as shown in Fig. A1.2.

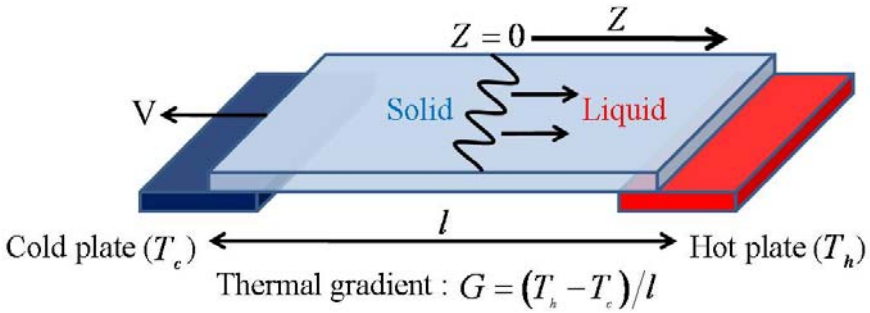

Figure A1.2. A solid-liquid interface moving along z-axis with constant velocity.

The stability of the planar interface was analyzed by calculating the time dependence of the amplitude of a sinusoidal perturbation of infinitesimal initial amplitude introduced into the shape of the plane.

$$Z = \phi(x,t) = \delta(t)\sin\omega x \qquad \text{(A1.1)}$$

$\delta(t)$: Amplitude

ω: The frequency of the sinusoidal ripple

$\lambda = 2\pi/\omega$: The wave length of a sinusoidal perturbation

The solid-liquid interface is unstable if any sinusoidal wave grows. This is determined by $\dot{\delta} \equiv \frac{d\delta}{dt}$. If $\dot{\delta} > 0$ within a range of the wave length the ripple grows and if $\dot{\delta} < 0$ at whole rage of the wave length the ripple decays.

To calculate $\dot{\delta}$, it is required the calculation of the velocity $v(x)$ of each element

of interface, as a function of its position x, in terms of the values of the local thermal and diffusion gradients. The average moving rate of the solid-liquid interface, the average growth rate of the solid, is an average of $v(x)$ in one wavelength.

$$V = \frac{1}{\lambda}\int_0^{\lambda} v(x)\,dx$$

A1.2. Calculation of the Time Derivative $\dot{\delta}$ of the Amplitude of a Fourier Perturbation

The expressions of composition and temperature must satisfy the appropriate steady-state equations. In a coordinate frame that moves with a constant velocity, V and with the origin at z=0, as shown in Figure A1.2, the steady-state differential equations for the thermal and diffusion fields are

For the liquid

$$\nabla^2 C + \left(\frac{V}{D}\right)\left(\frac{\partial C}{\partial z}\right) = 0 \qquad \text{(A1.2a)}$$

$$\nabla^2 T + \left(\frac{V}{D_{th}}\right)\left(\frac{\partial T}{\partial z}\right) = 0 \qquad \text{(A1.2b)}$$

For the solid

$$\nabla^2 T' + \left(\frac{V}{D_{th}'}\right)\left(\frac{\partial T'}{\partial z}\right) = 0 \qquad \text{(A1.2c)}$$

V : Constant mean velocity of the interface with respect to either phase

C : Concentration of solute in the liquid

T and T' : Temperature in the liquid and solid

D : Diffusion coefficient of solute in the liquid

$D_{th} = k_L / C_L$ and $D_{th}' = k_S / C_S$: Thermal diffusivity of the liquid and solid

k_S and k_L : Conductivity of solid and liquid

C_L and C_S : Specific heat of the liquid and solid/unit volume

A1.2.1. Thermal and Diffusion Equation for the Flat Interface.

To calculate the steady-state solutions of perturbed interface, an unperturbed flat interface has to be solved. For solute diffusion in the liquid phase, the solution of differential equation is

$$C = A + Be^{-\frac{V}{D}z}$$

As shown in Figs. A1.1 and A1.2, Boundary conditions for flat interface are

$$C(z=0) = C_0$$
$$C(z=\infty) = nC_0$$
$$-D\left(\frac{dC}{dz}\right)_{z=0} = G_C$$

n : The partition coefficient given by the ratio of the equilibrium concentration of solute on the solid side of the interface to that on the liquid side of the interface

C_0 : The solute concentration on the liquid side of the interface at steady-state

G_c : The concentration gradient in the liquid at the interface

Thus, diffusion equation is

$$C = nC_0 + (1-n)C_0 e^{-\frac{V}{D}z}$$

$$C = C_0 + C_0(n-1)\left(1 - e^{-\frac{V}{D}z}\right) = C_0 + \left(\frac{G_c D}{V}\right)\left(1 - e^{-\frac{V}{D}z}\right) \quad \text{(A1.3a)}$$

And similarly the thermal equations are

$$T = T_0 + \left(\frac{G'D_{th}}{V}\right)\left(1 - e^{-\left(\frac{V}{D_{th}}\right)z}\right) \tag{A1.3b}$$

$$T = T_0 + \left(\frac{G'D_{th}'}{V}\right)\left(1 - e^{-\left(\frac{V}{D_{th}'}\right)z}\right) \tag{A1.3c}$$

C_0 : Solute concentration of liquid for a flat interface

T_0 : Temperature for a flat interface

G_C : Concentration gradient in the liquid at the flat interface

G and G' : Thermal gradients in the liquid and solid at the flat interface

A1.2.2. Calculation of Thermal and Diffusion Equation for the Perturbed Interface

Eqs. A1.2 must satisfy the correct boundary conditions at infinity. i.e., C, T, and T' should agree with the equations, Eqs. A1.3, for the flat interface ($\delta = 0$) at several wavelengths from the interface. Eqs. (A1.2) must satisfy the following two boundary conditions at the perturbed interface, $z = \phi$. First, According to the phase diagram and assumption of local interface equilibrium must hold on the interface.

$$T_\phi = mC_\phi + T_N \tag{A1.4a}$$

$$T_N = T_M + T_M \Gamma K = T_M - T_M \delta\omega^2 \sin\omega x \tag{A1.4b}$$

m : The slope of the liquidus line on the phase diagram including sign

T_N : The temperature in the absence of solute at the perturbed interface

T_M : The melting temperature of a flat interface

K : The average curvature at a point of the interface

$\Gamma = \sigma / L$: Capillary constant

σ : The specific liquid-solid interfacial free energy

L : The latent heat of the solvent per unit volume

The second condition that must be satisfied at the interface is that the velocity $v(x)$ at each element of interface calculated from heat flow consideration must agree with the velocity calculated from diffusion consideration

$$v(x) = \frac{1}{L}\left(k_S \left(\frac{\partial T'}{\partial z} \right)_\phi - k_L \left(\frac{\partial T}{\partial z} \right)_\phi \right) = \frac{D}{C_\phi (n-1)} \left(\frac{\partial T}{\partial z} \right)_\phi \tag{A1.5}$$

For the geometry of sinusoidal ripple, the temperature and concentration at the interface takes the expressions of

$$T_\phi = T_0 + a\delta(t)\sin(\omega x) = T_0 + a\varphi \tag{A1.6a}$$

$$C_\phi = C_0 + b\delta(t)\sin(\omega x) = C_0 + b\varphi \tag{A1.6b}$$

Where, T_0 and C_0 are the values for a flat interface and the second terms are the first-order corrections corresponding to the infinitesimal ripple

The solution of Eq. A1.2a can be solved using the method of separation of variables

Let $C(x,z) = X(x)Z(z)$

$\frac{\partial^2 C}{\partial x^2} = X''Z$, $\frac{\partial^2 C}{\partial z^2} = XZ''$, and $\frac{\partial C}{\partial z} = XZ'$

$X''Z + XZ'' + (V/D)XZ' = 0$

$\frac{Z'' + (V/D)Z'}{Z} = -\frac{X''}{X} = \omega^2$

$Z'' + (V/D)Z' - \omega^2 Z = 0$ and $X'' + \omega^2 Y = 0$

For Z

$Z = Ae^{\lambda_1 Z} + Be^{\lambda_2 Z}$

$$\lambda_1 = \frac{1}{2}(-V/D + \sqrt{(V/D)^2 + \omega^2}) = -\left\{(V/2D) - \left[(V/2D)^2 + \omega^2\right]^{\frac{1}{2}} > 0$$

$$\lambda_2 = \frac{1}{2}(-V/D - \sqrt{(V/D)^2 + \omega^2}) = -\left\{(V/2D) + \left[(V/2D)^2 + \omega^2\right]^{\frac{1}{2}} < 0$$

Thus, $A = 0$. Set $B = 1$

$$Z = e^{\lambda_2 Z}$$

The solution of Y is

$$Y = E\sin(\omega x) + F\cos(\omega x)$$

Thus, the general solution of diffusion equation is

$$C(x,z) = e^{\lambda_2 z}\left(E\sin(\omega x) + F\cos(\omega x)\right) + G$$

This solution should agree with the general solution of diffusion equation for flat interface ($\delta = 0$) at several wavelengths from the interface. From general solution of diffusion equation for flat interface, Eq. A1.2a

$$\mathrm{C}(x,z) = C_0 + (G_C D/V)(1 - e^{-(V/D)z}) + \left\{E\sin(\omega x) + F\cos(\omega x)\right\} e^{\lambda_2 z}$$

At the interface, $C(0,0) = C_0$

Thus $F = 0$

$$\mathrm{C(x,z)} = C_0 + (G_C D/V)(1 - e^{-(V/D)z}) + E\sin(\omega x)e^{\lambda_2 Z}$$

This solution can be simplified using Taylor's theorem. On the interface $z = \phi\ (nor\ z = 0)$, $\mathrm{z} = \delta\sin\omega x$. $C(x,z)$ must satisfy Eq. A1.6b.

$$C_\varphi \cong C_0 - G_C\delta\sin\omega x + E\sin(\omega x) = C_0 + b\delta\sin\omega x$$

$$G = \delta(b - G_C)$$

Finally

$$C(x,z) - C_0 = (G_C D/V)(1 - e^{-(V/D)z}) + \delta(b - G_C)\sin\omega x e^{-\omega^* Z}$$

$$\omega^* = (V/2D) + \left[(V/2D)^2 + \omega^2 \right]^{\frac{1}{2}}$$

The required expressions satisfying Eqs. A1.2 and A1.3 and reducing to Eq. A1.6 on the interface $z = \phi$ are the following:

$$C(x,z) - C_0 = (G_c D/V)\left(1 - e^{-(V/D)z}\right) + \delta(b - G_c)\sin(\omega x)e^{-\omega^* z} \tag{A1.7}$$

$$T(x,z) - T_0 = (GD_{th}/V)\left(1 - e^{-(V/D_{th})z}\right) + \delta(a - G)\sin(\omega x)e^{-\omega_{th} z} \tag{A1.8}$$

$$T'(x,z) - T_0 = (G' D_{th}'/V)\left(1 - e^{-(V/D_{th}')z}\right) + \delta(a - G')\sin(\omega x)e^{-\omega_{th}' z} \tag{A1.9}$$

where

$$\omega^* = (V/2D) + \left[(V/2D)^2 + \omega^2 \right]^{\frac{1}{2}} \tag{A1.10a}$$

$$\omega_{th} = (V/2D_{th}) + \left[(V/2D_{th})^2 + \omega^2 \right]^{\frac{1}{2}} \tag{A1.10b}$$

$$\omega_{th}' = (V/2D_{th}') - \left[(V/2D_{th}')^2 + \omega^2 \right]^{\frac{1}{2}} \tag{A1.10c}$$

The gradients of the thermal and diffusion fields at the interface calculated form Eqs. A1.7, 8, and 9 to the first order in δ are

$$\begin{aligned} \left(\frac{\partial C}{\partial z}\right)_{\varphi} &= G_c e^{-(V/D)\delta\sin(\omega x)} - \omega^* \delta(b - G_c)\sin(\omega x)e^{-\omega^*\delta\sin(\omega x)} \\ &\approx -\omega^* \left\{ b - G_c \left[1 - (V/\omega^* D) \right] \right\} \delta \sin(\omega x) + G_c \end{aligned} \tag{A1.11}$$

Similarly

$$\begin{aligned} \left(\frac{\partial T}{\partial z}\right)_{\phi} &\approx -\omega_{th} \left\{ a - G\left[1 - (V/\omega_{th} D_{th}) \right] \right\} \delta \sin(\omega x) + G \\ \left(\frac{\partial T}{\partial z}\right)_{\phi} &\approx -\omega(a - G)\delta \sin(\omega x) + G \end{aligned} \tag{A1.12}$$

$$\left(\frac{\partial T'}{\partial z}\right)_{\varphi} \approx -\omega_{th}{}' \left\{a - G'\left[1 - \left(V / \omega_{th} D_{th}{}'\right)\right]\right\}\delta \sin\left(\omega x\right) + G'$$
$$\left(\frac{\partial T'}{\partial z}\right)_{\varphi} \approx \omega(a - G')\delta \sin\left(\omega x\right) + G' \qquad \text{(A1.13)}$$

Put Eqs. A1.11, 12, and 13 into Eq. A1.5 and integrate with respect to x over an interval of one wave length

$$V \equiv \frac{1}{\lambda}\int_0^{\lambda} v\left(x\right) dx = \frac{1}{L}(k_S G' - k_L G) \qquad \text{(A1.14)}$$

$$V \equiv \frac{1}{\lambda}\int_0^{\lambda} v\left(x\right) dx = \frac{D}{C_0(n-1)} G_C = \frac{Dn}{C_\infty\left(n-1\right)} G_c \qquad \text{(A1.15)}$$

In order to determine a and b, Put Eqs. A1.7, 8, and 9 into Eqs. A1.4 and 5 with the aid of Eqs. A1.11-15.

$$T_\phi = mc_\phi + T_m + T_m \Gamma K = mc_\phi + T_m + T_m \Gamma \left(\frac{\partial^2 z}{\partial x^2}\right)_\phi = mc_\phi + T_m - T_m \Gamma \delta \omega^2 \sin \omega x$$

$$T_\phi = T_0 + a\delta \sin \omega x = m(C_0 + b\delta \sin \omega x) + T_m - T_m \Gamma \delta \omega^2 \sin \omega x$$

Because $T_0 = mC_0 + T_m$, above equation will be

$$a\delta \sin \omega x = mb\delta \sin \omega x - T_m \Gamma \delta \omega^2 \sin \omega x$$

Thus, $a = mb - T_m \Gamma \omega^2$ (A1.16)

$$b = \frac{2G_c T_m \Gamma \omega^3 + \omega G_c\left(\wp' + \wp\right) + G_c\left[\omega^* - \left(V / D\right)\right]\left(\wp' - \wp\right)}{\omega^*(\wp' - \wp) + 2\omega m G_c - (\bar{k}p / DL)\left(\wp' - \wp\right)^2}$$
$$b = \frac{2G_c T_m \Gamma \omega^3 + \omega G_c\left(\wp' + \wp\right) + G_c\left[\omega^* - \left(V / D\right)\right]\left(\wp' - \wp\right)}{2\omega m G_c + \left(\wp' - \wp\right)\left[\omega^* - \left(V / D\right) p\right]} \qquad \text{(A1.17)}$$

where

$$\bar{k} = \frac{1}{2}(k_S + k_L)$$

$$\wp = (k_L / \bar{k})G$$

$$\wp' = (k_S / \bar{k})G'$$

$$p = 1 - n$$

To determine δ, Substitute Eqs. A1.8 and 9 into Eqs. A1.5.

$$v(x) \approx V + \dot{\delta}\sin\omega x = (\bar{k} / L)(\wp' - \wp) + (\bar{k} / L)\omega\{2a - (\wp' + \wp\}\delta\sin\omega x \qquad \text{(A1.18)}$$

Thus, $V = (\bar{k} / L)(\wp' - \wp)$ (A1.19)

And $\dot{\delta} = (\bar{k} / L)\omega\{2a - (\wp' + \wp\}\delta\sin\omega x$ (A1.20)

Substituting for a in Eq. A1.20 by using Eqs.A1.16 and 17

$$\frac{\dot{\delta}}{\delta} = \frac{V\omega\left\{-2T_m\Gamma\omega^2\left[\omega^* - (V/D)p\right] - (\wp' + \wp)\left[\omega^* - (V/D)p\right] + 2mG_c\left[\omega^* - (V/D)\right]\right\}}{2\omega mG_c + (\wp' - \wp)\left[\omega^* - (V/D)p\right]}$$

(A1.21)

A1.3. Analysis of the Stability of the Planar Interface.

To analyze the Eq. A1.21, we must consider the sign of the denominator and numerator of Eq. A1.21. The denominator of Eq. A1.21 is always positive because

1) ωmG_c is always positive because m and G_c have same sign.

2) $(\wp' - \wp) = \dfrac{k_s G' - k_L G}{\bar{k}} = \dfrac{VL}{\bar{k}} > 0$.

3) From Eq. A1.10a, $\omega^* - V/D > 0$ and $\omega^* - Vp/D > 0$ because $0 < p < 1$.

The numerator of Eq. A1.21 can be expressed as

$$2v\omega\left[\omega^* - (V/D)p\right]S(\omega) \qquad \text{(A1.22)}$$

$$S(\omega) = -T_m\Gamma\omega^2 - \frac{1}{2}(\wp' + \wp) + mG_C\frac{\left[\omega^* - (V/D)\right]}{\left[\omega^* - (V/D)p\right]} \qquad \text{(A1.23)}$$

Eq. A1.22 is always positive. Thus, the question of whether $\dot{\delta}$ has positive value turns into the question of whether Eq. A1.23 is positive or not. The first term of above equation is related to interface energy and is always negative. The larger interface energy possesses more stable interface. The second term is about the gradient of temperature around interface. The positive gradient of temperature around interface helps to maintain interface stable. The third term is about the effect of the solute diffusion on the interface stability. When $V/D \ll 1$, the third term approaches to $2mG_C$. This means that steep slope of liquidus line or high concentration gradient lead to instability. In summary, the instability of interface is determined by the competition of interface energy, temperature gradient, concentration gradient and slope of liquid line. Slope of liquidus line is determined by the value of cryoscopic constant.

Appendix II

Lamellar and Rod Eutectic Growth: Jackson and Hunt Theory

A2.1. Introduction

As shown in Figure A2.1, lamellar or rods structure is usually formed by unidirectional freezing of eutectic alloy. The formation of lamella and rods structure is investigated by Jackson and Hunt. They analyzed the conditions for stability of rod and lamellar structures. They concluded that stable growth occurs at or near the minimum interface undercooling for a given growth rate and that the growth of rod-type eutectic occurs when the volume difference of two phases is very big.

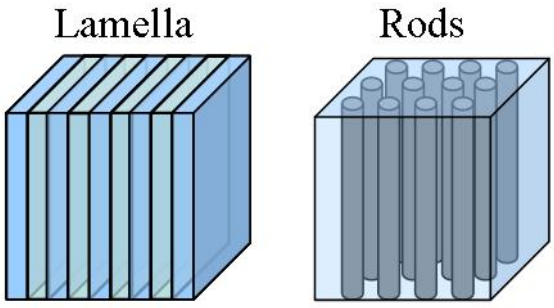

Figure A2.1. Schematic representation of lamellar and rods structure prepared by unidirectional freezing of eutectic alloy

To determine the conditions for stability of rod and lamellar structure, they derived equation for undercooling by combining freezing point depressions by average

composition and average curvature. To calculate average composition in front of liquid interface, they solved the steady-state solution for the diffusion equations for a lamellar and rods type eutectic growth. Equation for average curvature of lamellar and rods structure was also derived.

A2.2. Diffusion in Lamellar Growth

To calculate the average composition of liquid in front of α and β phase, consider a plane interface, with S_α and S_β respectively half the widths of α and β phases as shown in Fig. A2.2. The interface is assumed to be advancing in the z direction with velocity V, at steady-state.

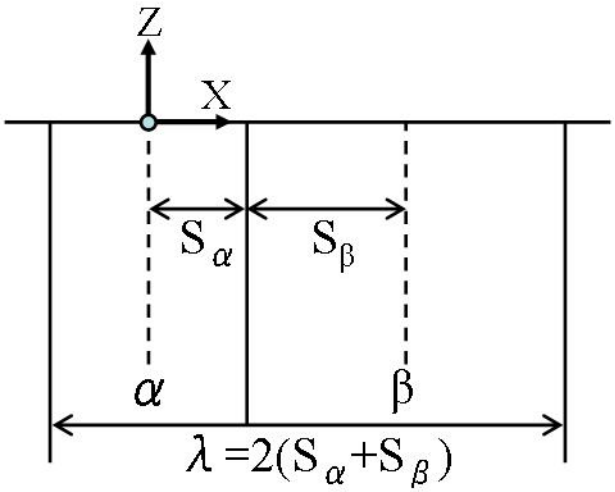

Figure A2.2. Planar lamellar eutectic interface showing definition of S_α and S_β and the coordinate system.

For steady-state growth with the coordinate system moving with velocity V in the z direction, the diffusion equation becomes

$$\Delta^2 C + \frac{V}{D}\frac{\partial C}{\partial z} = 0 \qquad \text{(A2.1)}$$

$$\frac{\partial^2 C}{\partial x^2}+\frac{\partial^2 C}{\partial z^2}+\frac{V}{D}\frac{\partial C}{\partial z}=0$$

With the boundary conditions,

$$C = C_E + C_\infty \quad \text{at} \quad z=\infty$$

$$\frac{\partial C}{\partial x}=0 \quad \text{at} \quad x=0 \quad \text{and} \quad x=S_\alpha+S_\beta$$

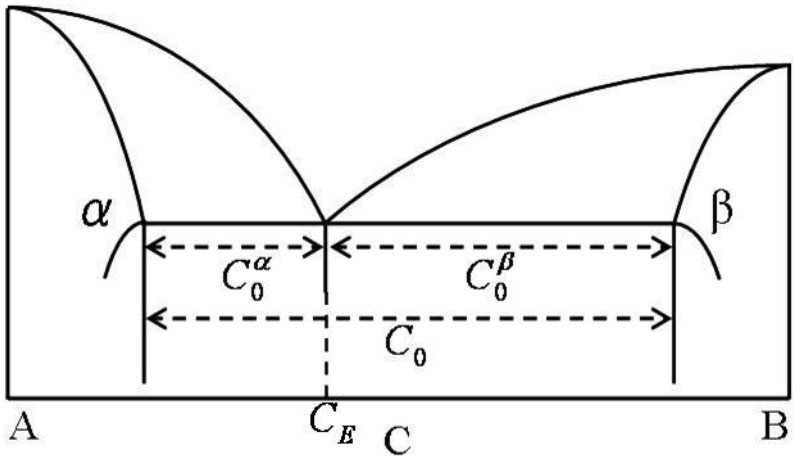

Figure A2.3. Phase diagram showing definition of C_0, C_0^α, and C_0^β.

The conservation of matter at the interface requires

$$\left(\frac{\partial C}{\partial z}\right)_{z=0}=-\frac{VC_0^\alpha}{D} \qquad 0 \le x < S_\alpha$$

$$\left(\frac{\partial C}{\partial z}\right)_{z=0}=\frac{VC_0^\beta}{D} \qquad S_\alpha < x \le S_\alpha + S_\beta \qquad \text{(A2.2)}$$

D : Diffusion coefficient

C_E : Eutectic composition

C_∞ : The difference between the eutectic composition and the actual composition far from the interface.

C_0^α and C_0^β : The amounts of B and A, respectively, rejected when unit volume

of the α and ß phase freeze, as shown in Fig. A2.3.

The solution of Eq. A2.1 can be solved using the method of separation of variables.

$Let\ C(x,z) = X(x)Z(z)$

$$X''Z + XZ'' + \frac{V}{D}XZ' = 0$$

$$\frac{Z'' + (V/D)Z'}{Z} = -\frac{X''}{X} = \omega^2$$

$$X'' + \omega^2 Y = 0$$

$$Z'' + (V/D)Z' - \omega^2 Z = 0$$

For X

$$X(x) = A\sin\omega x + B\sin\omega x$$

For Z

$$Z = Ee^{\lambda_1 Z} + Fe^{\lambda_2 Z} = Fe^{\lambda_2 Z}$$

$$\lambda_1 = -\frac{V}{2D} + \sqrt{(\frac{V}{2D})^2 + \omega^2} > 0$$

$$\lambda_2 = -\frac{V}{2D} - \sqrt{(\frac{V}{2D})^2 + \omega^2} < 0$$

Thus, $\lambda_1 = 0$. Set $F = 1$

$$Z = e^{\left(-\frac{V}{2D} - \sqrt{(\frac{V}{2D})^2 + \omega^2}\right)Z}$$

Thus, the general solution of diffusion equation is

$$C(x,z) = (A\sin\omega x + B\cos\omega x)e^{\lambda_2 z} + G$$

By the boundary condition $C = C_E + C_\infty$ at $z = \infty$

$$G = C_E + C_\infty$$

$$\frac{\delta C}{\delta x} = (A\omega\cos\omega x - B\omega\sin\omega x)e^{\lambda_2 z}$$

By the boundary condition $\frac{\partial C}{\partial x} = 0$ at $x = 0$ and $x = S_\alpha + S_\beta$

$$\left(\frac{\delta C}{\delta x}\right)_{x=0} = (A\omega)e^{\lambda_2 z} = 0 \quad \text{hence,} \quad A = 0$$

$$\left(\frac{\delta C}{\delta x}\right)_{x=s_\alpha+s_\beta} = -B\omega \sin\left\{\omega(s_\alpha + s_\beta)\right\} e^{\lambda_2 z} = 0$$

Hence, $\omega = \dfrac{n\pi}{s_\alpha + s_\beta}$, n is integer

Thus infinitely many solutions are obtained $X(x) = X_n(x)$, where

$$X_n(x) = B\cos\left(\frac{n\pi}{S_\alpha + S_\beta}\right)$$

A general solution of Eq. A2.1 is

$$C_n(x,z) = C_E + C_\infty + B\cos\left(\frac{n\pi}{S_\alpha + S_\beta}\right) \times e^{\left(-\frac{V}{2D} - \sqrt{(\frac{V}{2D})^2 + (\frac{n\pi}{S_\alpha + S_\beta})^2}\right)}$$

Clearly, a single solution $C_n(x,z)$ will not satisfy the conditions of the conservation of matter, Eqs. A2.2, at the interface. To obtain a solution that stratifies these conditions, the infinite series must be considered. Thus the solution of Eq. A2.1 is

$$C(x,z) = C_E + C_\infty + \sum_{n=0}^{\infty} B_n \cos\left(\frac{n\pi}{S_\alpha + S_\beta}\right) \times e^{\left(-\frac{V}{2D} - \sqrt{(\frac{V}{2D})^2 + (\frac{n\pi}{S_\alpha + S_\beta})^2}\right)}$$

This reduces to

$$C(x,z) = C_E + C_\infty + B_0 e^{-\frac{V}{D}z} + \sum_{n=1}^{\infty} B_n \cos\left(\frac{n\pi}{S_\alpha + S_\beta}\right) \times e^{-\frac{n\pi z}{S_\alpha + S_\beta}} \qquad \text{(A2.3)}$$

Since $\dfrac{n\pi}{S_\alpha + S_\beta} >> \dfrac{V}{D}$ for $n > 0$

To evaluate the Fourier coefficients that satisfies the conservation of matter,

$$\frac{\delta C}{\delta z} = -\frac{V}{D} B_0 e^{-\frac{V}{D}z} - \frac{n\pi}{S_\alpha + S_\beta} \sum_{n=1}^{\infty} B_n \cos\left(\frac{n\pi x}{S_\alpha + S_\beta}\right) e^{-\frac{n\pi z}{S_\alpha + S_\beta}}$$

$$\left(\frac{\delta C}{\delta z}\right)_{z=0} = -\frac{V}{D}B_0 - \frac{n\pi}{S_\alpha + S_\beta}\sum_{n=1}^{\infty} B_n \cos\left(\frac{n\pi x}{S_\alpha + S_\beta}\right)$$

Using Euler formulas of Fourier series,

$$-\frac{V}{D}B_0 = \frac{1}{S_\alpha + S_\beta}\left(\int_0^{S_\alpha}\left(\frac{\delta C}{\delta z}\right)_{z=0} dx + \int_{S_\alpha}^{S_\alpha+S_\beta}\left(\frac{\delta C}{\delta z}\right)_{z=0} dx\right)$$

$$= \frac{1}{S_\alpha + S_\beta}\left(-\frac{VC_0^\alpha S_\alpha}{D} + \frac{VC_0^\beta S_\beta}{D}\right)$$

$$B_0 = \frac{C_0^\alpha S_\alpha - C_0^\beta S_\beta}{S_\alpha + S_\beta} \tag{A2.4a}$$

$$-\frac{n\pi}{S_\alpha + S_\beta}B_n$$

$$= \frac{2}{S_\alpha + S_\beta}\left(\int_0^{S_\alpha}\left(\frac{\delta C}{\delta z}\right)_{z=0}\cos\left(\frac{n\pi x}{S_\alpha + S_\beta}\right)dx + \int_{S_\alpha}^{S_\alpha+S_\beta}\left(\frac{\delta C}{\delta z}\right)_{z=0}\cos\left(\frac{n\pi x}{S_\alpha + S_\beta}\right)dx\right)$$

$$= \frac{2}{n\pi}\left(-\frac{VC_0^\alpha}{D}\sin\left(\frac{n\pi S_\alpha}{S_\alpha + S_\beta}\right) - \frac{VC_0^\beta}{D}\sin\left(\frac{n\pi S_\alpha}{S_\alpha + S_\beta}\right)\right)$$

$$= -\frac{2}{n\pi}\frac{V}{D}C_0 \sin\left(\frac{n\pi S_\alpha}{S_\alpha + S_\beta}\right)$$

$$B_n = -\frac{2}{(n\pi)^2}\left(S_\alpha + S_\beta\right)\frac{V}{D}C_0 \sin\left(\frac{n\pi S_\alpha}{S_\alpha + S_\beta}\right) \tag{A2.4b}$$

Where $C_0 = C_0^\alpha + C_0^\beta$, as shown in Fig. A2.3.

The average composition in the liquid at the in front of the α phase (z=0) is given by

$$\begin{aligned}\overline{C}_\alpha &= C_E + C_\infty + B_0 + \frac{1}{S_\alpha}\int_0^{S_\alpha}\sum_{n=1}^{\infty} B_n \cos\left(\frac{n\pi}{S_\alpha + S_\beta}\right)dx \\ &= C_E + C_\infty + B_0 + \frac{2\left(S_\alpha + S_\beta\right)^2}{S_\alpha}\frac{V}{D}C_0 P\end{aligned} \tag{A2.5a}$$

And similarly, in front of the β phase, by

$$\begin{aligned}\bar{C}_\beta &= C_E + C_\infty + B_0 + \frac{1}{S_\beta}\int_{S_\alpha}^{S_\alpha+S_\beta}\sum_{n=1}^{\infty} B_n \cos\left(\frac{n\pi}{S_\alpha+S_\beta}\right)dx \\ &= C_E + C_\infty + B_0 - \frac{2\left(S_\alpha+S_\beta\right)^2}{S_\beta}\frac{V}{D}C_0 P\end{aligned} \tag{A2.5b}$$

Where $P=\sum_{n=1}^{\infty}\left(\frac{1}{n\pi}\right)^3 \sin^2\left(\frac{n\pi S_\alpha}{S_\alpha+S_\beta}\right)$. P depends only on the ratio S_α/S_β

A2.3. Diffusion in Rod Growth

To calculate the average composition of liquid in front of α and β phase, consider an interface, with r_α and r_β respectively half the widths of α and β phases as shown in Fig. A2.4.

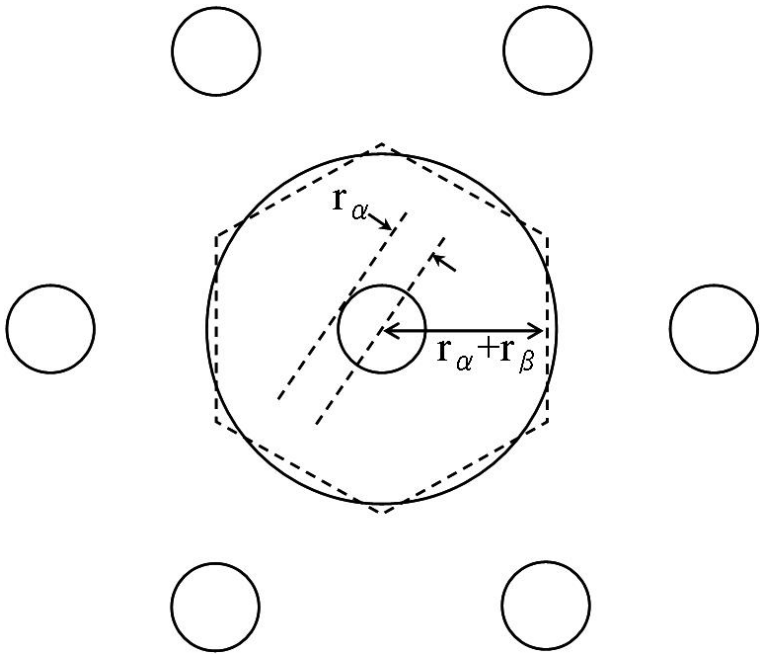

Figure A2.4. Schematic drawing of a rod structure viewed normal to the interface showing definition of r_α and r_β.

The interface is assumed to be advancing in the z direction with velocity V, at steady-state. For steady-state growth with the coordinate system moving with velocity V in the z direction, the diffusion equation becomes

$$\Delta^2 C + \frac{V}{D}\frac{\partial C}{\partial z} = 0 \tag{A2.6a}$$

$$\frac{\partial^2 C}{\partial r^2} + \frac{1}{r}\frac{\partial C}{\partial r} + \frac{\partial^2 C}{\partial z^2} + \frac{V}{D}\frac{\partial C}{\partial z} = 0 \tag{A2.6b}$$

The boundary conditions:

$$C = C_E + C_\infty \quad \text{at} \quad z = \infty \tag{A2.6c}$$

$$\frac{\partial C}{\partial r} = 0 \quad \text{at} \quad r = 0 \quad \text{and} \quad r = r_\alpha + r_\beta \tag{A2.6d}$$

The conservation of matter at the interface is similar to that for lamellar

$$\begin{aligned} \left(\frac{\partial C}{\partial z}\right)_{z=0} &= -\frac{VC_0^\alpha}{D} \qquad 0 \le r < r_\alpha \\ \left(\frac{\partial C}{\partial z}\right)_{z=0} &= \frac{VC_0^\beta}{D} \qquad r_\alpha < r \le r_\alpha + r_\beta \end{aligned} \tag{A2.6e}$$

The solution of Eq. A2.6a can be solved using the method of separation of variables.

$$Let\ C(r,z) = R(r)Z(z)$$

$$R''Z + \frac{1}{r}R'Z + RZ'' + \frac{V}{D}RZ' = 0$$

$$\frac{R'' + (1/r)R'}{R} = -\frac{Z'' + (V/D)Z'}{Z} = -\omega^2$$

$$Z'' + (V/D)Z' - \omega^2 Z = 0 \tag{A2.7a}$$

$$R'' + \frac{1}{r}R' + \omega^2 R = 0 \tag{A2.7b}$$

For Z

$$Z = Ee^{\lambda_1 Z} + Fe^{\lambda_2 Z} = Fe^{\lambda_2 Z}$$

$$\lambda_1 = -\frac{V}{2D} + \sqrt{(\frac{V}{2D})^2 + \omega^2} > 0$$

$$\lambda_2 = -\frac{V}{2D} - \sqrt{(\frac{V}{2D})^2 + \omega^2} < 0$$

Thus $\lambda_1 = 0$. Set $F = 1$

$$Z = e^{\left(-\frac{V}{2D}-\sqrt{(\frac{V}{2D})^2+\omega^2}\right)Z}$$

For R, introducing the new independent variable $s = \omega r$, we have $1/r = \omega/s$, so that, by the chain rule, the derivatives become

$$R' = \frac{dR}{dr} = \frac{dR}{ds}\frac{ds}{dr} = \frac{dR}{ds}\omega \text{ and } R'' = \frac{d^2R}{ds^2}\omega^2$$

By substituting this into Eq. A2.7b and omitting the common factor ω^2 we obtain

$$\frac{d^2R}{ds^2} + \frac{1}{s}\frac{dR}{ds} + R = 0$$

This is Bessel's equation. A general solution is

$$R = AJ_0(s) + BY_0(s)$$

Where J_0 and Y_0 are the Bessel functions of the first and second kind of order zero. Since the concentration of the system is always finite while Y_0 becomes infinite as s approaches zero, we cannot use Y_0 and must choose $B = 0$. Clearly $A \neq 0$ since otherwise $R \equiv 0$.

$$R(r) = AJ_0(s) = AJ_0(\omega r)$$

$$Z = e^{\left(-\frac{V}{2D}-\sqrt{(\frac{V}{2D})^2+\omega^2}\right)Z}$$

$$C(r,z) = AJ_0(\omega r)e^{\left(-\frac{V}{2D}-\sqrt{(\frac{V}{2D})^2+\omega^2}\right)Z} + G$$

By the boundary condition $C = C_E + C_\infty$ at $z = \infty$

$$G = C_E + C_\infty$$

$$\frac{\delta C}{\delta r} = \omega AJ_0'(\omega r)e^{\left(-\frac{V}{2D}-\sqrt{(\frac{V}{2D})^2+\omega^2}\right)Z} = \omega AJ_1(\omega r)e^{\left(-\frac{V}{2D}-\sqrt{(\frac{V}{2D})^2+\omega^2}\right)Z}$$

because $J_0'(x) = J_1(x)$

By the boundary condition $\frac{\partial C}{\partial r} = 0$ at $r = 0$ and $r = r_\alpha + r_\beta$

$$\left(\frac{\delta C}{\delta r}\right)_{r=0} = \omega A J_1(0) e^{\lambda_2 z} = 0$$

since $J_1(0) = 0$

$$\left(\frac{\delta C}{\delta r}\right)_{r=r_\alpha+r_\beta} = \omega A J_1(\omega(r_\alpha + r_\beta)) = 0$$

Thus, we require that, $J_1\left(\omega\left(r_\alpha + r_\beta\right)\right) = 0$

The Bessel function J_1 has infinitely many real zeros. Let us denote the roots of $J_1(s)$ by $s = \omega\left(r_\alpha + r_\beta\right) = \gamma_0, \gamma_1, \gamma_2, \cdots\cdots (\gamma_0 = 0)$

Thus, $\omega\left(r_\alpha + r_\beta\right) = \gamma_n$ or $\omega = \omega_n = \frac{\gamma_n}{r_\alpha + r_\beta}$.

Hence the functions

$$R_n(r) = A_n J_0(\omega_n r) = A_n J_0\left(\frac{\gamma_n}{r_\alpha + r_\beta} r\right), \quad (n = 0,\ 1,\ 2,\ \cdots).$$

Are solutions of Eq. A2.7b.

Hence the functions

$$C_n(r,z) = C_E + C_\infty + A_n J_0\left(\frac{\gamma_n}{r_\alpha + r_\beta} r\right) e^{\left(-\frac{V}{2D} - \sqrt{\left(\frac{V}{2D}\right)^2 + \left(\frac{\gamma_n}{r_\alpha + r_\beta}\right)^2}\right) Z}, \quad (n = 0,\ 1,\ 2,\ \cdots).$$

are the general solutions of the differential equation A2.6a, satisfying the boundary conditions. Clearly, a single solution $C_n(r,z)$ will not satisfy the conditions of the conservation of matter, Eqs. A2.6e, at the interface. To obtain a solution that stratifies the condition of the conservation of matter, Eq. A2.6e, the infinite series must be considered. Thus the solution of Eq. A2.6a is

$$C(r,z) = C_E + C_\infty + \sum_{n=0}^{\infty} A_n J_0\left(\frac{\gamma_n}{r_\alpha + r_\beta} r\right) e^{\left(-\frac{V}{2D} - \sqrt{\left(\frac{V}{2D}\right)^2 + \left(\frac{\gamma_n}{r_\alpha + r_\beta}\right)^2}\right) Z}$$

This reduces to

$$C(r,z) = C_E + C_\infty + A_0 e^{-\frac{V}{D} z} + \sum_{n=1}^{\infty} A_n J_0\left(\frac{\gamma_n}{r_\alpha + r_\beta} r\right) e^{-\frac{r_n z}{r_\alpha + r_\beta}} \qquad \text{(A2.8)}$$

Since $\gamma_0 = 0$, $J_0(0) = 1$ and $\frac{\gamma_n}{r_\alpha + r_\beta} >> \frac{V}{D}$ for $n > 0$

To evaluate the coefficients that satisfies the conservation of matter

$$\frac{\partial C}{\partial z} = -\frac{V}{D} A_0 e^{-\frac{V}{D} z} - \frac{\gamma_n}{r_\alpha + r_\beta} \sum_{n=1}^{\infty} A_n J_0\left(\frac{\gamma_n r}{r_\alpha + r_\beta}\right) e^{-\frac{\gamma_n z}{r_\alpha + r_\beta}}$$

$$\left(\frac{\delta C}{\delta z}\right)_{z=0} = -\frac{V}{D} A_0 - \frac{\gamma_n}{r_\alpha + r_\beta} \sum_{n=1}^{\infty} A_n J_0\left(\frac{\gamma_n r}{r_\alpha + r_\beta}\right)$$

Using formulas for the constant of Fourier-Bessel series that satisfy the condition

$J_{n+1}(\gamma_n) = 0$

$$C_m = \frac{2}{R^2 J_n^2(\gamma_{mn})} \int_0^R r f(r) J_n(\omega_{mn} r)\, dr \quad (m = 0,\ 1,\ 2,\ \cdots).$$

Thus,

$$-\frac{V}{D} A_0 = \frac{2}{\left(r_\alpha + r_\beta\right)^2 J_0^2(0)} \int_0^{r_\alpha + r_\beta} r f(r) J_0(0)\, dr$$

$$= \frac{2}{\left(r_\alpha + r_\beta\right)^2} \left(\int_0^{r_\alpha} r \left(\frac{-V C_0^\alpha}{D} \right) dr + \int_{r_\alpha}^{r_\alpha + r_\beta} r \left(\frac{V C_0^\beta}{D} \right) dr \right)$$

$$= \frac{2}{\left(r_\alpha + r_\beta\right)^2} \left(\left(-\frac{V C_0^\alpha}{2D} r^2 \right)_{r=0}^{r=r_\alpha} + \left(\frac{V C_0^\beta}{2D} r^2 \right)_{r=r_\alpha}^{r=r_\alpha + r_\beta} \right)$$

$$= \frac{1}{\left(r_\alpha + r_\beta\right)^2}\left(-\frac{VC_0^\alpha r_\alpha^2}{D} + \frac{VC_0^\beta\left(r_\alpha + r_\beta\right)^2}{D} - \frac{VC_0^\beta r_\alpha^2}{D}\right) = -\frac{V}{D}\left(\left(\frac{r_\alpha}{r_\alpha + r_\beta}\right)^2 C_0 - C_0^\beta\right)$$

$$A_0 = \left(\frac{r_\alpha}{r_\alpha + r_\beta}\right)^2 C_0 - C_0^\beta \tag{A2.9a}$$

$$-\frac{\gamma_n}{r_\alpha + r_\beta} A_n = \frac{2}{\left(r_\alpha + r_\beta\right)^2 J_0^2(\gamma_n)} \int_0^{r_\alpha + r_\beta} r f(r) J_0\left(\frac{\gamma_n r}{r_\alpha + r_\beta}\right) dr$$

$$= \frac{2}{\left(r_\alpha + r_\beta\right)^2 J_0^2(\gamma_n)}\left(\int_0^{r_\alpha} r\left(\frac{-VC_0^\alpha}{D}\right) J_0\left(\frac{\gamma_n r}{r_\alpha + r_\beta}\right) dr + \int_{r_\alpha}^{r_\alpha + r_\beta} r\left(\frac{VC_0^\beta}{D}\right) J_0\left(\frac{\gamma_n r}{r_\alpha + r_\beta}\right) dr\right)$$

$$= \frac{2}{\left(r_\alpha + r_\beta\right)^2 J_0^2(\gamma_n)}\left(\begin{array}{l}\left(-\frac{VC_0^\alpha\left(r_\alpha + r_\beta\right)}{\gamma_n D} r J_1\left(\frac{\gamma_n r}{r_\alpha + r_\beta}\right)\right)_{r=0}^{r=r_\alpha} \\ + \left(\frac{VC_0^\beta\left(r_\alpha + r_\beta\right)}{\gamma_n D} r J_1\left(\frac{\gamma_n r}{r_\alpha + r_\beta}\right)\right)_{r=r_\alpha}^{r=r_\alpha + r_\beta}\end{array}\right)$$

$$= \frac{2}{\left(r_\alpha + r_\beta\right)^2 J_0^2(\gamma_n)}\left(-\frac{VC_0^\alpha\left(r_\alpha + r_\beta\right) r_\alpha}{\gamma_n D} J_1\left(\frac{\gamma_n r_\alpha}{r_\alpha + r_\beta}\right) - \frac{VC_0^\beta\left(r_\alpha + r_\beta\right) r_\alpha}{\gamma_n D} J_1\left(\frac{\gamma_n r_\alpha}{r_\alpha + r_\beta}\right)\right)$$

$$= \frac{2Vr_\alpha}{D} C_0 \frac{J_1\left(\frac{\gamma_n r_\alpha}{r_\alpha + r_\beta}\right)}{\left(r_\alpha + r_\beta\right)\gamma_n J_0^2(\gamma_n)}$$

$$A_n = \frac{2Vr_\alpha}{D} C_0 \frac{J_1\left(\frac{\gamma_n r_\alpha}{r_\alpha + r_\beta}\right)}{\left[\gamma_n J_0(\gamma_n)\right]^2} \tag{A2.9b}$$

The average composition of the liquid at the in front of the α phase (z=0) is given by

$$\bar{C}_\alpha = \frac{4V}{D}\left(r_\alpha + r_\beta\right) C_0 M + C_E + C_\infty + A_0 \tag{A2.10a}$$

And

$$\bar{C}_\beta = \frac{4r_\alpha^2\left(r_\alpha + r_\beta\right)}{\left(r_\alpha + r_\beta\right)^2 - r_\alpha^2} \frac{V}{D} C_0 M + C_E + C_\infty + A_0 \tag{A2.10b}$$

Where

$$M = \sum_{n=1}^{\infty} \frac{1}{\gamma_n^3} \frac{J_1^2\left(\frac{r_\alpha \gamma_n}{r_\alpha + r_\beta}\right)}{J_0^2(\gamma_n)}$$

M depends only on the ratio r_α / r_β

A2.4. Average Curvature of a Lamellar Interface

As shown in Fig. A2.5, Taking the origin at the center of a lamella, so that the slope is zero at x=0

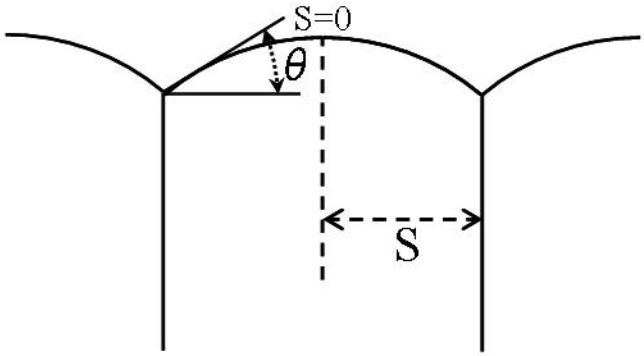

Figure A2.5. Schematic drawing of a lamellar interface showing definition of S and θ.

The average curvature is given by

$$\left\langle \frac{1}{r(x)} \right\rangle = \frac{1}{S}\int_0^S \frac{dx}{r(x)} = \frac{1}{S}\int_0^S \frac{-\frac{d^2z}{dx^2}}{\left(1+\left(\frac{dz}{dx}\right)^2\right)^{3/2}} dx$$

By setting $\tan\theta = \frac{dy}{dx}$, thus $\cos^{-2}\theta d\theta = \frac{d^2y}{dx^2}dx$,

$$\left\langle \frac{1}{r(x)} \right\rangle = \frac{1}{S}\int_0^S \frac{-\frac{d^2z}{dx^2}}{\left(1+\left(\frac{dz}{dx}\right)^2\right)^{3/2}} dx = \frac{1}{S}\int_0^{-\theta} \frac{-\cos^{-2}\theta}{\left(1+\tan^2\theta\right)^{3/2}} d\theta$$

$$= -\frac{1}{S}\int_0^{-\theta} \cos\theta d\theta = \left(-\frac{1}{S}\sin\theta\right)_0^{-\theta} = \frac{1}{S}\sin\theta \qquad \text{(A2.11)}$$

A2.5. Average Curvature of a Rod-Type Interface

For a point of P on a surface of revolution obtained by rotation about AB (Figure A2.6), one of the principal radii of curvature, ρ1, is in the plane of the paper. The other, ρ_2, is in the plane normal to the surface at P.

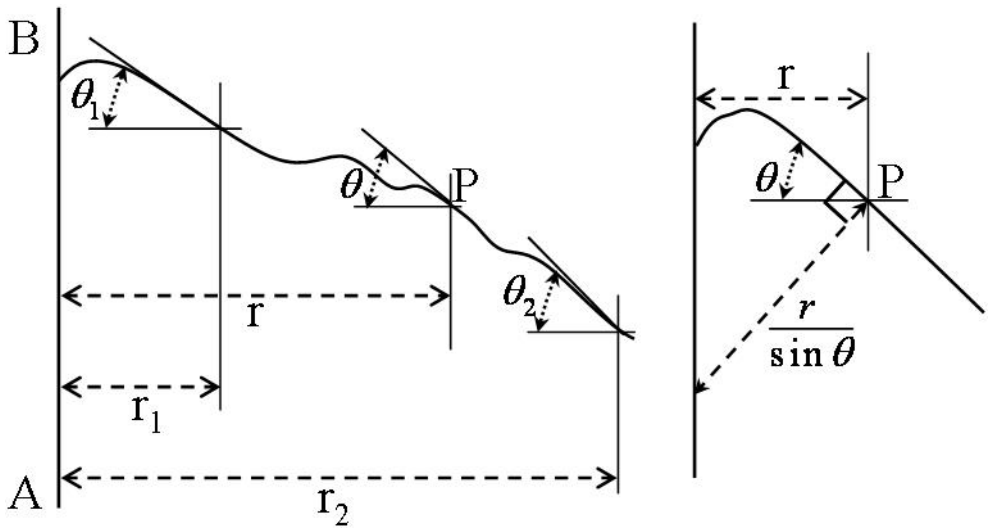

Figure A2.6. The average curvature of a surface of revolution generated by rotating any curve about the line AB depends only on the limiting radii r_1 and r_2 between which the average is to be computed, and on the angels θ_1 and θ_2 at these limits.

The radius of curvature in the plane of the paper is given by

$$\frac{1}{\rho_1} = \frac{-\frac{d^2z}{dr^2}}{\left[1+\left(\frac{dz}{dr}\right)^2\right]^{3/2}}$$

where z(r) is the equation of the surface in the plane of the paper.

From Fig. A2.5 and Meunier's theorem

$$\frac{1}{\rho_2} = -\frac{\sin\theta}{r} \quad \text{where} \quad \tan\theta = \frac{dz}{dr}$$

Total curvature at P is

$$\frac{1}{\rho} = \frac{1}{\rho_1} + \frac{1}{\rho_2}$$

The average total curvature of the surface between r_1 and r_2 is

$$\left\langle \frac{1}{\rho} \right\rangle = \frac{1}{\pi\left(r_2^2 - r_1^2\right)} \int_{r_1}^{r_2} 2\pi r \left(\frac{1}{\rho_1} + \frac{1}{\rho_2}\right) dr$$

$$= -\frac{2}{r_2^2 - r_1^2} \int_{r_1}^{r_2} \frac{r\left(\frac{d^2z}{dr^2}\right)dr}{\left[1+\left(\frac{dz}{dr}\right)^2\right]^{3/2}} - \frac{2}{r_2^2 - r_1^2} \int_{r_1}^{r_2} \sin\theta dr$$

Using same method used for the calculation of the lamellar case

$$\left\langle \frac{1}{\rho} \right\rangle = -\frac{2}{r_2^2 - r_1^2} \int_{\theta_1}^{\theta_2} r\cos\theta d\theta - \frac{2}{r_2^2 - r_1^2} \int_{r_1}^{r_2} \sin\theta dr = \left(-\frac{2}{r_2^2 - r_1^2} r\sin\theta \right)_{r_1}^{r_2} \qquad \text{(A2.12)}$$

$$= -\frac{2}{r_2^2 - r_1^2}\left(r_2\sin\theta_2 - r_1\sin\theta_1\right)$$

For α rods in a β matrix, we have for the α phase

$$r_2 = r_\alpha,\ r_1 = 0,\ \theta_2 = \tan^{-1}\left(\frac{dy}{dx}\right)_2 = -\theta_\alpha,\ \theta_1 = 0$$

So that

$$\left\langle \frac{1}{\rho_\alpha} \right\rangle = \frac{2}{r_\alpha}\sin\theta_\alpha \qquad \text{(A2.13a)}$$

For the β phase

$$r_2 = r_\alpha + r_\beta,\ r_1 = r_\alpha,\ \theta_1 = \theta_\beta,\ \theta_2 = 0$$

So that

$$\left\langle \frac{1}{\rho_\beta} \right\rangle = \frac{2r_\alpha}{\left(r_\alpha + r_\beta\right)^2 - r_\alpha^2} \sin\theta_\beta \qquad \text{(A2.13b)}$$

A2.6. Average Undercooling at the Interface and the Extremum Condition

A2.6.1. Interface Temperature

The freezing point depression by the departure of the local composition from the eutectic composition, ΔT_C, can be calculated by

$$\Delta T_C = m\left(C_E - C(x)\right)$$

m : The slope of the liquidus line

$C(x)$: The composition of the interface at x.

The freezing point depression by a non-planar interface, ΔT_σ, can be calculated by

$$\Delta T_\sigma = \frac{a}{r\left(x\right)}$$

a : A constant given by the Gibbson-Thompson relationship

$r\left(x\right)$: The local curvature of the interface

Thus total undercooling can be calculated by following equation:

$$T_E - T_I = \Delta T = \Delta T_C - \Delta T_\sigma$$

T_E : The eutectic temperature

T_I : The local actual temperature of the interface

A2.6.2. Average Undercooling of the Interface

The undercooling at any point on the interface is given by

$$\Delta T = m\left(C_E - C(x)\right) + \frac{a}{r\left(x\right)} \tag{A2.14}$$

The average undercooling at the interface for a lamellar eutectic is obtained by inserting average values for $C(x)$ and $1/r(x)$ from Eq. A2.5 and Eq. A2.11 into Eq. A2.14.

$$\Delta T_\alpha = m_\alpha \left(C_\infty + B_0 + \frac{2V}{D} C_0 \frac{\left(S_\alpha + S_\beta\right)^2}{S_\alpha} P \right) + \frac{a_\alpha^L}{S_\alpha} \tag{A2.15a}$$

$$\Delta T_\beta = m_\beta \left(-C_\infty - B_0 + \frac{2V}{D} C_0 \frac{\left(S_\alpha + S_\beta\right)^2}{S_\beta} P \right) + \frac{a_\beta^L}{S_\beta} \tag{A2.15b}$$

$$a_\alpha^L = \left(T_E / L\right)_\alpha \sigma_\alpha^L \sin\theta_\alpha^L$$
$$a_\beta^L = \left(T_E / L\right)_\beta \sigma_\beta^L \sin\theta_\beta^L$$

m_α and m_β: The slopes of the α and β liquidus lines, respectively (defined so that both are positive.

L : The heat of fusion per unit volume of the appropriate phase.

σ_α^L and σ_β^L: The specific surface free energies of the α-liquid and β-liquid interfaces, respectively.

The temperature within a few lamellar spacings of the interface is constant to within one hundredth of a degree or less.

Thus

$$\Delta T = \Delta T_\alpha = \Delta T_\beta$$

We can delete C_∞ and B_0 by combining Eq. A2.15a and b.

$$\frac{\Delta T_\alpha}{m_\alpha}+\frac{\Delta T_\beta}{m_\beta}=+\frac{2V}{D}C_0P\left(S_\alpha+S_\beta\right)^2\left(\frac{1}{S_\alpha}+\frac{1}{S_\beta}\right)+\frac{a_\alpha^L}{S_\alpha m_\alpha}+\frac{a_\beta^L}{S_\beta m_\beta}$$

Using $\lambda=2\left(S_\alpha+S_\beta\right)$, $\zeta=S_\beta/S_\alpha$

$$S_\alpha=\lambda/2\left(1+\zeta\right) \text{ and } S_\beta=\lambda/2\left(1+\zeta\right)$$

$$\Delta T\left(\frac{1}{m_\alpha}+\frac{1}{m_\beta}\right)=\frac{V\lambda}{D}C_0P\left(\frac{S_\alpha+S_\beta}{S_\alpha}+\frac{S_\alpha+S_\beta}{S_\beta}\right)+\frac{a_\alpha^L}{m_\alpha}\frac{2\left(1+\zeta\right)}{\lambda}+\frac{a_\beta^L}{m_\beta}\frac{2\left(1+\zeta\right)}{\zeta\lambda}$$

$$=\frac{V\lambda}{D}C_0P\frac{\left(1+\zeta\right)^2}{\zeta}+\frac{2\left(1+\zeta\right)}{\lambda}\left(\frac{a_\alpha^L}{m_\alpha}+\frac{a_\beta^L}{m_\beta}\right)$$

Thus,

$$\frac{\Delta T}{m}=V\lambda Q^L+\frac{a^L}{\lambda} \tag{A2.16}$$

Where m, Q^L, and a^L are constants given by

$$\frac{1}{m}=\frac{1}{m_\alpha}+\frac{1}{m_\beta} \tag{A2.17a}$$

$$Q^L=\frac{P\left(1+\zeta\right)^2C_0}{\zeta D} \tag{A2.17b}$$

$$a^L=2\left(1+\zeta\right)\left(\frac{a_\alpha^L}{m_\alpha}+\frac{a_\beta^L}{m_\beta}\right) \tag{A2.17c}$$

Eq. A2.16 is shown schematically for a given growth velocity in Fig. A2.7. The lamellar spacing, λ, may be adjusted arbitrarily for Eq. A2.16 to be satisfied. Assuming that the solid grows at the extremum. Eq. A2.16 has a minimum at constant growth velocity.

$$\frac{1}{m}\frac{\delta\left(\Delta T\right)}{\delta\lambda}=VQ^L-\frac{a^L}{\lambda^2}=0$$

Thus

$$\lambda^2 V = \frac{a^L}{Q^L} \tag{A2.18a}$$

$$\frac{\Delta T^2}{V} = 4m^2 a^L Q^L \tag{A2.18b}$$

$$\Delta T \lambda = 2ma^L \tag{A2.18c}$$

This relationship also corresponds to the maximum in the V vs λ curve, plotted at constant ΔT.

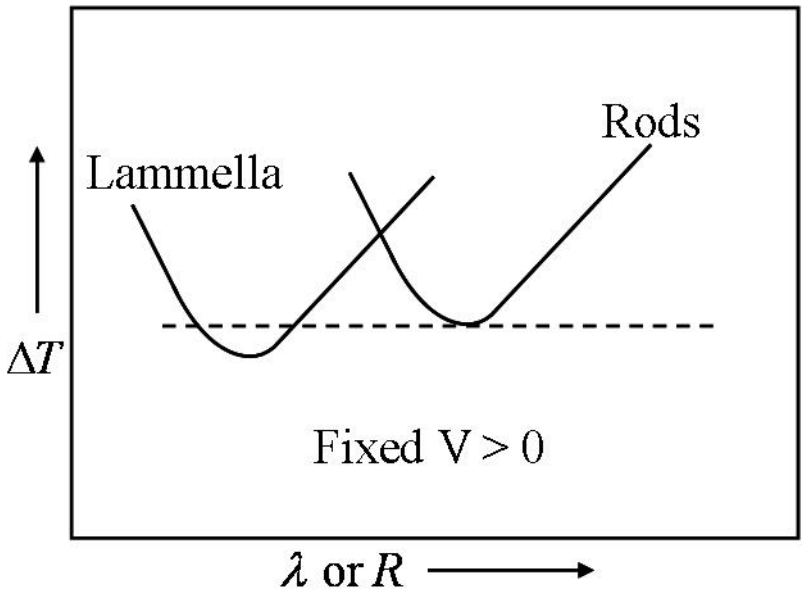

Figure A2.7. Schematic drawing of the variation of interface undercooling with lamellar spacing., λ, or rod spacing, R, for a given growth rate V.

Equations similar to Eqs. A2.15 but for the rod structure are obtained by combining Eqs. A2.10, A2.13, and A2.14

$$\Delta T_\alpha = m_\alpha \left(C_\infty + A_0 + \frac{4V}{D} C_0 \left(r_\alpha + r_\beta \right) M \right) + \frac{2a_\alpha^R}{r_\alpha} \tag{A2.19a}$$

$$\Delta T_\beta = m_\beta \left(-C_\infty - A_0 + \frac{4V}{D} C_0 \frac{\left(r_\alpha + r_\beta\right) r_\alpha^2}{\left(r_\alpha + r_\beta\right)^2 - r_\alpha^2} M \right) + \frac{2 a_\beta^R r_\alpha}{\left(r_\alpha + r_\beta\right)^2 - r_\alpha^2} \qquad \text{(A2.19b)}$$

Where

$$a_\alpha^R = \left(T_E / L\right)_\alpha \sigma_\alpha^R \sin\theta_\alpha^R$$
$$a_\beta^R = \left(T_E / L\right)_\beta \sigma_\beta^R \sin\theta_\beta^R$$

The superscript R refers to the rod structure since in general σ and θ will be different for lamellar and rod interfaces. As in the lamellar analysis, it will be assumed that the ratio of the two phases is constant ζ and R is defined by

$$R = r_\alpha + r_\beta = r_\alpha \sqrt{1+\zeta}$$

So that

$$r_\alpha = \frac{R}{\sqrt{1+\zeta}} \text{ and } r_\beta = R\left(1 - \frac{1}{\sqrt{1+\zeta}}\right)$$

Eqs. A2.19 can be combined giving

$$\frac{\Delta T}{m} = VRQ^R + \frac{a^R}{R} \qquad \text{(A2.20)}$$

Where

$$a^R = 2\sqrt{1+\zeta}\left(\frac{a_\alpha^R}{m_\alpha} + \frac{a_\beta^R}{\zeta m_\beta}\right) \qquad \text{(A2.21a)}$$

and

$$Q^R = \frac{4\left(1+\zeta\right)}{D\zeta} C_0 M \qquad \text{(A2.21b)}$$

Eq. A2.20 is formally identical to Eq.A2.16. The extremum is there for given by following equations.

$$R^2 V = \frac{a^R}{Q^R}$$

$$\frac{\Delta T^2}{R} = 4m^2 a^R Q^R \tag{A2.22}$$

$$\Delta TR = 2ma^R$$

A2.7. Rod Formation

When the rod minimum undercooling is smaller than that for lamellar, the lamellar structure will not be formed. By comparing Eq. A2.16 with Eq. A2.20, the condition for rod formation at a given growth velocity can be calculated by

$$\frac{\Delta T_L}{m} > \frac{\Delta T_R}{m}$$

$$\frac{\left(\frac{a_\alpha^L}{m_\alpha} + \frac{a_\beta^L}{m_\beta}\right)}{\left(\frac{a_\alpha^R}{m_\alpha} + \frac{a_\beta^R}{\zeta m_\beta}\right)} > \frac{4M}{P}\frac{1}{(1+\zeta)^{3/2}}\, a^R = 2\sqrt{1+\zeta}\left(\frac{a_\alpha^R}{m_\alpha} + \frac{a_\beta^R}{\zeta m_\beta}\right) \tag{A2.23}$$

For isotropic solid-liquid and α-β interfacial free energies, the left-hand side of this equation is equal to one. The right hand side is given in Table II. It is evident from the table that, if the surface energies are isotropic, rods have the lower minimum when

$$1/(1+\zeta) < 1/\pi\,. \tag{A2.24}$$

Thus, the growth of rod-type eutectic occurs when the volume difference of two phases is very big.

Acknowledgment

This thesis is the summary of research conducted by the author at the Laboratory of Materials Processing Engineering, Department of Chemical Engineering, Kyoto University, from 2007 to 2010.

I would like to express my deep and sincere gratitude to Professor Masahiro Ohshima, Department of Chemical Engineering, Kyoto University. His wide knowledge and logical way of thinking have been of great value for me. His understanding, encouraging and personal guidance have provided a good basis for the present thesis.

It was a great honor to have two official referees for this thesis, Dr. Hajime Tamon and Dr. Minoru Miyahara, Professors of Department of Chemical Engineering, Kyoto University. I really appreciate for their detailed review, constructive criticism and excellent advice during the preparation of this thesis.

I would like to show my warm and sincere thanks to Dr. Kentaro Taki, Assistant Professor of Kyoto University and Dr. Shinsuke Nagamine, Lecture of Kyoto University for detailed and constructive comments, and for important support. Their guidance helped me in all the time of research. I would like to specially thank Ms. Maki Hiroyama, Secretary of the Laboratory of Materials Processing Engineering, for her kind supports and help.

I would also like to thank members of Coating Research Working Group. Their ideas and concepts have had a remarkable influence on my research in the field of phase separation. My sincere thanks also go to Dr. Masato Yamamura, Associate Professor, Department of Applied Chemistry, Kyushu Institute of Technology for offering me the opportunities to participate in the working group.

During this work I have collaborated with many colleagues for whom I have great regard, and I wish to extend my warmest thanks to all those who have helped me with my work. Specially, I am indebted to Dr. Jae-Kyung Kim. His valuable advice and extensive discussions have been very helpful for this study. I would also like to specially thank to Ms. Kohei Tazumi for our collaboration.

I gratefully acknowledge the financial support of SK Energy, Co., Ltd. during my education period in Kyoto University. Furthermore my gratitude is sincerely expressed to all members of SK Energy for their compensation of my long absence. Without their endless encouragement and support it would have been impossible for me to finish my Ph.D. work.

Finally, I want to take this opportunity to thank my family members. They have lost a lot due to my research abroad. As always, my family has been there, providing all sorts of tangible and intangible support.

Jin-Woong Kim

List of Publications

Chapter 2

Kim, J. W.; Taki, K.; Nagamine, S.; Ohshima, M., Preparation of Poly(L-lactic acid) Honeycomb Monolith Structure by Unidirectional Freezing and Freeze-drying. *Chemical Engineering Science* **2008**, *63*, 3858-3863.

Chapter 3

Kim, J. W.; Taki, K.; Nagamine, S.; Ohshima, M., Preparation of Porous Poly(L-lactic acid) Honeycomb Monolith Structure by Phase Separation and Unidirectional Freezing. *Langmuir* **2009**, *25*, 5304-5312.

Chapter 4

Kim, J. W.; Tazumi, K.; Okaji, R.; Ohshima, M., Honeycomb Monolith Structured Silica with Highly Ordered, Three-dimensionally Interconnected Macroporous Walls, *Chemistry of Materials* **2009**, *21*, 3476-3478.

Other Relevant Publication

1. Todo, M.; Kuraoka, H.; Kim, J. W.; Taki, K.; Ohshima, M., Deformation Behavior and Mechanism of Porous PLLA under Compression. *Journal of Materials Science* **2008**, *43*, 5644-5646.

2. Todo, M.; Park, J. E.; Kuraoka, H.; Kim, J. W.; Taki, K.; Ohshima, M., Compressive deformation behavior of porous PLLA/PCL polymer blend. *Journal of Materials Science* **2009**, *44*, 4191-4194.

International Conferences

1. Kim, J. W.; Kim, J. K.; Taki, K.; Ohshima, M., Preparation of Porous Polymeric Materials from Ternary Components Polymer Solution using Phase Separation, *Biofoams 1st International Conference,* Capri, Italy (2007).

2. Kim, J. W.; Taki, K.; Nagamine, S.; Ohshima, M., Preparation of Honeycomb Monolith Structure with Micro/Nanoscale Porous Wall, *8th Japan-Korea Symposium on Materials & Interfaces*, Sapporo, Japan (2008).

3. Kim, J. W.; Taki, K.; Nagamine, S.; Ohshima, M., Preparation of Porous Poly(L-lactic acid) Honeycomb Monolith Structure by Unidirectional Freezing and Freeze Drying, *AIChE Annual Meeting* Philadelphia, America (2008).

4. Ohshima, M.; Nemoto, T.; Itoh, M.; Kabumoto, A.; Kim, J. W.; Kim, J. K.; Taki, K., Preparation of Porous Polymeric Materials by Polymer Processing, *4th International Symposium on Designing, Processing and Properties of Advanced Engineering Materials* Nagoya, Japan (2008).